11-1-2019 1:45 PM

# Synthesis of VO2/Poly(MMA-co-dMEMUABr) Antimicrobial/Thermochromic Dual-functional Coating and Reactivity Ratios Study

Yixian Liu, *The University of Western Ontario*

Supervisor: Charpentier, Paul A., *The University of Western Ontario*
A thesis submitted in partial fulfillment of the requirements for the Master of Engineering Science degree in Chemical and Biochemical Engineering
© Yixian Liu 2019

### Recommended Citation

# Abstract

Antimicrobial/thermochromic dual-functional coatings were successfully synthesized via UV-curing. The quaternary ammonium compound (QAC) N,N-dimethyl-N-{2-[(2-methylprop-2-enoyl)oxy]ethyl}undecane-1-aminium bromide (dMEMUABr) was synthesized and copolymerized with methyl methacrylate (MMA) for antimicrobial properties. Vanadium oxide ($VO_2$) nanoparticles were evenly dispersed within the coating, providing thermochromic properties. The dual-functional coating showed high luminous transmittance ($T_{lum(25°C)}$ =36.1 %) and solar energy modulation ($\Delta T_{sol}$=5.8 %). 90.3 % of bacteria reduction was observed against Escherichia coli within 24 h contact. To further understand the sequence distribution of the copolymer poly(MMA-co-dMEMUABr), the reactivity ratios of MMA and dMEMUABr monomer were studied and compared under thermal and UV initiation copolymerization. In the non-polar solvent chloroform-d, the reactivity ratio of MMA ($r_{MMA}$=0.06-0.46) was found lower than that of dMEMUABr ($r_{dMEMUABr}$=6.64-11.51) under thermal copolymerization, which was found consistent for reactivity ratios under UV copolymerization ($r_{MMA}$=0.73-0.76, $r_{dMEMUABr}$=4.42-4.48). However, in the polar solvent DMSO-$d_6$, it showed the opposite tendency ($r_{MMA}$=1.65-1.73, $r_{dMEMUABr}$=0.24-0.32) attributed to solvent-dMEMUABr monomer interactions.

## Keywords

# Summary for lay audience

Smart window coatings are considered promising for reducing air conditioning loads to save energy, as they can intelligently regulate the solar radiation and heat transmitted through the window. A further challenge with smart windows is their tendency to foul, as bacteria accumulate on their surfaces. These factors raise health concerns while increasing cleaning costs. This thesis examined synthesizing dual functional coatings, which can both regulate light and heat flow while being antimicrobial. Vanadium dioxide ($VO_2$) nanoparticles were used as the light/heat regulating agents (i.e. thermochromic), which can block undesired infrared light when temperature exceeds its critical temperature (~68 °C). The results showed that the synthesized $VO_2$ nanoparticles were evenly dispersed within the polymer coating, which exhibited thermochromic behavior. The antimicrobial agent, quaternary ammonium compound (QAC) named N,N-dimethyl-N-{2-[(2-methylprop-2-enoyl)oxy]ethyl}undecane-1-aminium bromide (dMEMUABr) was polymerized with methyl methacrylate (MMA) through UV curing using the photo initiator 2-hydroxyl-2-methylpropiophenzssone (HMP). These dual-functional antimicrobial/thermochromic coatings were found to reversibly tune the transmittance of infrared solar radiation to cut the energy consumption, while simultaneously killing attached bacteria to reduce fouling and the resulting pathogenic risk.

To further investigate the copolymerization of dMEMUABr and MMA for coating film preparation, the reactivity ratios of these two monomers were measured. The reactivity ratio values of dMEMUABr and MMA can predict the sequence structure of copolymer chains, which determine the ultimate chemical and physical properties of the copolymer. Therefore, understanding the reactivity ratios is essential for designing and tailoring the copolymer structures for various applications. The reactivity ratios of MMA and dMEMUABr were investigated and compared under thermal and UV initiated copolymerization respectively. The added thermal initiator or photo initiator both produce free radicals to initiate the copolymerization. Two solvents of varying polarity were compared towards reactivity ratios using the polar solvent DMSO-$d_6$ and non-polar solvent chloroform-d. An *in-situ* NMR technique and conventional low-conversion technique were compared for obtaining data for reactivity ratio calculations. *In-situ* NMR allows simultaneously monitoring the real-time concentration data for each monomer, providing an efficient, reliable and simple technique

for measuring reactivity ratios. This study provided important clues for tailoring the copolymer structure, poly (MMA-co-dMEMUABr), for various applications.

# Acknowledgments

I would like to acknowledge many people, who gave me their sincere helps during the past two years.

First, I would like to give my sincere gratitude to my supervisor Prof. Paul A. Charpentier, who gave me greatly understanding, support and trust during my master program. Whenever I have any trouble or confusion, he is always willing to help me. This work would not be done without his guidance.

I would also like to thank all my lab colleagues for their suggestions and strong support, especially Dr. William Xu and Dr. Olabode Olujimi Oyeneye. They provided many helpful suggestions and help during my research progress.

Finally, I was grateful to my family and all my friends for their company and encouragement. The love and happiness they brought to me is my motivation to become better.

# Table of Contents

# List of Tables

# List of Figures

# List of Abbreviations

QACs — Quaternary ammonium compounds

dMEMUABr — N, N-dimethyl-N-{2-[(2-methylprop-2-enoyl)oxy]ethyl}undecane-1-aminium bromide

$VO_2$ (M)/(R) — Vanadium oxide in monoclinic/ rutile phase

MMA/PMMA — Methyl methacrylate/ Poly (methyl methacrylate)

MIT — Metal-to-semiconductor phase transition

E.coli — Escherichia coli

DMAEMA — 2-(Dimethylamino) ethyl methacrylate

HMP — 2-hydroxy-2-methylpropiophenone

TMS — Tetramethylsilane

NMR — Nuclear magnetic resonance

$\Delta T_{sol}$ — Solar energy modulation

$T_{lum}$ — Luminous transmittance

CFU — Colony-forming unit

UV — Ultraviolet light

NLLS — Non-linear least squares

LLS — Linear least squares

DMF — N, N-dimethylformamide

AIBN — Azobisisobutyronitrile

DMSO-d — Deuterated dimethyl sulfoxide

Chloroform-d          Deuterated chloroform

$r_1, r_2$          Reactivity ratio

$f_1$          Mole fraction of MMA in the feed

$F_1$          Mole fraction of MMA in the copolymer

Xn          Mole conversion

DND          Direct numerical differential method

NSD          Numerical solution differential method

K-T          Kelen-Tüdös method

Chapter 1

# 1 Introduction

## 1.1 Background & Motivation

The increase in global population and rapid modernization in developing countries is leading to tremendous increases in worldwide energy consumption. Negative environmental effects are raising concerns about global warming, energy supply challenges and resource exhaustion, requiring urgent energy saving and alternative renewable technologies. [1-3] Energy used for buildings accounts for up to 40 % of energy requirements in developed countries. Of this energy requirement, over 60 % is used for heating, ventilation and air conditioning (HVAC) needs.[4] Cutting the usage frequency of space conditioning is key to save energy in buildings, and would help to drastically lower our carbon footprint. As windows are considered the least energy efficient place in a room, an effective way to address the goal is towards developing smart windows using thermochromic properties, which can control the solar radiation and reduce undesired heat loss/gain, without any input of energy.[5, 6]

An additional consideration towards smart windows is the challenge of window fouling by micro-organisms. Living organisms such as viruses, bacteria and parasites easily grow on the surface of coatings and windows, which may cause a diversity of health issues for humans. For example, it is reported that approximately 470 Canadians are infected with E.coli bacteria every year.[7] The infection causes illness and even death. To reduce the risk of pathogens and the loss of optical and thermal efficiency due to fouling, self-cleaning smart windows are highly desired. The ability to integrate both properties into next generation windows is of considerable interest and the goal of this thesis.

## 1.2 Thesis objective & structure

In this work, the first target is to synthesize a dual-functional coating, examining both antimicrobial and thermochromic properties of the coating. (Chapter 3) Quaternary ammonium compounds (QACs) were chosen as the antimicrobial agent to copolymerize

with methyl methacrylate (MMA) via UV curing for coating film preparation. QACs have the advantage of low toxicity, low cost and excellent environmental stability, compared to other antibiotics. They kill bacteria upon contact without releasing any toxic material. For thermochromic performance, vanadium oxide ($VO_2$) particles have been widely used for smart window application. When the temperature reaches a transition temperature of approximately 68 °C, $VO_2$ can reduce transmittance in the infrared light region and have a negligible influence on the visible light spectrum through its first order metal-to-semiconductor phase transition (MIT). The purity of synthesized $VO_2$ particles and QAC named N,N-dimethyl-N-{2-[(2-methylprop-2-enoyl)oxy]ethyl}undecane-1-aminium bromide (dMEMUABr) were well characterized and the performance of dual-functional coatings was evaluated.

The second target of this thesis is to further investigate the copolymerization mechanism of dMEMUABr and MMA. (Chapter 4) The reactivity ratios are determined for predicting the sequence distribution of the copolymer poly (MMA-co-dMEMUABr), which also provides important information for designing and tailoring copolymers for different applications or optimization. The copolymerization was carried out under both thermal initiation and UV initiation respectively. Solvents with different polarities were used for investigation. The composition data of the feed and copolymer was achieved using *in-situ* NMR and the conventional low-conversion technique. Non-linear least squares (NLLS) and linear least squares (LLS) calculation methods were applied for determining the reactivity ratios. The obtained reactivity ratios for MMA and dMEMUABr using polar/non-polar solvent and under thermal/UV initiated copolymerization were compared and discussed.

Chapter 2

# 2 Literature Review

## 2.1 Thermochromic vanadium oxide VO$_2$(M) nanoparticle

### 2.1.1 Smart window

Smart windows can regulate the transmittance of infrared light to prevent heat from passing through them.[8] This means that heat can be conserved inside the room in winter, and blocked outside in summer. In this case, the usage frequency of heating and cooling can be significantly decreased.

Current smart windows can be categorized into three main kinds: electrochromic, photochromic and thermochromic windows. [9] Electrochromic devices are usually produced as five-layer sandwich structures placed between two pieces of glass, which consist of two layers of transparent conductor, two electrochromic films (one of them is also called ion storage film) and one layer of electrolyte. The electrolyte is a mixture of conductor, conduct ions and electrons. When a voltage is applied, ions move between the electrochromic film and ion storage film layers, blocking the solar irradiation.[10] Our new engineering building in Western University, three C+, also utilizes this kind of energy saving smart window, which tints automatically and offers an unobstructed view. Tungsten trioxide is currently the most widely used electrochromic material for electrolyte.[11] On the other hand, photochromic windows can change their color to darker or lighter to attenuate the irradiation when they are exposed to light. These are considered to be derived from the combination of a dye-sensitized solar cell and an electrochromic device. The electrochromic reaction is driven by UV light for photochromic behavior.[12] Therefore, different UV intensities have an obvious influence on the color and performance of the widow depending on the weather, which is considered as one of the main disadvantages of photochromic windows. Compared to electrochromic and photochromic smart windows, thermochromic windows regulate the solar light responding to the surrounding temperature, which do not need any external switching device, power supply or UV light. These characteristics make the system simpler, self-adjustable and lower cost.

Electrochromic Smart Window    Photochromic Smart Window    Thermochromic Smart Window

Voltage    UV    Temperature

Electrochromic layer  Transparent conductor    Photochromic coating    Thermochromic coating
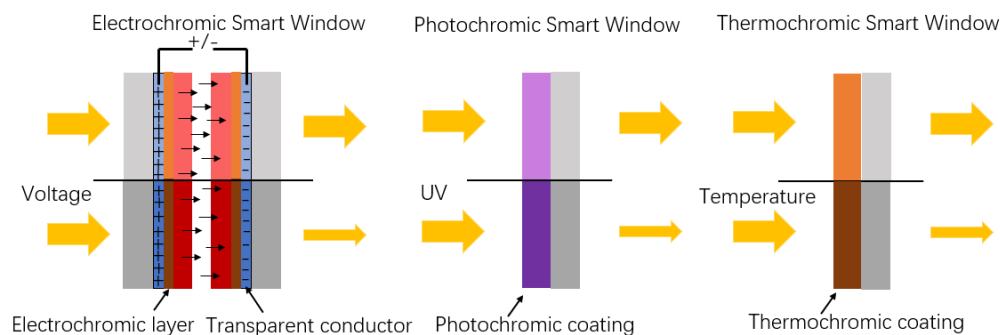
**Figure 2.1：Schematic of electrochromic, thermochromic and photochromic smart windows working mechansim.[9]**

## 2.1.2  Vanadium oxide $VO_2$(M)

The main functional material exhibiting the thermochromic property is vanadium oxide ($VO_2$). It has been studied for decades for smart window application, with its thermochromic property first discovered by Morin in the 1950s.[13] Although there are some other thermal-responsive materials, for example, hydrogels, ionic liquids, metamaterials, perovskites and liquid crystals,[9] $VO_2$ is studied the most intensively and the synthesis parameters can generally be well controlled. $VO_2$ works by blocking the infrared light without any other extra energy input, compared to other thermochromic materials.[14] $VO_2$ in the monoclinic phase and rutile phase are the most promising materials for energy-efficient coatings application. When the temperature exceeds its critical temperature (~68 °C), $VO_2$ (M) undergoes a first order metal-to-semiconductor phase transition (MIT) to the rutile phase.  This phase transition reduces transmittance in the infrared light region and has a negligible influence on the visible light spectrum. The $VO_2$ phase transition between monoclinic (IR transparent) and rutile (IR reflective) is reversible, and the ability to regulate the solar heat flux makes $VO_2$ (M) ideal for thermochromic smart window application.

Vanadium ($V^{n+}$) has different valence states from $V^{2+}$ to $V^{5+}$ , which makes nearly 20 stable phases of vanadium oxide.[15]  These non-stoichiometric vanadium oxide can be divided into two types. The first type exists between $V_2O_5$ and $VO_2$ with a general formula $V_nO_{2n+1}$, including $V_6O_{13}$, $V_3O_7$ and so on. The other type is called a Magnéli-type with

general formula $V_nO_{2n-1}$, including $V_4O_7$, $V_5O_9$, $V_6O_{11}$, $V_7O_{13}$ and $V_8O_{15}$.[16] The $V_nO_{2n+1}$ group has less numbers than that of Magnéli-type. In addition, besides the monoclinic and rutile phases, $VO_2$ has multiple polymorphic forms: tetragonal $VO_2(A)$, monoclinic $VO_2(B)$, $VO_2(D)$, monoclinic rutile-type $VO_2(M)$, tetragonal rutile-type $VO_2(R)$, $VO_2(P)$.[17] However, among all different morphologies, $VO_2(M)$ is the only one exhibiting full reversible first-order MIT, close to room temperature.[18]

## 2.1.3 Crystal and electronic structure

In $VO_2(R)$, all V atoms are in parallel linear chains with equal spacing along the crystallographic c axis.[19] In each $VO_6$ octahedra, the V atom is located at the center of a body-centered cubic.[20] Four oxygen atoms are closer to the centered vanadium atom with a V-O distance of 1.92 Å and other two oxygen atoms have a V-O distance of 1.93 Å. Through the MIT, when vanadium oxide transfers from the metallic R to insulating M phase, the cubic stretches along the V-V direction which leads to the pairing and tilting of the $VO_6$ octahedra and the relocation of vanadium atoms.[21] The V-V distance changes from 2.85 Å in $VO_2(R)$ to 3.12 Å and 2.65 Å in $VO_2(M)$. One $VO_2$ (M) unit cell contains 12 atoms which doubles the number in one $VO_2(R)$ unit cell.[14] The schematic of the crystal structures of $VO_2(M)$ and $VO_2(R)$ is shown in Figure 2.2 (a), (b).

In 1971, Goodenough first described the molecular orbital picture, based on crystal field theory.[22] As shown in Figure 2.2 (c), (d), in $VO_2(R)$, a narrow $\pi^*$ anti-bond and a $d_{II}$ nonbond partially overlap with each other and the level of density states $E_F$ is located at the overlapped area of $\pi^*$ and $d_{II}$ orbitals. After the MIT phase transition, the tilting of the octahedra and the dimerization of the vanadium ions elevate the $\pi^*$ bond to higher energies and separate the $d_{II}$ bond to one filled $d_{II}$ bonding and one empty anti-bonding component.[23, 14] The change of the band gap between $d_{II}$ and $\pi^*$ results in the insulating phase of $VO_2(M)$. The driven force of the MIT includes electron-correlation-driven Mott transition, structure-driven Peierls transition and the combination of these two transitions.[24]
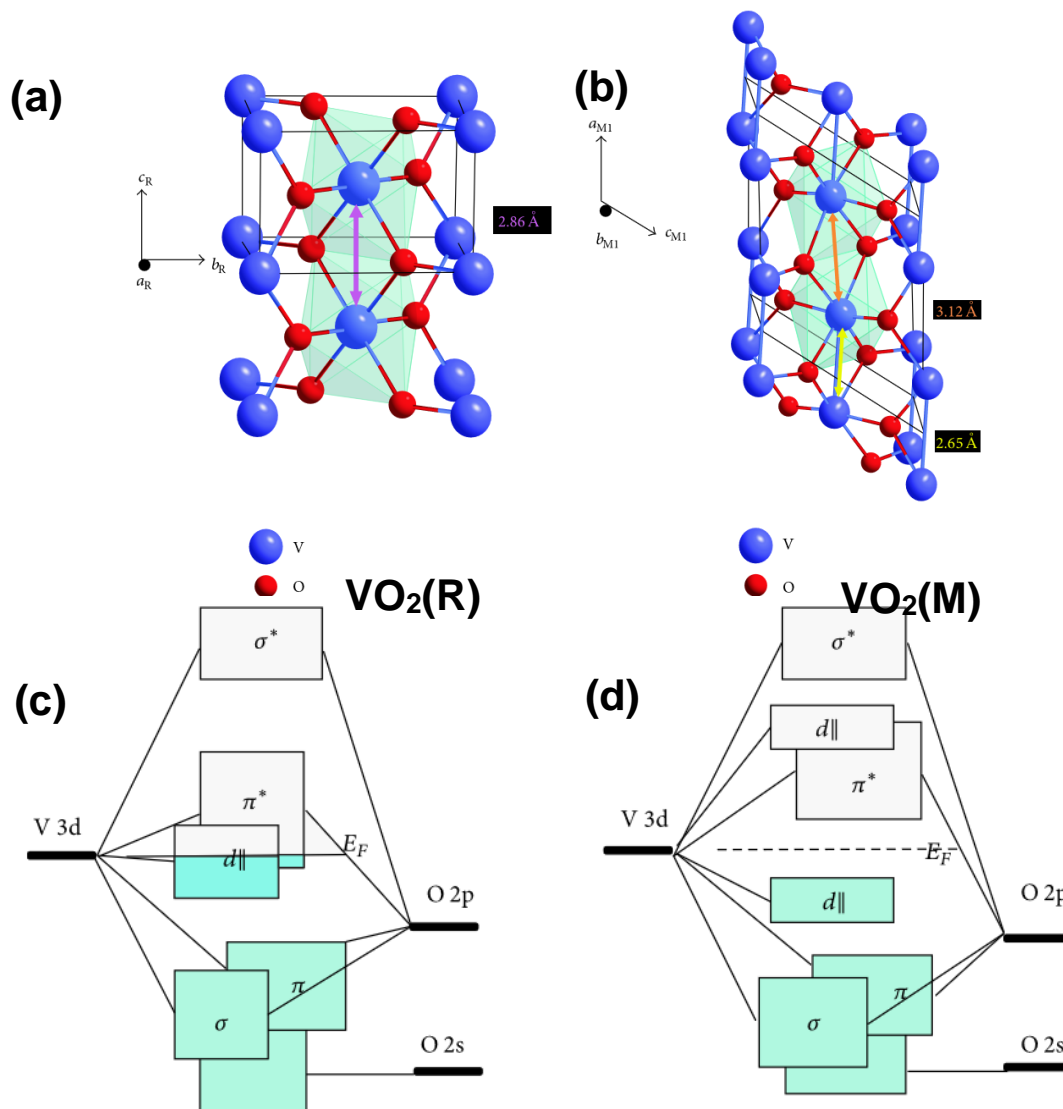
**Figure 2.2: Schematic of crystal structure of (a) high-temperature metallic and (b) the low-temperature insulating VO₂. And the electronic band structure of (c)rutile VO₂ and (d) monoclinic VO₂. [19]**

## 2.1.4   Effect of elemental dopants

In the practical application of $VO_2$ for smart windows, there are three main challenges: low luminous transmittance ($T_{lum}$), unexpected solar-energy modulation efficiency ($\Delta T_{sol}$) and a high transition temperature ($T_c$).[25] The transition temperature of bulk $VO_2$ nanoparticles is around 68 °C, which is too high to be used for window coatings. Doping

with high valence metal cations is an efficient way to reduce $T_c$, for example, W[26], Nb[27], Mo[28, 29] and so on. It was reported that doping with the metal element Nb can decrease the Tc by 7.8 °C per at %, and Mo can decrease Tc by 11 °C per at %.[29, 30] Among these, tungsten $W^{6+}$ is considered the most effective doping element, which can reduce $T_c$ by 20-26 °C per at %.[31] On the contrary, doping with low valence cations increases the transition temperature, for example, Ti[32], Ga[33], Cr[34].

The mechanism of decreasing the Tc by doping is based on electronic-driven Mott phase transition and structure-driven Peierls transitions. During the MIT, $VO_2$ experiences a continuous structural phase transition and the dopant acts as a donor or acceptor, producing electrons or holes to the electronic structure of $VO_2$. According to the Mott phase transition, the carrier concentration is then increased, and the energy barrier is reduced. Therefore, phase transition is easier to happen with less energy needed and the Tc decreases.[35] At the same time, the induced dopant causes the expansion and distortion of the $VO_2$ crystal structure, especially along the V-V bond. As the main crystal structure difference of $VO_2(M)$ and $VO_2(R)$ is the distance of V-V bond, the distortion makes the change easier, which reduces the $T_c$.[36] The increase in carrier concentration and structure distortion usually happen at the same time.[14] The dopant either is located at the interstitial sites or replaces a V or O lattice site.

## 2.1.5 Different $VO_2$ synthesis methods

Several methods have been developed for synthesizing $VO_2$. These methods can be categorized into two main types: gas-based and solution-based process. The gas-based deposition includes chemical vapor deposition (CVD) and physical vapor deposition (PVD). The solution-based process contains sol-gel method, hydrothermal method, electrochemical method, and polymer-assisted deposition. Different synthesis precursors and processes result in various $VO_2$ morphologies, structures and optical properties.

**Gas-based deposition**

The chemical vapor deposition (CVD) approach was first discovered for producing $VO_2$ film in 1967.[37] The two most frequently used methods are atmospheric chemical vapor deposition (APCVD) and aerosol assisted chemical vapor deposition (AACVD).[33] In the basic route of CVD process, liquid or solid precursors are heated and become gas phase by evaporation. The generated active gas reactants direct to the reaction chamber, where the gas reactants experience reactions at gas-solid interface and grow on the surface of the substrate to form a thin film.[38] Therefore, the CVD process is driven by a concentration gradient and includes internal molecular collisions.

A relatively recent CVD method for $VO_2$ film preparation uses an electric field assisted chemical vapor deposition.[39] Vanadyl aceylacetanoate was dissolved in ethanol and used as the precursor, which was then processed using a cold walled quartz tube CVD reactor. Electrodes within the reactor were coated with a transparent fluorine doped tin oxide allowing the electric field to cover the entire reaction chamber. It was shown that the applied electric field can affect the $VO_2$ crystallite orientation, microstructure and optical property.[40] By applying the electric field assisted chemical vapor deposition method, $VO_2$ was formed with reduced crystal size, increased surface area and enhanced wetting characteristics.

The physical vapor deposition (PVD) approach is similar to the CVD, which also consists of four main steps, which are evaporation, transportation, reaction and deposition. The difference is the target raw materials, which are activated as solid state, instead of the gas state as in the CVD process.[41] The solid precursor metals are bombarded by a high energy source, for example, a beam of electrons or ions and release its atoms. The atoms then direct to the reaction chamber, where the coating substrate is put. The atoms either react with other gas-phase reactants or directly coated on the substrate surface to form a film.

Although CVD and PVD process can produce high quality $VO_2$ films, they require expensive equipment and complex operation. Also, for synthesizing a dual-functional coating, $VO_2$ is expected as fine solid particle instead of directly forming a film, which can be mixed into the copolymer. In addition, a solution-based process has the advantage

of cost-effectiveness and high-yield. Therefore, a solution-based synthesis method was of interest for this project.

**Solution-based process**

The sol-gel method has been intensively studied for $VO_2$ synthesis since it was first used in 1983.[42] It is one of the most common ways to synthesize $VO_2$ currently, as it can provide good control on the chemical composition, even in small quantities. Generally, an oxide network is formed by hydrolysis and polycondensation of chemical precursors in the liquid medium. Because of the self-assembly between precursor molecules, hydrogen bonds and Van de Waals interaction have obvious influence on the network growth.[43] In the sol-gel process, chemical precursor is first dissolved in solvent to produce a homogenous sol. The most common used precursor for $VO_2$ production is tetravalent alkoxide. Through condensation, the sol changes to a gel and the gel will be annealed at high temperature to get $VO_2$ crystal.[44]

Hydrothermal method is sensitive to the synthesis parameters, compared to sol-gel method. Therefore, the size, morphology and structure can be tuned by adjusting the synthesis time, temperature, concentration, pH value, pressure and so on. It has been investigated that different $VO_2$ morphologies depend on the solution pH value.[45, 46] $VO_2$ phase experiences a sequence transition of $VO_2(B)$-$VO_2(A)$-$VO_2(R/M)$ with pressure increase.[47] Vanadium pentoxide($V_2O_5$)[48] and vanadyl sulfate ($VOSO_4$)[49] are the most common precursors used for the hydrothermal method. Reduce agents, such as oxalic acid ($C_2H_2O_4$)[50] and hydrazine hydrate ($N_2H_4.H_2O$)[51], are usually chosen for reducing $V^{5+}$ to $V^{4+}$. Besides those, Alivio et al. used 2-propanol ($C_3H_8O$) and acetone (($CH_3$)$_2CO$) as the reducing agent and synthesized $VO_2$ nanobeam with dimension of $210 \pm 70$ nm x $4.0 \pm 3.0$ μm and $180 \pm 70$ nm x $1.6 \pm 0.9$ μm respectively.[48] Liang et al. proposed a new reductant, tartaric acid ($C_4H_6O_6$), for preparing W-doped $VO_2(M)$ nanorods.[18] $VO_2$ synthesized with tartaric acid experienced two step phase evolution of $VO_2(B)$ - $VO_2(R/M)$ instead of the traditional three steps, which makes higher yield and more suitable for large scale production.

Alie et al. successfully synthesized VO₂ using an inexpensive and scalable hydrothermal technology, with $V_2O_5$ and oxalic acid as precursors.[1] The reactants were continuously stirred to become a blue solution and placed in a Teflon-lined autoclave for 24 h. The effect of precursors' molar ratio, synthesis temperature and concentration were carefully studied. After hydrothermal treatment, the blue-black powder was collected, washed and dried under vacuum. This is a general synthesis process for hydrothermal method. It was found that high purity $VO_2(M)$ started to be produced, when the molar ratio of oxalic acid to $V_2O_5$ was greater than 3:1. The excess oxalic acid not only ensures the fully conversion of $V^{5+}$ to $V^{4+}$, but also adjusts the pH value of the mixture, which affects the resulting phase and morphology formation.[52] The synthesized VO₂ using a molar ratio of 2:1 gave nanorod morphology, as shown in Figure 2.3 (a). When the ratio of oxalic acid to $V_2O_5$ was increased to 3:1, both star and unique hollow sphere morphology were achieved, shown in Figure 2.3 (b) and (c). In addition, $VO_2(B)$ was observed at low synthesis temperature. With the hydrothermal temperature exceeded 260 °C, $VO_2(B)$ fully transferred to $VO_2(M)$.
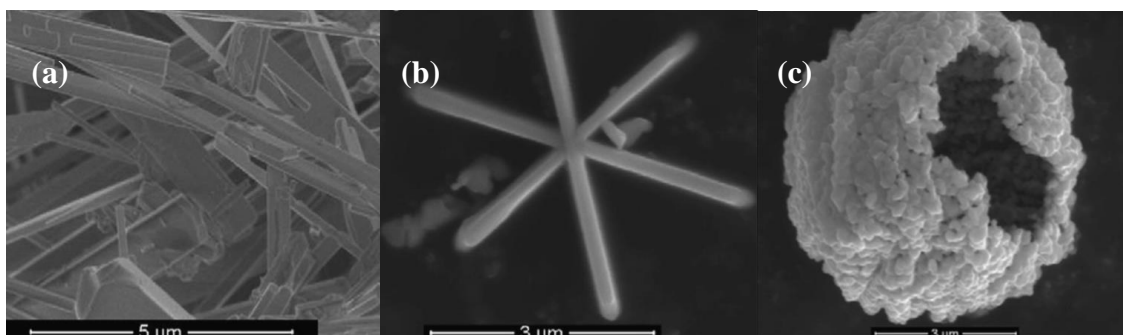


**Figure 2.3: SEM of VO₂ with (a) nanorod morphology using molar ratio of 2:1, (b) star and (c) hollow sphere morphology with molar ratio of 3:1.[1]**

To improve the stability in oxygen and water, a VO₂/Al-O core shell structure was proposed.[53] The Al-O-based shell kept VO₂ stable at high temperature (350 °C) in air, as well as in $H_2O_2$ solution. The functional time of its thermochromic property was also 6 times longer than normal hydrothermally synthesized VO₂. Similarly, Li et al. reported a VO₂@TiO₂ core-shell structure, which utilized TiO₂ overcoating to improve the luminous transmittance as well as enhance VO₂ stability against oxygen.[8]

Other solution-based processes includes polymer-assisted deposition (PAD) introduced by Gao's group, where $V_2O_5$ and hydrazinium chloride ($N_2H_4.HCl$) were used as precursors for preparing $VOCl_2$.[54] Polyvinylpyrrolidone (PVP) was added during the synthesis, which not only promoted film formation but also improved the purity of M/R phase $VO_2$. In addition, Tsuchiya's group successfully synthesized epitaxial $VO_2$ film on $TiO_2$ (001) substrates via photo-assisted chemical solution deposition.[55]

In summary, high quality $VO_2$ nanoparticles can be achieved by carefully adjusting hydrothermal synthesis parameters. Compared to other solution-based methods, one-step hydrothermal method offers a simpler and more cost-effective way to get $VO_2$ in solid powder form, which can easily be further treated. Therefore, hydrothermal method was used in my project for synthesizing thermochromic $VO_2$.

## 2.1.6 Thermochromic property

Thermochromic ability is the most important property of $VO_2$, which results in the energy conservation efficiency of smart windows. Two parameters that can reflect thermochromic performance are luminous transmittance ($T_{lum}$) and solar energy modulation ability ($\Delta T_{sol}$). $T_{lum}$ (380 nm-780 nm) and $T_{sol}$ (250 nm-2500 nm) can be calculated from the following equation:

$$T_{sol/lum} = \int \phi_{sol/lum}(\lambda)T(\lambda)d\lambda / \int \phi_{sol/lum}(\lambda)d\lambda$$

$\phi_{sol}$ represents the solar irradiation spectrum for air mass 1.5, which corresponds to the sun standing 37 ° above horizon.[56] $\phi_{lum}$ represents the function of standard luminous efficiency for human vision. $T(\lambda)$ is the transmittance within the specified wavelength range. $\Delta T_{sol}$ is defined by the different of $T_{sol}$ at low and high temperature.

$$\Delta T_{sol} = T_{sol}(T < Tc) - T_{sol}(T > Tc)$$

High $T_{lum}$ and high $\Delta T_{sol}$ value are expected for excellent performance of thermochromic smart window. However, the increase of $\Delta T_{sol}$ is usually at the cost of lower $T_{lum}$. Therefore, many researchers now focus on the solutions to overcome the challenge,

which can be categorized to: preparing $VO_2$ film in microstructure, integrating $VO_2$ in nanocomposite and optimizing the optical thin film.[14]

## 2.2 Antimicrobial agents

### 2.2.1 Multifunctional energy-efficient smart window with self-cleaning property

Due to the humidity in the air and moisture from rain and dew, bacteria or pollutants are easy to grow on windows, which raises health concerns and causes high cleaning costs. To solve the problem, many researches have examined producing multifunctional smart windows, for example performing both thermochromic and self-cleaning property.

$TiO_2$ has been studied for the preparation of multifunctional energy efficient window, due to its excellent photocatalytic degradation of bacteria. Powell et al proposed a layered $VO_2/SiO_2/TiO_2$ thin film using atmospheric-pressure chemical vapor deposition.[57] The film exhibited significant solar modulation ability as well as self-cleaning property, after $TiO_2$ illuminated by UV light. The self-cleaning property was tested against organic pollutant stearic acid. $SiO_2$ layer prevented the $Ti^{4+}$ ion diffusing into $VO_2$ layer and improved the optical property of $VO_2$ layer. Zheng et al. synthesized a $TiO_2(R)/VO_2/TiO_2(A)$ multilayer, where $TiO_2$ was directly deposited on $VO_2$ film without a barrier layer.[58] The bottom $TiO_2$ helped the formation of $VO_2$ layer and acted as an antireflection layer, while the top $TiO_2$ layer performed photo-catalytical property. Besides $TiO_2$, ZnO has also been studied for preparing multifunctional smart window. Jin's group prepared a $VO_2$@ZnO core-shell structure, which not only elevated the thermochromic property, but also improved $VO_2$ environmental durability.[59]

Many antimicrobial agents can be considered for preparing multifunctional energy-efficient coating with self-cleaning property. In this review section, various antimicrobial agents that are currently widely used are discussed and their mechanisms of killing contaminants are studied. The advantages and disadvantages of each agents are compared. The reasons for choosing quaternary ammonium compounds (QACs) for synthesizing dual-functional coating are illustrated as well.

## 2.2.2  Common antimicrobial agents and their mechanisms

Many materials have been used for antimicrobial agents, such as metal and metal oxide nanoparticles, antibiotics, antimicrobial polymers and halogens.[60, 61] When these antimicrobial agents are integrated in coating, antimicrobial surface is developed, which decreases bacteria livability based on contact killing, preventing bacteria attachment to the surface or leaching antimicrobial substance.[62] Two main types, antimicrobial nanoparticles and antimicrobial polymers, will be reviewed and discussed.

**Antimicrobial nanoparticles**

Metal nanoparticles have been studied for decades for antimicrobial purpose. Nanomaterials such as titanium, silver, zinc, copper and gold have already been widely used in food packaging, dental or medical fields. They exhibit significant antimicrobial ability on Gram-positive,  Gram-negative bacteria, mycobacteria and fungi. [63] Different morphologies, sizes and other physicochemical characteristics influence the antimicrobial performance. [64, 65]

Titanium dioxide is one of the most common antimicrobial nanoparticles, which has been studied for years, due to its photocatalytic property under UV activation. The mechanism includes several steps. $TiO_2$ generates electron-hole pair after exposed to UV light. The produced hole reacts with $H_2O$ or $OH^-$ and generates active hydroxyl radical. At the same time, electrons react with oxygen vacancies and produce superoxide ions. These reactive oxygen species (ROS) oxidize organic compounds, destroy the cell wall and cytoplasmic membrane, which leads to the bacteria death.[66] As the antimicrobial activity of $TiO_2$ is related with its photocatalytic property, many methods have been proposed to improve the photocatalytic efficiency.  Dawson et al. proposed a semiconductor/metal composite by reducing $HAuCl_4$ on $TiO_2$ nanoparticle, which improved 40 % oxidation efficiency by tailoring particle size and surface of $TiO_2$.[67] Similarly, Zhao's group successfully synthesized phosphate mesoporous titanium dioxide using phosphoric acid.[68] The reduced phosphorus improved stability of $TiO_2$ framework and increased the surface area, which greatly enhanced $TiO_2$ photocatalytic efficiency.
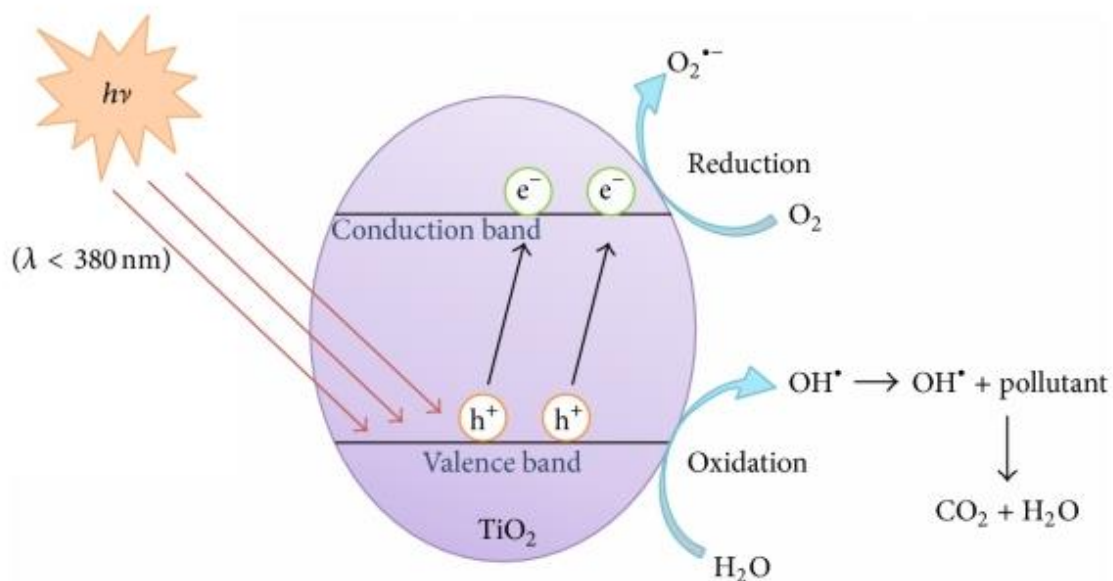
**Figure 2.4: Mechanism of TiO₂ photocatalysis.** [69]

Silver nanoparticles are now widely used in plastic, biomedical, pharmaceutical, food processing and coating-based materials. It has been reported that silver has excellent antimicrobial performance against many foodborne bacteria, such as E. coli, S. aureus and P. aeruginosa. [70] Silver NPs produces gaps and pits in the membrane of bacteria cell walls and the silver ions interact with enzymes inside the bacteria, which destroys the metabolic system and leads to the bacteria death.[71, 72] Silver nanoparticle has been proved having higher antibacterial ability than its ionic form.[73] Pal et al. studied the effect of different silver nanoparticle shapes on antimicrobial performance against Gram-negative bacteria E.coli. [74] It was found that the truncated triangular silver nanoparticle showed the most significant antimicrobial action among rod-shape and sphere-shape, due to its larger atom density surface.

Zinc oxide nanoparticles are considered as safe for contacting human skin. Therefore, it was usually used for food application or products for human body. Accurate antimicrobial mechanism for zinc oxide hasn't been completely explained. Proposed reasons for killing bacteria include the generation of hydrogen peroxide, the accumulation of particles on bacteria surface, ROS generation and zinc oxide release. It

has been reported that the antimicrobial efficiency of zinc oxide nanoparticles was improved when decreasing particle size and increasing the powder concentration. [75] What's more, ZnO nanoparticle also shows excellent photocatalysis and generates ROS after exposed to UV light, which improves its antimicrobial ability.[76]

**Antimicrobial Polymers**

Although antimicrobial metal/metal oxide nanoparticles have been widely used in many fields, respiratory and neurological damage, toxic effect on human health and circulatory issues of these nanoparticles raise safety concern.[77] Additionally, when antimicrobial nanoparticles are integrated into a polymer film, such as PMMA, most particles are immersed inside. As only particles on the surface of the film can contact bacteria and perform antibacterial property, the utilization is low in this case. What's more, the antimicrobial property of some nanoparticles needs to be activated by light within a certain wavelength range, which complicates the process and increases the operation cost. Therefore, antimicrobial polymers offer a better choice, because of their significant antimicrobial performance, minimized environmental pollution, less toxicity and longer lifetime.[78] Antimicrobial polymers structure can be controlled by different functional groups or comonomers using a copolymerization process. Three main types of antimicrobial polymers are discussed below.

Natural antimicrobial polymers include chitosan and poly-ε-lysine. Chitosan was first found by Rouget in 1859. Since then, it is widely used in the biomedical field. The interaction between Chitosan and bacteria, such as chelating effect, electrostatic interaction and hydrophobic influence, leads to the bacteria death. The dominant mechanism of Chitosan's antimicrobial activity depends on the pH value.[79] Poly-ε-lysine usually applied in food storage, disinfection, drug, gene delivery and so on.[80] It attracts bacteria through electrostatic adsorption and strips the outer membrane of bacteria. That leads to the physiological destroy and finally the death of the cell.[81]

Antimicrobial polymers containing halogen contain one or more halogen covalent bonds in the polymer. This kind of polymer is widely used in water disinfection, health care or painting. When the halogen polymers contact with bacteria, the reactive free halogens

transfer to the targeted site of protein receptor and result in the disfunction of bacteria.[82] The most common used halogen is chloride, however other halogens such as iodine and bromide have also been studied.[78]

Antimicrobial polymers containing nitrogen contains quaternary ammonium compounds, nitrogen containing polymer with ring structure, polyethyleneimine, polyguanidines and polymeric ionic liquid. The linear-structured quaternary ammonium compounds (QACs) has a general formula of $N^+R_1R_2R_3R_4X^-$, where X means an anion and R can represent a hydrogen, an alkyl group or other functional group taking place of alkyl group. The quaternary pyridinium is similar with QACs, which contains a heterocyclic ring with nitrogen atom. Although it shows obvious antimicrobial performance on both bacteria and yeast, toxicity of this compound raises health concern for human.[83] The mechanism of Polyethyleneimine's (PEI) antimicrobial activity is based on rupture of the cell membrane. However, positive charge density and hydrophobicity requirement for exhibiting antimicrobial property restricts its application.[84]

Among various antimicrobial polymers, QACs stand out due to their excellent antimicrobial efficiency, good environmental stability, low toxicity and corrosive and long life-time.[85, 86] Unlike halogen compounds gradually releasing active halogen species to the surrounding, it was found that QACs kill bacteria upon contact, without releasing toxic antimicrobial agents to the environment.[87, 88] As the agents are not released, it can retain its antimicrobial effect after several times usages, which results in longer lifetimes.[89] Besides, the structure of QACs can be easily modified and controlled by using different synthesis precursors. Therefore, QACs were chosen as antimicrobial agent for synthesizing dual-functional thermochromic/antimicrobial coating.

## 2.2.3 Quaternary Ammonium compounds (QACs)

QACs attract bacteria through ionic and hydrophobic interaction.The hydrophobic tail of QACs inserts into the lipid bilayer, which leads to the membrane rearrangement, denaturation of protein and enzyme and intercellular substances leakage.[90] The gram-negative bacteria has been proved to be more resistant to the antimicrobial ability of QACs. The cell wall of gram-positive bacteria is mainly composed of peptidoglycan,

which allows QACs easily to travel through. However, the two-membrane structure of gram-negative bacteria provides an additional protection. What's more, the two-membrane structure of gram-negative bacteria have efflux pumps to clear the lipophilic agent transferring through the periplasm. However, gram-positive bacteria do not have the ability of migratory capture of exogenous molecules, as the pump terminals are between the external environment and its internal cell.[91] Xu et al. investigated the effect of the length of methyl groups in QACs on antimicrobial property against E. coli bacteria. It was discovered that short length of methyl groups was not long enough to insert into the lipid bilayer, which led to no antibacterial efficiency.[92] On the other hand, Melo et al. synthesized hybrid PMMA coating with three different QACs: dioctadecyldimethyl ammonium bromide (DODAB), cetyltrimethylammonium bromide (CTAB), and tetrapropylammonium bromide (TPAB). Antimicrobial performance of these three QACs was studied, and it showed that a very long methyl group was too flexible to be able to infiltrate the cell membrane.[62] Previous research showed that QACs with 8-18 carbon exhibited excellent antimicrobial property. Among them, QACs with alkyl length of 12-14 have better antimicrobial ability against Gram-positive bacterial, while QACs with alkyl length of 14-16 show better antimicrobial performance against Gram-negative bacteria. [93] Zhao et al successfully synthesized a new QAC with a long perfluoroalkyl group tail[61]. The new QAC was covalently bonded into an acrylic coating through UV curing. Its antimicrobial ability was compared to that of QAC with long hydrocarbon tail. It was found that QACs with perfluoroalkyl tail exhibited superior antimicrobial ability against both Gram-positive and Gram-negative bacteria, due to its greater cationic charge density and lower surface energy. That made QACs enriched at the coating surface and increased the biocidal efficiency.
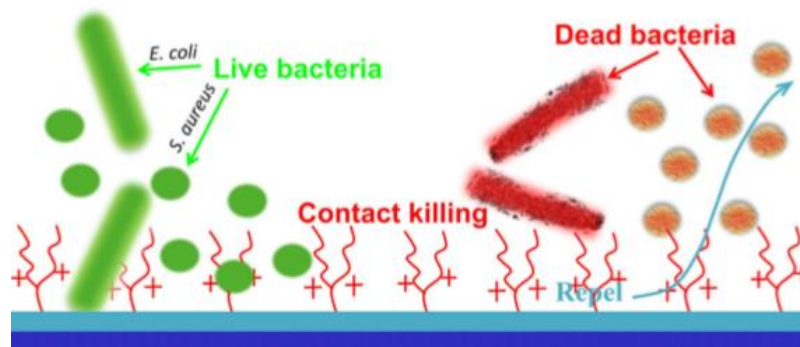
**Figure 2.5: Mechanism of antimicrobial activity of QACs. [94]**

Various methods have been investigated for grafting QACs to surfaces of materials, for example, hydrophobic interactions, sonication, electrostatic interaction, covalent linking as well as metal-coordination chemistry. Among them, covalent linkage is considered as the most effective and reliable method, as QACs are chemically bonded and not able to escape to the environment.[95] This ensures the contact killing principle of QACs, without leaching toxic biocide agents to the surrounding environment. Recently, Zhang et al. grafted QAC 2-dimethyl-2-hexadecayl-1-methyacryloxyethyl ammonium bromide (DEHMA) on polyester with acrylic acid using electron-beam irradiation.[96] Ag nanoparticles were induced by deposited on the site of carboxyl groups in acrylic acid. The results showed improved antimicrobial efficiency.

In brief, for preparing dual-functional coating, $VO_2$ (M) nanoparticles and a synthesized QAC named N,N-dimethyl-N-{2-[(2-methylprop-2-enoyl)oxy]ethyl}undecane-1-aminium bromide (dMEMUABr) with a hydrocarbon tail of 11 carbon atoms were chosen for performing thermochromic and antimicrobial property. MMA monomer was used for covalent linkage with dMEMUABr, because of its light weight, excellent characteristic, colorless and high transparency.[97]

## 2.3 Reactivity ratio

As the antimicrobial agent dMEMUABr was polymerized with MMA for synthesizing a dual-functional coating, further investigation of the sequence distribution of dMEMUABr

and MMA monomers in the copolymer coating is desired. Different sequence distributions and compositional heterogeneity greatly affect the chemical and physical property of the copolymer.[98] Yao et al. studied amine based copolymer with four different sequence structures, which were diblock (poly(dimethylamino-2-ethyl methacrylate-b-methyl methacrylate) (poly(MMA-b-DMAEMA))), four-armed diblock (poly(MMA-b-DMAEMA)4), triblock (poly(DMAEMA-b-MMA-b-DMAEMA)), and random (poly(MMA-r-DMAEMA)).[99] They showed different performance in retention ratio, surface enrichment ratio and durability.

In the copolymerization system of two monomers, four propagation reactions may occur (eq 1, 2, 3 & 4), as either monomer can be added to the last propagating chain end. $M_1^*$, $M_2^*$ represent the propagating ends and $M_1$, $M_2$ represent the monomers.[100] The k value is the rate constant, which determines the compositional profile. Theoretically, the reactivity ratio is the ratio of its homo-polymerization rate constant versus the cross-propagating rate constant with the other monomer.[101] (eq 5) Therefore, reactivity ratio offers importance information for prediction of copolymer composition as well as the structure.[102] It also helps to understand the kinetic and mechanistic perspective of the copolymerization.

$$\sim M_1^* + M_1 \xrightarrow{k11} \sim M_1 M_1^* \ (1)$$

$$\sim M_1^* + M_2 \xrightarrow{k12} \sim M_1 M_2^* \ (2)$$

$$\sim M_2^* + M_1 \xrightarrow{k21} \sim M_2 M_1^* \ (3)$$

$$\sim M_2^* + M_2 \xrightarrow{k22} \sim M_2 M_2^* \ (4)$$
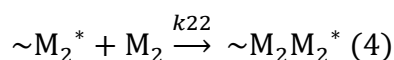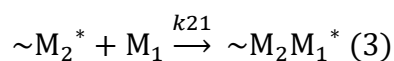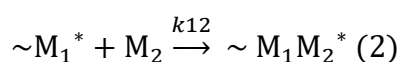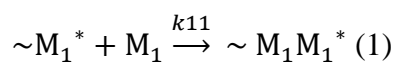
$$r_1 = \frac{k_{11}}{k_{12}} \ ; \ r_2 = \frac{k_{22}}{k_{21}} \ (5)$$

The well-known Mayo-Lewis equation was generated from the copolymer composition equation. (eq 6). The Mayo-Lewis equation (eq 7) describes the relationship between the mole fraction of monomer 1 in the feed $f_1$ and in the copolymer $F_1$ in terms of the

reactivity ratio $r_1$ and $r_2$.[103] Once data for $f_1$ and $F_1$ are known, the reactivity ratios can be calculated using the Mayo-Lewis equation through the non-linear least squares (NLLS) method.

$$\frac{d[M_1]}{d[M_2]} = \frac{[M_1](r_1[M_1]+[M_2])}{[M_2]([M_1]+r_2[M_2])} \quad (6)$$

$$F_1 = \frac{r_1{f_1}^2+f_1(1-f_1)}{r_1{f_1}^2+2f_1(1-f_1)+r_2(1-f_1)^2} \quad (7)$$

## 2.3.1 Linear and non-linear least squares method for reactivity ratio determination

The first linear calculation method was proposed by Fineman and Ross according to the Mayo-Lewis equation.[104] The Fineman-Ross (F-R) equation is:

$$G = r_1 H - r_2 \quad (8)$$

$$\text{where } G = \frac{f_1(2F_1-1)}{(1-f_1)F_1}; H = \frac{{f_1}^2(1-F_1)}{(1-f_1)^2F_1}$$

Through the plot of H versus G, a straight line will be achieved. The slope of the line gives $r_1$ and the intercept gives the $r_2$ value. Similarly, Yezrielev et al. proposed another equation for reactivity ratio calculation (Yezrielev-Brokhina-Roskin (Y-B-R) method):

$$G = r_1 H^{3/2} - r_2 \quad (9)$$

However, the limitation in previous methods is that the high and low concentration data are equally valued, which affects the correct estimation of reactivity ratio. Kelen and Tüdös induced an arbitrary positive constant $\alpha$ to spread the data more evenly and gave equal weight to all data points.[105] The Kelen-Tüdös (K-T) equation is:

$$\eta = \left[r1 + \frac{r_2}{\alpha}\right]\mu - \frac{r_2}{\alpha} \quad (10)$$

$$\text{where } \alpha = (H_{min}H_{max})^{0.5}; \eta = \frac{G}{(\alpha+H)}; \mu = \frac{H}{(\alpha+H)}$$

By plotting the data of μ versus η, reactivity ratio $r_1, r_2$ can be calculated from the slope and intercept. These three methods are the most commonly used linear methodology for reactivity ratio calculation.

 In 1987, O'Driscoll and Reilly pointed out the limitations of linear least squares method.[106] They proposed that linear methods led to an incorrect estimate, and non-linear least squares method was the most sound technique. The non-linear method currently used was developed by Mortimer and Tidwell.[107] Briefly, an initial assumption value was given to the reactivity ratio $r_1$, $r_2$. The sum of the squares of the difference between the experimental copolymer composition data and computer calculated ones is minimized through multiple times of calculation. In this method, once the error criteria is set, only one pair of reactivity ratio value can be achieved for a given set of data.

## 2.3.2   In-situ NMR technique for reactivity ratio determination

In the conventional low-conversion technique for reactivity calculation, a large number of experiments is required. Monomers with different concentration ratios need to be prepared, and the conversion during the copolymerization needs to be limited to less than 10-15 %.[108] The low conversion (10-15 %) required is difficult to be controlled.[109, 110] Therefore, an in-situ NMR technique offers a more efficient way for reactivity ratio calculation. It can monitor the real-time concentration data of individual monomers as well as the continuously formed copolymer as a function of reaction progress.[111] In addition to in-situ NMR, in-situ FTIR also provides on-line tracking of monomer concentration.[112-114] However, in-situ FTIR needs clear adsorption peaks. The monomers' peaks need to be different enough from the copolymer's peaks, which is difficult for many FTIR instruments. In this case, NMR has greater selectivity and resolution, compared to FTIR. NMR is more sensitive towards the variations.[115] For application of the in-situ NMR technique, three criteria have been proposed: (1) the copolymerization reaction rate needs to be lower than the scanning rate, (2) the monomer and copolymer's characteristic peaks should be distinguishable from each other, (3) the copolymer is soluble in the solvent.[116, 117]

In-situ NMR technique has been applied for determining reactivity ratio of various comonomer pairs. Hutchinson's group investigated the aqueous phase copolymerization of acrylamide (AM) and acrylic acid (AA) with in-situ NMR.[117] The monomer mixture was scanned every two minutes until full conversion at 40 °C. Abdollahi et al. studied the free-radical copolymerization of styrene and ethyl acrylate at 70 °C.[118] The composition of each unit in copolymer F was considered as the reduction of each monomer versus the total reduction of two monomers. The reactivity ratio was determined by various linear and non-linear method at low and high conversions and compared. Similarly, Pugh's group studied the reactivity ratio of styrene with methyl methacrylate, 2-(N-ethylperfluorooctanesulfonamido)ethyl acrylate (FOSA) with N,N-dimethylacrylamide (DMA) and 2-(N-ethylperfluorooctanesulfonamido)ethyl methacrylate (FOSM) with DMA using pyridazine as the internal reference.[119] Previous work from our group reported the reactivity ratio of methyl methacrylate and diallyl dimethylammonium chloride using in-situ NMR.[120] The copolymerization was carried out at different temperatures, which showed no obvious influence on the reactivity ratio values. Direct numerical differential method and numerical solution differential method were used for calculating the copolymer composition. These investigations all illustrate the stability, efficiency and simplicity of the in-situ NMR technique in determining reactivity ratios.

## 2.3.3   Sequence prediction with reactivity ratio

The reactivity ratios of a pair of two monomers $r_1$, $r_2$ in a system indicates the sequence distribution in the copolymer. When $r_1r_2=1$, the copolymerization is considered as ideal polymerization, as the propagating end shows equal preference to both monomers. In this case, there are three possibilities. When $r_1=1$, $r_2=1$, two monomers show the same reactivity. Therefore, the copolymer composition equals the feed composition with a random sequence of two monomers.[121] When $r_1>1$, $r_2<1$ or $r_1<1$, $r_2<1$, the one higher than unity is more active, adding to the propagating end. The copolymer will contain more fragments of that monomer in a random sequence.

When $r_1r_2=0$ or $r_1$, $r_2$ are both very small numbers, the sequence tends to be alternative. The two types of propagating end prefer to add the other monomer. Therefore, the

composition of each monomer in the copolymer is 0.5. The extreme example is $r_1 \gg r_2$ and $r_1 r_2 = 0$, where $M_1$ is more active to be added to the propagating species.

When $r_1 > 1$, $r_2 > 1$ or $r_1 r_2 > 0$, block copolymers will be formed. In the long polymer chain, there is one or more long continuously sequence of each monomer.[100]
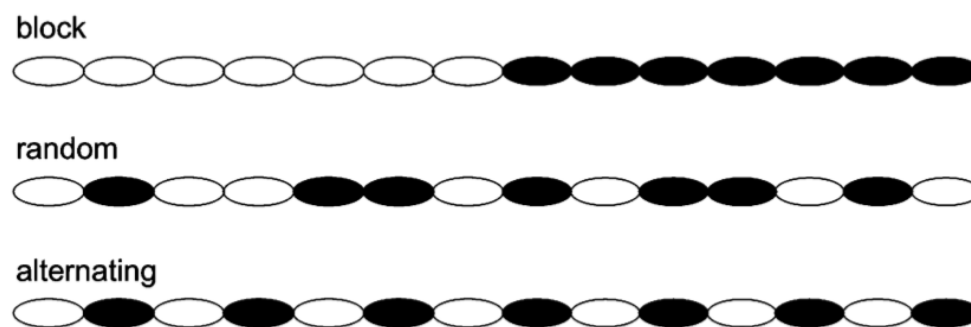


**Figure 2.6: Schematic of block, random and alternative copolymer sequence.[122]**

## 2.3.4 UV initiated copolymerization

When studying the reactivity ratio of monomer pairs, copolymerization reaction is commonly initiated by heat, with thermal initiator producing free radicals and initiating the copolymerization.[123, 124] However, another free radical copolymerization method, UV initiated copolymerization, has been widely used in many applications, such as coating, packaging, semiconductors and so on. As antimicrobial coatings using QAC dMEMUABr and MMA monomer were successfully synthesized via UV curing in the previous chapter, investigating the reactivity ratio of these two monomers under UV initiated copolymerization has significant meaning.

A limited number of papers have been published on the determination of reactivity ratios in UV initiated copolymerization. Zhang et al. studied the reactivity ratio of dimethyldiallylammonium chloride (DMD) and acrylamide (AM) in UV initiated polymerization for improving the flocculant performance of removing suspended solids from wastewater.[125] Different reaction material ratios were prepared, and the total

conversion was controlled less than 15 % by shortening the UV exposure time. They also investigated the effect of the template sodium polyacrylate added to the polymerization system, which was reported to interact with monomers by van der Waals forces, electrostatic forces or hydrogen bond and improve the performance of the copolymer.[126, 127] It was found that the template improved the reactivity ratio of DMD, increased its length and number in the copolymer and decreased the viscosity of the copolymer. Patton et al. proposed a measurement method for monomer reactivity ratio using X-ray photoelectron spectroscopy (XPS).[128, 98] They synthesized a polymer brush by attaching an asymmetric trichlorosilyl-functionalized azo initiator to a -OH-terminated silicon wafer and polymerizing MMA and styrene on the azo-functionalized substrate by UV irradiation. The reactivity ratio's measurement by XPS also relied on the distinguishable chemical species of monomers. Similarly, Zheng's group determined the reactivity ratio of acrylamide (AM) and methacryloxyethyltrimethyl ammonium chloride (DMC) through UV initiation.[129] The composition of the copolymer was specified by silver nitrate titration, followed by Fineman-Ross, Kelen-Tudos and Yezrielev-Brokhina-Roskin methods to determine the reactivity ratio.

In this review, the reasons for choosing $VO_2$ and QACs for thermochromic/antimicrobial dual-functional coating preparation were fully explained. Different synthesis methods of $VO_2$ were compared, and the mechanism of QACs' antimicrobial ability against bacteria was illustrated. What's more, for the determination of reactivity ratios, detailed information of in-situ NMR technique was investigated, which has been shown to be a more efficient way compared to the conventional low-conversion technique. Various LLS and NLLS calculation methods were shown. Latest researches on reactivity ratio under UV initiated copolymerization were studied.

## 2.4 References

[1] Alie D, Gedvilas L, Wang Z, et al. Direct synthesis of thermochromic VO2 through hydrothermal reaction [J]. Journal of Solid State Chemistry, 2014, 212:237-241.

[2] Chang T-C, Cao X, Bao S-H, et al. Review on thermochromic vanadium dioxide based smart coatings: from lab to commercial application [J]. Advances in Manufacturing, 2018, 6 (1):1-19.

[3] Omer AM. Energy, environment and sustainable development [J]. Renewable and Sustainable Energy Reviews, 2008, 12 (9):2265-2300.

[4] Pérez-Lombard L, Ortiz J, Pout C. A review on buildings energy consumption information [J]. Energy and Buildings, 2008, 40 (3):394-398.

[5] Baetens R, Jelle BP, Gustavsen A. Properties, requirements and possibilities of smart windows for dynamic daylight and solar energy control in buildings: A state-of-the-art review [J]. Solar Energy Materials and Solar Cells, 2010, 94 (2):87-105.

[6] Long L, Ye H. How to be smart and energy efficient: a general discussion on thermochromic windows [J]. Sci Rep, 2014, 4:6427.

[7] Todd ECd, Baker N 2018. E. coli Infection in Canada [M], The Canadian Encyclopedia, 8th edn.

[8] Li Y, Ji S, Gao Y, et al. Core-shell VO2@TiO2 nanorods that combine thermochromic and photocatalytic properties for application as energy-saving smart coatings [J]. Sci Rep, 2013, 3:1370.

[9] Ke Y, Zhou C, Zhou Y, et al. Emerging Thermal-Responsive Materials and Integrated Techniques Targeting the Energy-Efficient Smart Window Application [J]. Advanced Functional Materials, 2018, 28 (22):1800113.

[10] Granqvist CG, Arvizu MA, Bayrak Pehlivan İ, et al. Electrochromic materials and devices for energy efficiency and human comfort in buildings: A critical review [J]. Electrochimica Acta, 2018, 259:1170-1182.

[11] Wang WQ, Wang XL, Xia XH, et al. Enhanced electrochromic and energy storage performance in mesoporous WO3 film and its application in a bi-functional smart window [J]. Nanoscale, 2018, 10 (17):8162-8169.

[12] Bella F, Leftheriotis G, Griffini G, et al. A New Design Paradigm for Smart Windows: Photocurable Polymers for Quasi-Solid Photoelectrochromic Devices with Excellent Long-Term Stability under Real Outdoor Operating Conditions [J]. Advanced Functional Materials, 2016, 26 (7):1127-1137.

[13] Morin FJ. Oxides Which Show a Metal-to-Insulator Transition at the Neel Temperature [J]. Physical Review Letters, 1959, 3 (1):34-36.

[14] Cui Y, Ke Y, Liu C, et al. Thermochromic VO2 for Energy-Efficient Smart Windows [J]. Joule, 2018, 2 (9):1707-1746.

[15] Li M, Magdassi S, Gao Y, et al. Hydrothermal Synthesis of VO2 Polymorphs: Advantages, Challenges and Prospects for the Application of Energy Efficient Smart Windows [J]. Small, 2017, 13 (36).

[16] Wu C, Feng F, Xie Y. Design of vanadium oxide structures with controllable electrical properties for energy applications [J]. Chem Soc Rev, 2013, 42 (12):5157-5183.

[17] Zhang J, Tian H, Hao L, et al. Thermochromic VO2 films from ammonium citrato-oxovanadate(iv) with excellent optical and phase transition properties [J]. Journal of Materials Chemistry C, 2016, 4 (23):5281-5288.

[18] Liang S, Shi Q, Zhu H, et al. One-Step Hydrothermal Synthesis of W-Doped VO2 (M) Nanorods with a Tunable Phase-Transition Temperature for Infrared Smart Windows [J]. ACS Omega, 2016, 1 (6):1139-1148.

[19] Hong W-K, Cha S, Sohn JI, et al. Metal-Insulator Phase Transition in Quasi-One-Dimensional VO2Structures [J]. Journal of Nanomaterials, 2015, 2015:1-15.

[20] Haverkort MW, Hu Z, Tanaka A, et al. Orbital-assisted metal-insulator transition in VO2 [J]. Phys Rev Lett, 2005, 95 (19):196404.

[21] Whittaker L, Patridge CJ, Banerjee S. Microscopic and Nanoscale Perspective of the Metal−Insulator Phase Transitions of VO2: Some New Twists to an Old Tale [J]. The Journal of Physical Chemistry Letters, 2011, 2 (7):745-758.

[22] Goodenough JB. The two components of the crystallographic transition in VO2 [J]. Journal of Solid State Chemistry, 1971, 3:490-500.

[23] Aetukuri NB, Gray AX, Drouard M, et al. Control of the metal–insulator transition in vanadium dioxide by modifying orbital occupancy [J]. Nature Physics, 2013, 9 (10):661-666.

[24] Yao T, Zhang X, Sun Z, et al. Understanding the nature of the kinetic process in a VO2 metal-insulator transition [J]. Phys Rev Lett, 2010, 105 (22):226405.

[25] Xu F, Cao X, Luo H, et al. Recent advances in VO2-based thermochromic composites for smart windows [J]. Journal of Materials Chemistry C, 2018, 6 (8):1903-1919.

[26] Whittaker L, Wu T-L, Patridge CJ, et al. Distinctive finite size effects on the phase diagram and metal–insulator transitions of tungsten-doped vanadium(iv) oxide [J]. Journal of Materials Chemistry, 2011, 21 (15):5580.

[27] Lv Y, Le J, Chen H, et al. Influence of Nb doping on the phase transition properties of VO2 thin films prepared by ion beam co-sputtering deposition [J]. 2017, 10255:1025558.

[28] Khan GR, Asokan K, Ahmad B. Room temperature tunability of Mo-doped VO 2 nanofilms across semiconductor to metal phase transition [J]. Thin Solid Films, 2017, 625:155-162.

[29] Mai LQ, Hu B, Hu T, et al. Electrical Property of Mo-Doped VO2 Nanowire Array Film by Melting−Quenching Sol−Gel Method [J]. J. Phys. Chem. B, 2006, 110 (39):19083-19086.

[30] Piccirillo C, Binions R, Parkin IP. Nb-Doped VO2 Thin Films Prepared by Aerosol-Assisted Chemical Vapour Deposition [J]. European Journal of Inorganic Chemistry, 2007, 2007 (25):4050-4055.

[31] Tang C, Georgopoulos P, Fine ME, et al. Local atomic and electronic arrangements inWxV1−xO2 [J]. Physical Review B, 1985, 31 (2):1000-1011.

[32] Hu Y, Shi Q, Huang W, et al. Preparation and phase transition properties of Ti-doped VO2 films by sol–gel process [J]. Journal of Sol-Gel Science and Technology, 2015, 78 (1):19-25.

[33] Wang S, Liu M, Kong L, et al. Recent progress in VO2 smart coatings: Strategies to improve the thermochromic properties [J]. Progress in Materials Science, 2016, 81:1-54.

[34] Miyazaki K, Shibuya K, Suzuki M, et al. Correlation between thermal hysteresis width and broadening of metal–insulator transition in Cr- and Nb-doped VO2films [J]. Japanese Journal of Applied Physics, 2014, 53 (7):071102.

[35] Cyrot M. Theory of mott transition : Applications to transition metal oxides [J]. Journal de Physique, 1972, 33 (1):125-134.

[36] Zhang J, He H, Xie Y, et al. Giant reduction of the phase transition temperature for beryllium doped VO2 [J]. Phys Chem Chem Phys, 2013, 15 (13):4687-4690.

[37] Koide S, Takei H. Epitaxial Growth of VO2 Single Crystals and Their Anisotropic Properties in Electrical Resistivities [J]. J. Phys. Soc. Jpn, 1967, 22:946-947.

[38] Warwick MEA, Binions R. Chemical vapour deposition of thermochromic vanadium dioxide thin films for energy efficient glazing [J]. Journal of Solid State Chemistry, 2014, 214:53-66.

[39] Warwick MEA, Roberts AJ, Slade RCT, et al. Electric field assisted chemical vapour deposition – a new method for the preparation of highly porous supercapacitor electrodes [J]. J. Mater. Chem. A, 2014, 2 (17):6115-6120.

[40] Naik AJT, Bowman C, Panjwani N, et al. Electric field assisted aerosol assisted chemical vapour deposition of nanostructured metal oxide thin films [J]. Thin Solid Films, 2013, 544:452-456.

[41] Pahade VS, Chavan PS, Baisane VP. A review paper on Vapour deposition coating [J]. International Journal of Engineering and Applied Sciences (IJEAS), 2016, 3 (6).

[42] Greenberg CB. Undoped and doped VO2 films grown from VO(OC3H7)3 [J]. Thin Solid Films, 1983, 110:73-82.

[43] Livage J, Henry M, Sanchez C. Sol-gel chemistry of transition metal oxides [J]. Prog. Solid St. Chem., 1988, 18:259-341.

[44] Seyfouri MM, Binions R. Sol-gel approaches to thermochromic vanadium dioxide coating for smart glazing application [J]. Solar Energy Materials and Solar Cells, 2017, 159:52-65.

[45] Liu J, Li Q, Wang T, et al. Metastable vanadium dioxide nanobelts: hydrothermal synthesis, electrical transport, and magnetic properties [J]. Angew Chem Int Ed Engl, 2004, 43 (38):5048-5052.

[46] Xu Y, Huang W, Shi Q, et al. Porous nano-structured VO2 films with different surfactants: synthesis mechanisms, characterization, and applications [J]. Journal of Materials Science: Materials in Electronics, 2013, 24 (10):3823-3829.

[47] Ji S, Zhang F, Jin P. Selective formation of VO2(A) or VO2(R) polymorph by controlling the hydrothermal pressure [J]. Journal of Solid State Chemistry, 2011, 184 (8):2285-2292.

[48] Alivio TEG, Sellers DG, Asayesh-Ardakani H, et al. Postsynthetic Route for Modifying the Metal—Insulator Transition of VO2 by Interstitial Dopant Incorporation [J]. Chemistry of Materials, 2017, 29 (12):5401-5412.

[49] Li W, Ji S, Li Y, et al. Synthesis of VO2 nanoparticles by a hydrothermal-assisted homogeneous precipitation approach for thermochromic applications [J]. RSC Adv., 2014, 4 (25):13026-13033.

[50] Dong B, Shen N, Cao C, et al. Phase and morphology evolution of VO2 nanoparticles using a novel hydrothermal system for thermochromic applications: the growth mechanism and effect of ammonium (NH4+) [J]. RSC Advances, 2016, 6 (85):81559-81568.

[51] Wang N, Duchamp M, Xue C, et al. Single-Crystalline W-Doped VO2Nanobeams with Highly Reversible Electrical and Plasmonic Responses Near Room Temperature [J]. Advanced Materials Interfaces, 2016, 3 (15):1600164.

[52] Ji S, Zhao Y, Zhang F, et al. Direct formation of single crystal VO2(R) nanorods by one-step hydrothermal treatment [J]. Journal of Crystal Growth, 2010, 312 (2):282-286.

[53] Tong K, Li R, Zhu J, et al. Preparation of VO 2 /Al-O core-shell structure with enhanced weathering resistance for smart window [J]. Ceramics International, 2017, 43 (5):4055-4061.

[54] Kang L, Gao Y, Luo H. A novel solution process for the synthesis of VO2 thin films with excellent thermochromic properties [J]. ACS Appl Mater Interfaces, 2009, 1 (10):2211-2218.

[55] Nishikawa M, Nakajima T, Kumagai T, et al. Photoassisted chemical solution deposition method for fabricating uniformly epitaxial VO2 films [J]. Applied Physics A, 2010, 100 (1):297-303.

[56] Zhao L, Miao L, Liu C, et al. Solution-processed VO2-SiO2 composite films with simultaneously enhanced luminous transmittance, solar modulation ability and anti-oxidation property [J]. Sci Rep, 2014, 4:7000.

[57] Powell MJ, Quesada-Cabrera R, Taylor A, et al. Intelligent Multifunctional VO2/SiO2/TiO2 Coatings for Self-Cleaning, Energy-Saving Window Panels [J]. Chemistry of Materials, 2016, 28 (5):1369-1376.

[58] Zheng J, Bao S, Jin P. TiO2(R)/VO2(M)/TiO2(A) multilayer film as smart window: Combination of energy-saving, antifogging and self-cleaning functions [J]. Nano Energy, 2015, 11:136-145.

[59] Chen Y, Zeng X, Zhu J, et al. High Performance and Enhanced Durability of Thermochromic Films Using VO2@ZnO Core-Shell Nanoparticles [J]. ACS Appl Mater Interfaces, 2017, 9 (33):27784-27791.

[60] Cherdtrakulkiat R, Boonpangrak S, Sinthupoom N, et al. Derivatives (halogen, nitro and amino) of 8-hydroxyquinoline with highly potent antimicrobial and antioxidant activities [J]. Biochem Biophys Rep, 2016, 6:135-141.

[61] Zhao J, Millians W, Tang S, et al. Self-Stratified Antimicrobial Acrylic Coatings via One-Step UV Curing [J]. ACS Appl Mater Interfaces, 2015, 7 (33):18467-18472.

[62] Melo LD, Palombo RR, Petri DF, et al. Structure-activity relationship for quaternary ammonium compounds hybridized with poly(methyl methacrylate) [J]. ACS Appl Mater Interfaces, 2011, 3 (6):1933-1939.

[63] Wang L, Hu C, Shao L. The antimicrobial activity of nanoparticles: present situation and prospects for the future [J]. Int J Nanomedicine, 2017, 12:1227-1249.

[64] Mohammadi G, Valizadeh H, Barzegar-Jalali M, et al. Development of azithromycin-PLGA nanoparticles: physicochemical characterization and antibacterial effect against Salmonella typhi [J]. Colloids Surf B Biointerfaces, 2010, 80 (1):34-39.

[65] Seil JT, Webster TJ. Antimicrobial applications of nanotechnology: methods and literature [J]. Int J Nanomedicine, 2012, 7:2767-2781.

[66] Linsebigler AL, Lu G, John T. Yates J. Photocatalysis on TiO2 Surfaces Principles, Mechanisms, and Selected Results [J]. Chem. Rev., 1995, 95:735-758.

[67] Dawson A, Kamat PV. Semiconductor−Metal Nanocomposites. Photoinduced Fusion and Photocatalysis of Gold-Capped TiO2 (TiO2Gold) Nanoparticles [J]. J. Phys. Chem. B, 2001, 105:960-966.

[68] Yu JC, Zhang L, Zheng Z, et al. Synthesis and Characterization of Phosphated Mesoporous Titanium Dioxide with High Photocatalytic Activity [J]. Chem. Mater., 2003, 15:2280-2286.

[69] Feng T, Feng GS, Yan L, et al. One-Dimensional Nanostructured TiO2for Photocatalytic Degradation of Organic Pollutants in Wastewater [J]. International Journal of Photoenergy, 2014, 2014:1-14.

[70] Birla SS, Tiwari VV, Gade AK, et al. Fabrication of silver nanoparticles by Phoma glomerata and its combined effect against Escherichia coli, Pseudomonas aeruginosa and Staphylococcus aureus [J]. Lett Appl Microbiol, 2009, 48 (2):173-179.

[71] Egger S, Lehmann RP, Height MJ, et al. Antimicrobial properties of a novel silver-silica nanocomposite material [J]. Appl Environ Microbiol, 2009, 75 (9):2973-2976.

[72] Yun H, Kim JD, Choi HC, et al. Antibacterial Activity of CNT-Ag and GO-Ag Nanocomposites Against Gram-negative and Gram-positive Bacteria [J]. Bulletin of the Korean Chemical Society, 2013, 34 (11):3261-3264.

[73] Jo Y-K, Kim BH, Jung G. Antifungal Activity of Silver Ions and Nanoparticles on Phytopathogenic Fungi [J]. APS Publications, 2009.

[74] Pal S, Tak YK, Song JM. Does the antibacterial activity of silver nanoparticles depend on the shape of the nanoparticle? A study of the Gram-negative bacterium Escherichia coli [J]. Appl Environ Microbiol, 2007, 73 (6):1712-1720.

[75] Yamamoto O. Influence of particle size on the antibacterial activity of zinc oxide [J]. International Journal of Inorganic Materials, 2001, 3: 643–646.

[76] Khezerlou A, Alizadeh-Sani M, Azizi-Lalabadi M, et al. Nanoparticles and their antimicrobial properties against pathogens including bacteria, fungi, parasites and viruses [J]. Microbial Pathogenesis, 2018, 123:505-526.

[77] Auffan M, Rose J, Wiesner MR, et al. Chemical stability of metallic nanoparticles: a parameter controlling their potential cellular toxicity in vitro [J]. Environ Pollut, 2009, 157 (4):1127-1133.

[78] Jain A, Duvvuri LS, Farah S, et al. Antimicrobial polymers [J]. Adv Healthc Mater, 2014, 3 (12):1969-1985.

[79] Kong M, Chen XG, Liu CS, et al. Antibacterial mechanism of chitosan microspheres in a solid dispersing system against E. coli [J]. Colloids Surf B Biointerfaces, 2008, 65 (2):197-202.

[80] Shih IL, Shen MH, Van YT. Microbial synthesis of poly(epsilon-lysine) and its various applications [J]. Bioresour Technol, 2006, 97 (9):1148-1159.

[81] Shima S, Fukuhara Y, Sakai H. Inactivation of Bacteriophages byε-Poly-l-lysine Produced byStreptomyces [J]. Agricultural and Biological Chemistry, 2014, 46 (7):1917-1919.

[82] Denyera SP, Stewartb GSAB. Mechanisms of action of disinfectants [J]. International Biodeterioration & Biodegradation, 1998, 41:261-268.

[83] LI G, SHEN J, ZHU Y. Study of pyridinium‐type functional polymers. II. Antibacterial activity of soluble pyridinium‐type polymers [J]. Appl Polm Sci, 1998, 67:1761‐1768.

[84] Jian Lin, Shuyi Qiu, Kim Lewis, et al. Bactericidal properties of flat surfaces and nanoparticles derivatized with alkylated polyethylenimines. [J]. Biotechnol. Prog., 2002, 18:1082−1086.

[85] Jampala SN, Sarmadi M, Somers EB, et al. Plasma-enhanced synthesis of bactericidal quaternary ammonium thin layers on stainless steel and cellulose surfaces [J]. Langmuir, 2008, 24 (16):8583-8591.

[86] Roy D, Knapp JS, Guthrie JT, et al. Antibacterial cellulose fiber via RAFT surface graft polymerization [J]. Biomacromolecules, 2008, 9 (1):91-99.

[87] Elena P, Miri K. Formation of contact active antimicrobial surfaces by covalent grafting of quaternary ammonium compounds [J]. Colloids Surf B Biointerfaces, 2018, 169:195-205.

[88] Hui F, Debiemme-Chouvy C. Antimicrobial N-halamine polymers and coatings: a review of their synthesis, characterization, and applications [J]. Biomacromolecules, 2013, 14 (3):585-601.

[89] Kenawy E-R, Worley SD, Broughton§ R. The Chemistry and Applications of Antimicrobial Polymers  A State-of-the-Art Review [J]. American Chemical Society, 2007, 8.

[90] Ioannou CJ, Hanlon GW, Denyer SP. Action of disinfectant quaternary ammonium compounds against Staphylococcus aureus [J]. Antimicrob Agents Chemother, 2007, 51 (1):296-306.

[91] Wickham G. An investigation into the relative resistances of common bacterial pathogens to quaternary ammonium cation disinfectants [J]. Bioscience Horizons, 2017, 10.

[92] Xu WZ, Yang L, Charpentier PA. Preparation of Antibacterial Softwood via Chemical Attachment of Quaternary Ammonium Compounds Using Supercritical CO2 [J]. ACS Sustainable Chemistry & Engineering, 2016, 4 (3):1551-1561.

[93] Gilbert P, Moore LE. Cationic antiseptics: diversity of action under a common epithet [J]. J Appl Microbiol, 2005, 99 (4):703-715.

[94] He W, Zhang Y, Li J, et al. A Novel Surface Structure Consisting of Contact-active Antibacterial Upper-layer and Antifouling Sub-layer Derived from Gemini Quaternary Ammonium Salt Polyurethanes [J]. Sci Rep, 2016, 6:32140.

[95] Appendinia P, Hotchkissb JH. Review of antimicrobial food packaging [J]. 2002, 3:113-126.

[96] Zhang S, Li R, Huang D, et al. Antibacterial modification of PET with quaternary ammonium salt and silver particles via electron-beam irradiation [J]. Mater Sci Eng C Mater Biol Appl, 2018, 85:123-129.

[97] Ergün Y, Dirier C, Tanoğlu M. Polymethyl methacrylate based open-cell porous plastics for high-pressure ceramic casting [J]. Materials Science and Engineering: A, 2004, 385 (1-2):279-285.

[98] Patton DL, Page KA, Hoff EA, et al. A robust and high-throughput measurement platform for monomer reactivity ratios from surface-initiated polymerization [J]. Polymer Chemistry, 2012, 3 (5):1174.

[99] Yao Z, Cui Y, Zheng K, et al. Composition and properties of porous blend membranes containing tertiary amine based amphiphilic copolymers with different sequence structures [J]. J Colloid Interface Sci, 2015, 437:124-131.

[100] Odian G 2004. Principles of Polymerization [M]. Wiley,NewYork.

[101] Ting JM, Navale TS, Bates FS, et al. Precise Compositional Control and Systematic Preparation of Multimonomeric Statistical Copolymers [J]. ACS Macro Letters, 2013, 2 (9):770-774.

[102] Holmberg AL, Karavolias MG, Epps TH. RAFT polymerization and associated reactivity ratios of methacrylate-functionalized mixed bio-oil constituents [J]. Polymer Chemistry, 2015, 6 (31):5728-5739.

[103] Idowu LA, Hutchinson RA. Solvent Effects on Radical Copolymerization Kinetics of 2-Hydroxyethyl Methacrylate and Butyl Methacrylate [J]. Polymers (Basel), 2019, 11 (3).

[104] Fineman M, Ross SD. Linear method for determining monomer reactivity ratios in copolymerization [J]. Journal of Polymer Science, 1950, 5 (2):259-262.

[105] Kelen T, Tüdös F. Analysis of the Linear Methods for Determining Copolymerization Reactivity Ratios. I. A New Improved Linear Graphic Method [J]. Journal of Macromolecular Science. Chemistry, 1974, 9:1-27.

[106] O'Driscoll KF, Reilly PM. Determination of reactivity ratios in copolymerization [J]. 1987, 10-11 (1):355-374.

[107] Tidwell PW, Mortimer GA. An improved method of calculating copolymerization reactivity ratios [J]. Journal of Polymer Science, 1965, 3 (1):369-387.

[108] Mayo FR, Lewis FM. Copolymerization. I. A Basis for Comparing the Behavior of Monomers in Copolymerization; The Copolymerization of Styrene and Methyl Methacrylate [J]. Journal of the American Chemical Society, 1944, 66 (9):1594-1601.

[109] CANKAYA N, TEMÜZ MM. Monomer reactivity ratio of cellulose grafted with N-cyclohexylacrylamide and methyl methacrylate by atom transfer radical polymerization [J]. Cellulose Chemistry and Technology, 2012, 48:209-215.

[110] Jagan Mohan D. Synthesis, characterization and swelling properties of copolymers of N(-1,1-dimethyll-3-oxobutyl)acrylamide with methyl methacrylate [J]. Designed Monomers and Polymers, 2013, 17 (5):438-444.

[111] Abdollahi M, Sharifpour M. A new simple procedure to calculate monomer reactivity ratios by using on-line 1H NMR kinetic experiments Copolymerization system with greater difference between the monomer reactivity ratios [J]. Polymer, 2007, 48 (1).

[112] Pasquale AJ, Long TE. Determination of monomer reactivity ratios using in situ FTIR spectroscopy for maleic anhydride norbornene free radical copolymerization [J]. Journal of Applied Polymer Science, 2004, 92:3240–3246

[113] Wittenberg NFG, Buback M, Hutchinson RA. Kinetics and Modeling of Methacrylic Acid Radical Polymerization in Aqueous Solution [J]. Macromolecular Reaction Engineering, 2013, 7 (6):267-276.

[114] Zhao J-w, Zhu H, Wu Y-x, et al. In situ monitoring of coordination copolymerization of butadiene and isoprene via ATR-FTIR spectroscopy [J]. Chinese Journal of Polymer Science, 2010, 28 (3):385-393.

[115] Zhang W, Allgaier J, Zorn R, et al. Determination of the Compositional Profile for Tapered Copolymers of Ethylene Oxide and 1,2-Butylene Oxide by In-situ-NMR [J]. Macromolecules, 2013, 46 (10):3931-3938.

[116] Mahdavian A-R, Abdollahi M, Bijanzadeh HR. Kinetic study of radical polymerization. III. Solution polymerization of acrylamide by1H-NMR [J]. Journal of Applied Polymer Science, 2004, 93 (5):2007-2013.

[117] Preusser C, Hutchinson RA. An In-Situ NMR Study of Radical Copolymerization Kinetics of Acrylamide and Non-Ionized Acrylic Acid in Aqueous Solution [J]. Macromolecular Symposia, 2013, 333 (1):122-137.

[118] Abdollahi M, Mehdipour-Ataei S, Ziaee F. Using1H-NMR spectroscopy for the kinetic study of thein situ solution free-radical copolymerization of styrene and ethyl acrylate [J]. Journal of Applied Polymer Science, 2007, 105 (5):2588-2597.

[119] Debnath D, Baughman JA, Datta S, et al. Determination of the Radical Reactivity Ratios of 2-(N-Ethylperfluorooctanesulfonamido)ethyl Acrylate and Methacrylate in Copolymerizations with N,N-Dimethylacrylamide by in Situ 1H NMR Analysis As Established for Styrene–Methyl Methacrylate Copolymerizations [J]. Macromolecules, 2018, 51 (20):7951-7963.

[120] Feng J, Oyeneye OO, Xu WZ, et al. In-Situ NMR Measurement of Reactivity Ratios for Copolymerization of Methyl Methacrylate and Diallyl Dimethylammonium Chloride [J]. Industrial & Engineering Chemistry Research, 2018, 57 (46):15654-15662.

[121] Faraguna F, Vidović E, Jukić A. Reactivity ratios and copolymer properties of 2-(diisopropylamino)ethyl methacrylate with methyl methacrylate and styrene [J]. Polymer International, 2015, 64 (10):1497-1504.

[122] Palermo EF, McNeil AJ. Gradient Sequence π-Conjugated Copolymers [J]. 2014, 1170:287-299.

[123] Biryan F, Demirelli K. Copolymerization of benzyl methacrylate and a methacrylate bearing benzophenoxy and hydroxyl side groups: Monomer reactivity ratios, thermal studies and dielectric measurements [J]. Fibers and Polymers, 2017, 18 (9):1629-1637.

[124] Erol I, Sahin B. Functional styrenic copolymer based on 2-(dimethylamino)ethyl methacrylate: Reactivity ratios, biological activity thermal properties and semi-conducting properties [J]. Journal of Fluorine Chemistry, 2015, 178:154-164.

[125] Zhang Z, Zheng H, Huang F, et al. Template Polymerization of a Novel Cationic Polyacrylamide: Sequence Distribution, Characterization, and Flocculation Performance [J]. Industrial & Engineering Chemistry Research, 2016, 55 (37):9819-9828.

[126] Al-Alawi S, Saeed NA. Preparation and separation of complexes prepared by template polymerization. [J]. Macromolecules, 1990, 23:4474.

[127] Clapper JD, Sievens-Figueroa L, Guymon CA. Photopolymerization in Polymer Templating† [J]. Chemistry of Materials, 2008, 20 (3):768-781.

[128] Patton DL, Kirt A. Page, Xu C, et al. Measurement of Reactivity Ratios in Surface-Initiated Radical Copolymerization [J]. Macromolecules, 2007, 40:17.

[129] Wang Y, Zhang X, Li W, et al. Determination of Reactivity Ratios of Copolymerization of Acrylamide (AM) and Methacryloxyethyltrimethyl Ammonium

Chloride (DMC) with Ultraviolet Initiation, and Their Sequence Length Distribution [J]. Polymers & Polymer Composites, 2016, 24 (5).

Chapter 3

# 3 Synthesis of VO$_2$/Poly(MMA-co-dMEMUABr) Antimicrobial/Thermochromic Dual-functional Coating

## 3.1 Abstract

In order to address the need for window coatings that can control both temperature while being self-cleaning, this work examined a dual-functional antimicrobial/thermochromic coating. The goal was addressed by chemically polymerizing the antimicrobial agent, quaternary ammonium compound (QAC) N,N-dimethyl-N-{2-[(2-methylprop-2-enoyl)oxy]ethyl}undecane-1-aminium bromide (dMEMUABr) while using vanadium dioxide (VO$_2$) as the thermochromic agent. The antimicrobial agent dMEMUABr, having a long hydrocarbon tail and acrylic moiety for enhanced killing, was synthesized and characterized by 1D NMR and FTIR spectra. VO$_2$ nanoparticles were synthesized hydrothermally and characterized by physicochemical analysis including powder XRD, DSC and SEM. Polymer coatings were obtained by polymerizing dMEMUABr with methyl methacrylate (MMA) monomer using UV curing investigating the required UV curing time. Thermochromic performance of dual-functional VO$_2$/poly(MMA-co-dMEMUABr) coating gave a solar energy modulation $\Delta T_{sol}$ of 5.8 % and luminous transmittance $T_{lum}$ at 25 °C of 36.1 %. The antimicrobial testing of the dual-functional coating indicated that it could kill 90.3% representative bacteria Escherichia coli (E.coli) within 24 h at a low QAC concentration (3.8 wt % relative to MMA). The hydrophilic property of the coating surface was measured by contact angle analysis, showing that enhanced hydrophilicity helps to attract more bacteria and increase the antimicrobial efficiency. The zone of inhibition test proved the contact kill principle of the coating, without releasing toxic antimicrobial agents to the environment.

## 3.2 Introduction

The global energy crisis has led to great need for reducing the energy needs for heating and cooling our homes and buildings, while simultaneously lowering our carbon footprint. Thermochromic smart windows provide a passive method to block undesired heat loss/gain for energy savings.[1] Vanadium oxide (VO$_2$) has been studied for decades

for thermochromic smart windows, due to its unique metal-to-semiconductor transition (MIT).[2] $VO_2$ nanoparticles have multiple morphologies, such as tetragonal $VO_2$(A), monoclinic $VO_2$ (B), $VO_2$(D), monoclinic rutile type $VO_2$(M), tetragonal rutile type $VO_2$(R) and $VO_2$(P).[3, 2, 4] $VO_2$(M) is the most promising morphology exhibiting fully reversible first-order phase transition to block infrared light transmittance, depending on the temperature.[5] When its temperature reaches a critical temperature ~68 °C, $VO_2$ transforms from an IR transparent state (monoclinic phase) to an IR reflective state (rutile phase).[6] When used as a coating, it transforms automatically to block infrared light, without requiring any external switching device.[7, 8]

Another challenge with windows is that they are easily fouled by fungi, bacteria or other organisms due to the moisture from the rain and humidity. Commonly used antimicrobial agents include nanoparticles ($TiO_2$,[9-11] $ZnO_2$,[12, 13] etc.), silver ions,[14, 15] quaternary ammonium compounds (QACs),[16-18] halogens[19, 20] and other oxygen reactive species. Among the various antimicrobial agents, QACs are of interest due to their strong antibacterial performance in both light and dark conditions, low toxicity, low cost and environmental stability.[21, 22] Their antimicrobial property is considered as long-lasting and does not need to be activated by external light energy, compared to widely used $TiO_2$.[23] In previous times, many antibacterial products were based on the release principle, leaching bactericidal substances such as $Ag^+$ ions to the surroundings. These biocides are usually toxic or contain toxic heavy metal ions, which will eventually pollute the environment.17 However, QACs kill microorganisms upon contact without leaching bactericidal substances.

In this work, for the first time, a dual-functional antimicrobial/thermochromic coating was produced. For the antimicrobial purpose, the QAC N,N-dimethyl-N-{2-[(2-methylprop-2-enoyl)oxy]ethyl}undecane-1-aminium bromide (dMEMUABr) was co-polymerized with methyl methacrylate (MMA) via UV curing. The positively charged QACs are believed to attract negatively charged bacteria membrane surfaces through ionic interactions. Generally, the antimicrobial performance of QACs is related to the length of N-alkyl chain. N-alkyl chain with 8-18 carbons shows excellent antimicrobial property.[15] A long hydrophobic tail is believed to enhance activity by inserting into the

bacterial cell, leading to leakage of intercellular constituents, resulting in bacteria death.[24] On the other hand, thermochromic $VO_2$ nanoparticle was well-dispersed inside the poly(MMA-co-dMEMUABr) matrix, blocking undesired infrared light at the same time.

## 3.3 Experimental Section

### 3.3.1 Materials

Vanadium oxide ($V_2O_5$, ≥98 %), 2-(dimethylamino)ethyl methacrylate (DMAEMA, 98 %), 1-bromoundecane (98 %), photo initiator 2-hydroxy-2-methylpropiophenone (HMP, 97 %), methyl methacrylate (MMA, 99%), poly(methyl methacrylate) (PMMA, Mw 350,000) were purchased from Sigma-Aldrich, Canada. The solvents acetonitrile, hexanes and chloroform were purchased from Caledon Laboratory Ltd, Ontario, Canada. Acetone were obtained from Fisher Chemical, Canada. Inhibitor MEHQ was removed from MMA by distillation method.[25] In brief, MMA was washed twice with 5% sodium hydroxide (NaOH, ≥97%) and distilled water. After that, it was dried over $MgSO_4$ (≥ 97%) for 2 h. After degassing, MMA was then vacuum distilled with the middle portion collected for the polymerization studies. All other chemicals were used as received.

### 3.3.2 Synthesis of $VO_2$ nanoparticle

$VO_2$ nanoparticles were synthesized by a hydro/solvothermal method, in which both acetone and water were used to reduce $V_2O_5$.[26] In brief, the well-mixed suspension of 0.6 g of $V_2O_5$, 18 ml of acetone and 14 ml of deionized water were added to a 100 ml Teflon-lined autoclave at room temperature. The autoclave was hydrothermally treated at 210 °C for 18 h in the oven. After that, particles were washed twice with acetone by centrifugation and then dried at 50 °C overnight. The dried particles were then placed in a quartz tube and calcined in a tubular furnace at 550 °C for 3 h with continuous flow of nitrogen gas (temperature increased at a rate of 45 °C/min). $VO_2$ nanoparticles were then removed from the ambient furnace tube, when it was cooled to the room temperature to avoid oxidation.

### 3.3.3  Synthesis of dMEMUABr

The synthesis method of antimicrobial agent dMEMUABr was modified based on Zhao's method.[27] dMEMUABr was synthesized by reacting 0.314g of DMAEMA (2mmol) with 0.52g of 1-bromoundecane (2.2mmol) through a quaternization reaction (Figure 3.1). The amount of 1-bromoundecane was adjusted to be in slight excess to that of DMAEMA to enhance the purity of QAC, as 1-bromoundecane was easier to be dissolved in organic solvent (hexane) and removed by evaporation. It was desired to not have DMAEMA in the final product, as it has high boiling point. The starting materials were dissolved in 10 ml of acetonitrile. Nitrogen gas was purged to the uniform solution for the first 30 min to remove any dissolved oxygen with the mixture consistently stirred at 50 °C for 24 h. Then, a rotary evaporator was used to remove acetonitrile. When the solvent was evaporated, hexane was added to the viscous solution to wash the product to remove any unreacted 1-bromoundecane by centrifugation. As dMEMUABr did not dissolve in hexane, it remained in the bottom in the centrifugation with the supernatant of hexane then decanted.  The product was then dried in vacuum oven at 40 °C for 24 h to achieve the purified dMEMUABr, which was a white wax-like product. Yield: 78.7%. $^{1}$H NMR (CDCl$_3$, 400 MHz) δ (ppm): 0.89 (-CH$_2$-C$\underline{H}_3$, 3H), 1.26-1.35 (-N$^+$-CH$_2$-CH$_2$-(C$\underline{H}_2$)$_8$-CH$_3$, 16H), 1.76 (-N$^+$-CH$_2$-C$\underline{H}_2$-(CH$_2$)$_8$-CH$_3$, 2H), 1.96 (C$\underline{H}_3$-C(C=O)=C-, 3H), 3.53 ((C$\underline{H}_3$)$_2$-N$^+$-, 6H), 3.60 (-N$^+$-C$\underline{H}_2$-CH$_2$-(CH$_2$)$_8$-CH$_3$, 2H), 4.19 (-O-CH$_2$-C$\underline{H}_2$-N$^+$-, 2H), 4.66 (-O-C$\underline{H}_2$-CH$_2$-N$^+$-, 2H), 5.69 and 6.16 (C$\underline{H}_2$=C-COO-, 2H). $^{13}$C NMR (CDCl$_3$, 100 MHz) δ (ppm): 14.01 (-CH$_2$-$\underline{C}$H$_3$), 18.19 ($\underline{C}$H$_3$-C(C=O)=C-), 22.56 (-N$^+$-CH$_2$-$\underline{C}$H$_2$-CH$_2$-(CH$_2$)$_5$-CH$_2$-$\underline{C}$H$_2$-CH$_3$), 26.17 (-N$^+$-CH$_2$-CH$_2$-$\underline{C}$H$_2$-), 29.17-29.35 (-N$^+$-CH$_2$-CH$_2$-CH$_2$-($\underline{C}$H$_2$)$_5$-CH$_2$-CH$_2$-CH$_3$), 31.76 (-N$^+$-CH$_2$-CH$_2$-CH$_2$-(CH$_2$)$_5$-$\underline{C}$H$_2$-CH$_2$-CH$_3$), 51.78 (($\underline{C}$H$_3$)$_2$-N$^+$-), 58.06 (-O- $\underline{C}$H$_2$-CH$_2$-N$^+$-), 62.09 (-O-CH$_2$-$\underline{C}$H$_2$-N$^+$-), 65.36 (-N$^+$- $\underline{C}$H$_2$-(CH$_2$)$_9$-CH$_3$), 127.30 (CH$_3$-C(C=O)=$\underline{C}$-), 135.05 (CH$_3$-$\underline{C}$(C=O)=C-), 166.23 (CH$_3$-C($\underline{C}$=O)=C-).
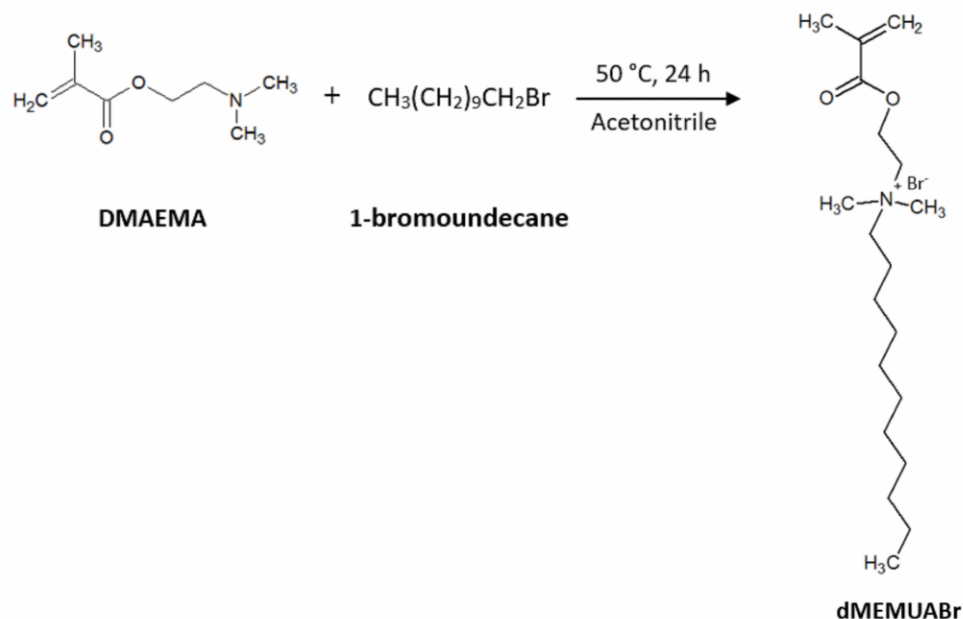
**Figure 3.1: Synthesis scheme for dMEMUABr.**

### 3.3.4 Preparation of VO₂/Poly(MMA-co-dMEMUABr) dual-functional coating by UV curing

0.038g of synthesized dMEMUABr was dissolved in 0.5 ml of chloroform. Then, 1.01g of MMA, 0.08 g of PMMA and 0.0328 g of photo initiator HMP were added in order. PMMA was used as a thickener to make the solution more viscous. Then, 10mg of $VO_2$ nanoparticles were added to the mixture and dispersed in the solution by sonication. A 2.5 cm x 2.5 cm glass slide was cleaned by sonication in alcohol for 20 min and then dried with air. 100 μl of above mixture was evenly spread on the glass slide and then cured by UV irradiation (UVP95012701, 365 nm, 100W, BLAK-RAY, B-100AP Model, U.S.A.) for defined times. The chemical structure of synthesized poly(MMA-co-dMEMUABr) was shown in Figure 3.2. The entire UV curing procedure was carried out under nitrogen gas (Figure 3.3). The coating was then dried in a vacuum oven to remove any remaining solvent. In synthesis of all coating samples, the intensity of UV light received by the coating is 8335 μW/cm2, tested by UVA/B light meter (SPER SCIENTIFIC, 850009). The distance from the UV light source to the coating surface is 4 cm.
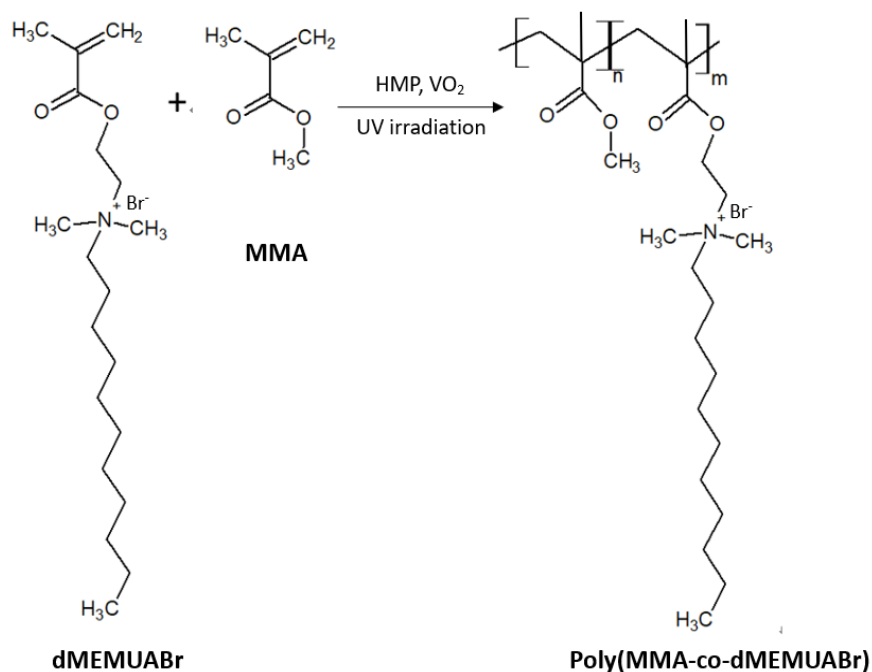
**Figure 3.2: Synthesis scheme for copolymerization of MMA and dMEMUABr via UV curing.**
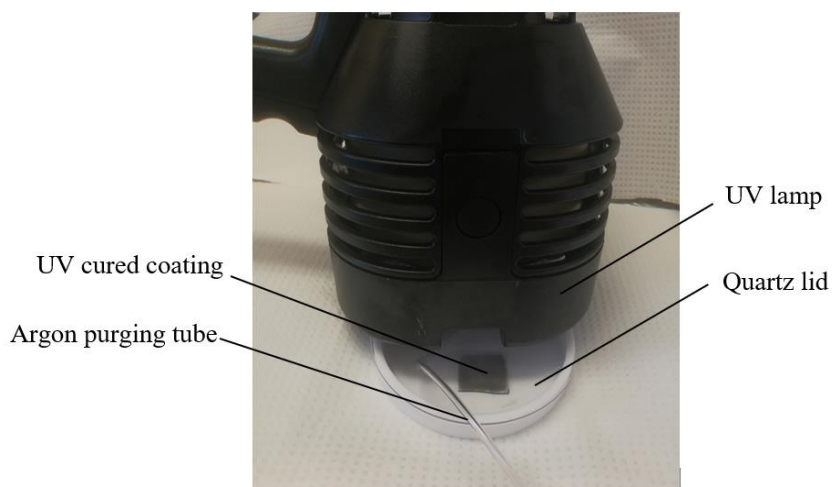


**Figure 3.3: Picture of UV curing process.**

## 3.3.5 Measurements

Functional groups of dMEMUABr were characterized by Fourier transform infrared (FTIR) Spectra using wavenumber 600–4000 cm$^{-1}$. 1D ($^{1}$H and $^{13}$C) nuclear magnetic

resonance spectroscopy (NMR) spectra using Bruker AVIII HD 400, were recorded for dMEMUABr characterization. Chloroform-d was used as solvent with the chemical shifts referenced to tetramethylsilane (TMS). The crystalline phase analysis of synthesized $VO_2$ was tested by X-ray diffraction (XRD; Bruker D2 phaser powder diffractometer, Billerica, MA, USA) using Cu Kα (λ=1.54184 Å) radiation between 20° to 80°. The phase transition property of $VO_2$ nanoparticles was characterized by Differential scanning calorimetry (DSC, SDT Q600, TA Instruments, US) using heating and cooling cycle between 10° to 140°. The morphologies and dimensions of $VO_2$ particle were tested by Scanning electron microscopy (SEM) and analyzed by ImageJ Software. Contact angle measurements of the dual-functional $VO_2$/poly(MMA-co-dMEMUABr) coating was carried out by a PGX measuring head pocket goniometer (FIBRO System AB, Sweden). The optical transmittance of the dual-functional coating was measured using a UV-3600 UV-vis-NIR spectrophotometer (Shimadzu, Kyoto, Japan), with temperature controlled by a Julabo F12-Refrigarated/Heating Circulator (Julabo GmbH, Seelbach, Germany).

## 3.3.6   Study of UV curing time complete copolymerization

Before adding dMEMUABr and $VO_2$ particles, the system of MMA, PMMA and HMP was studied. To ensure all MMA monomers completely polymerized before heating in the oven, samples with different UV curing times were removed by dissolution in chloroform-d for NMR testing.

## 3.3.7   Testing of antimicrobial ability

The antimicrobial ability of coating samples was tested against Escherichia coli (strain ATCC 29425). In a typical method, E. coli was cultured in a tryptic soy broth at 37 °C for 24 h. Bacteria were then washed with PBS buffer three times to remove broth by centrifugation at 3000 rpm for 15 min each time, and the supernatant was then decanted. The bacterial concentration was determined by OD600. The OD600 of the E.coli suspension was adjusted to be 0.2 using PBS buffer, which indicated the concentration was approximately $10^8$ CFU/ml.[28, 29] This value was used for estimation. The exact bacteria concentration can be calculated by the counted colony-forming units (CFU) on the agar plate. The suspension was then appropriately diluted to achieve $10^5$ CFU/ml.

Coating samples were immersed in 20 ml of above bacteria suspension inside the centrifuge tubes, shaking at 37 °C for 24 h in the dark. After that, a series of dilution was applied and aliquots (100 μl) of diluted bacteria solution with concentration of $10^3$ CFU/ml were evenly spread on the tryptic soy agar plates. Each sample was tested in triplicate. After 24 h incubation at 37 °C, the number of CFU on agar plate was counted and the bacteria reduction was calculated compared to control sample.

## 3.4 Results and Discussion

### 3.4.1   Characterization of synthesized VO$_2$ nanoparticle

The purity, morphology and first-order transition property of VO$_2$ nanoparticles synthesized by the hydro/solvothermal procedure were carefully characterized before being integrated into the dual-functional coating. XRD analysis of the nanoparticles is shown in Figure 3.4, indicating high purity of monoclinic phase VO$_2$ particles. No characteristic peak for V$_2$O$_5$ is present in the XRD graph, indicating that acetone successfully reduced V$_2$O$_5$ to the desired VO$_2$ product.

Figure 3.5 shows the enthalpy change of VO$_2$ particles measured by DSC. The observed endothermic peak in heating (insulator-to-metal) and exothermic peak in cooling (metal-to-insulator) are due to the release of latent heat, accompanied with the first order phase transition.[30] The synthesized VO$_2$ exhibits good MIT transition with temperature hysteresis of 12 °C. It has a lower transition temperature at 60 °C than the bulk VO$_2$ at 68 °C. The well-defined peaks indicate high crystalline quality.[31, 32]
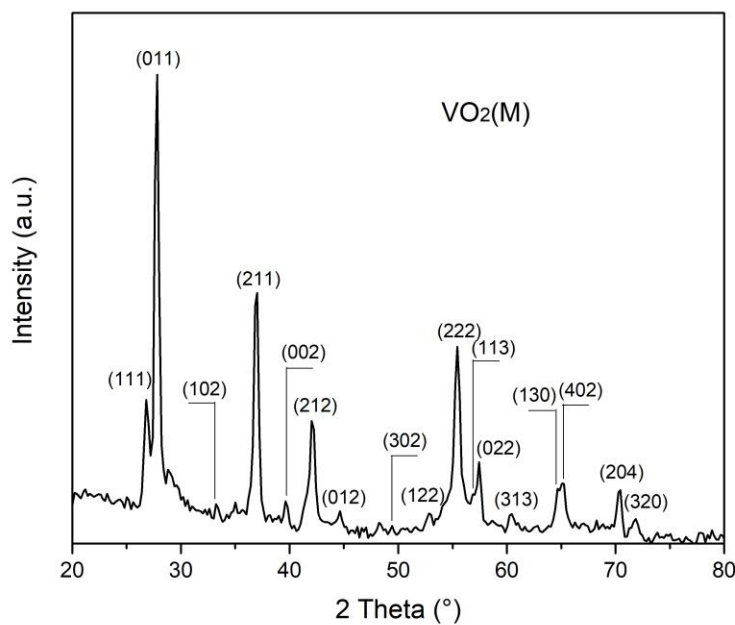
**Figure 3.4: XRD pattern of synthesized VO₂.**
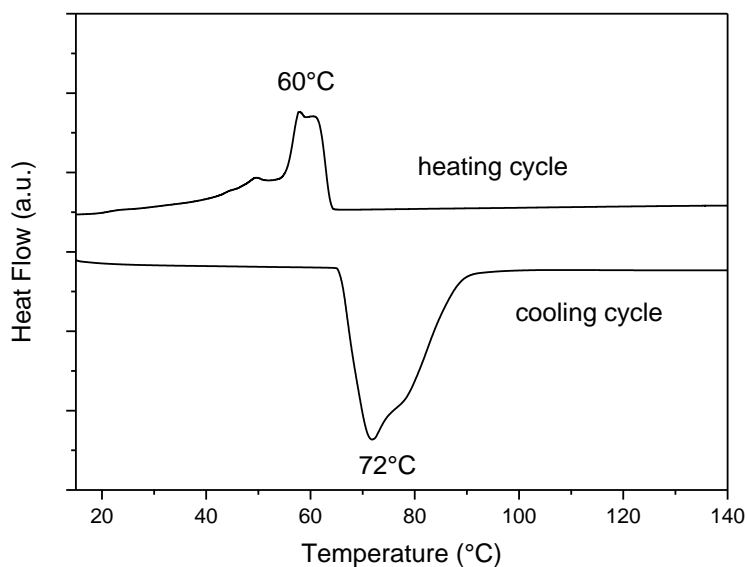


**Figure 3.5: DSC curves of synthesized VO₂.**

The SEM images for morphologies and dimensions of $VO_2$ are depicted in Figure 3.6, using 1.00 k and10.0 k resolution respectively. The electron micrographs indicate that the synthesized $VO_2$ has a fiber nanomorphology. The size distribution histogram was

determined using Image J software with SEM images, as shown in Figure 3.7. This figure shows that the synthesized $VO_2$ nanoparticles are $1.5 \pm 0.35$ μm in length and $148.6 \pm 64$ nm in width, which are similar to the previous report of $1.6 \pm 0.9$ μm in length and $180 \pm 70$ nm in width.[26] The size distribution was even, and no obvious large aggregates or particles were observed from the SEM results.
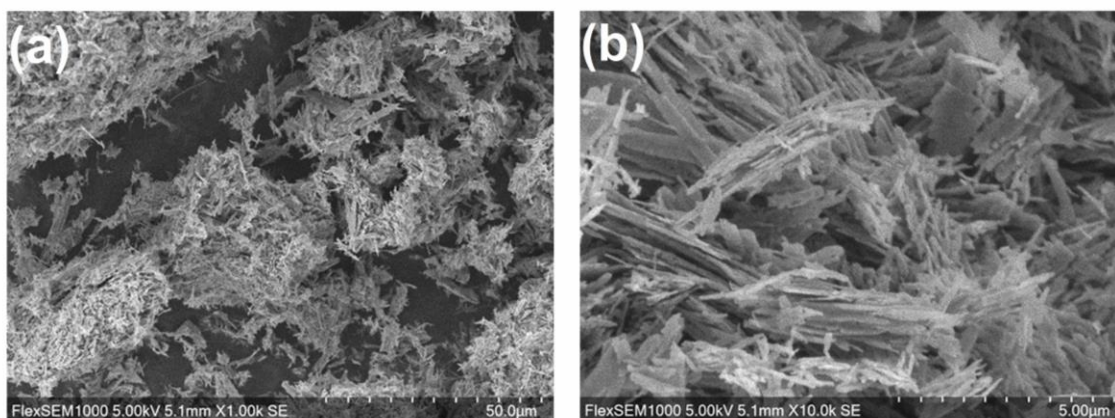


**Figure 3.6： SEM images of synthesized VO₂ using (a)1.00 k and (b)10.0 k resolution.**
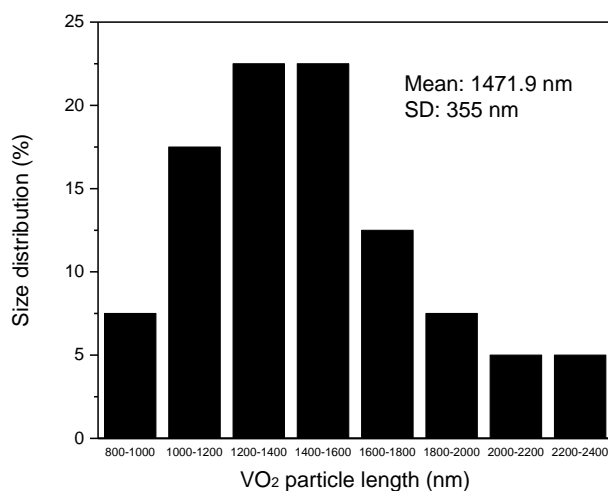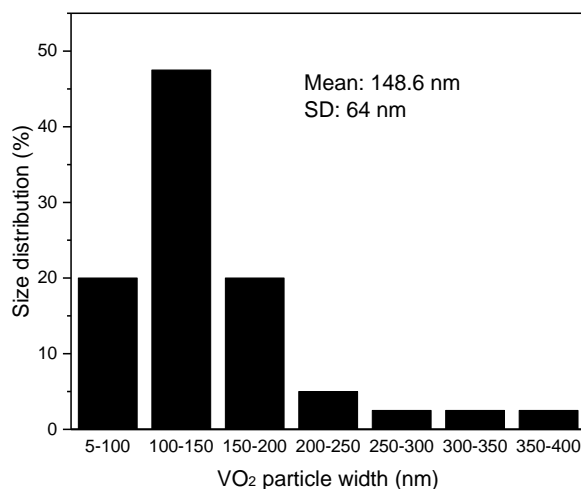
**Figure 3.7：Size distribution of synthesized VO₂ nanoparticles.**

## 3.4.2 Characterization of synthesized antimicrobial agent dMEMUABr

dMEMUABr was prepared by quaternization reaction of DMAEMA and 1-bromoundecane. The FTIR spectra of dMEMUABr and its reactants are shown in Figure 3.8. In the FTIR spectra of dMEMUABr, peaks at 2921 and 2853 $cm^{-1}$ come from asymmetric and symmetric vibration of $-(CH_2)_n-$ from 1-bromoundecane and DMAEMA. Peaks at 1722, 1640 and 1151 $cm^{-1}$ indicate the stretching vibration of C=O, C=C and C-O respectively. The FTIR result indicates the successful synthesis of dMEMUABr using DMAEMA and 1-bromoundecane.
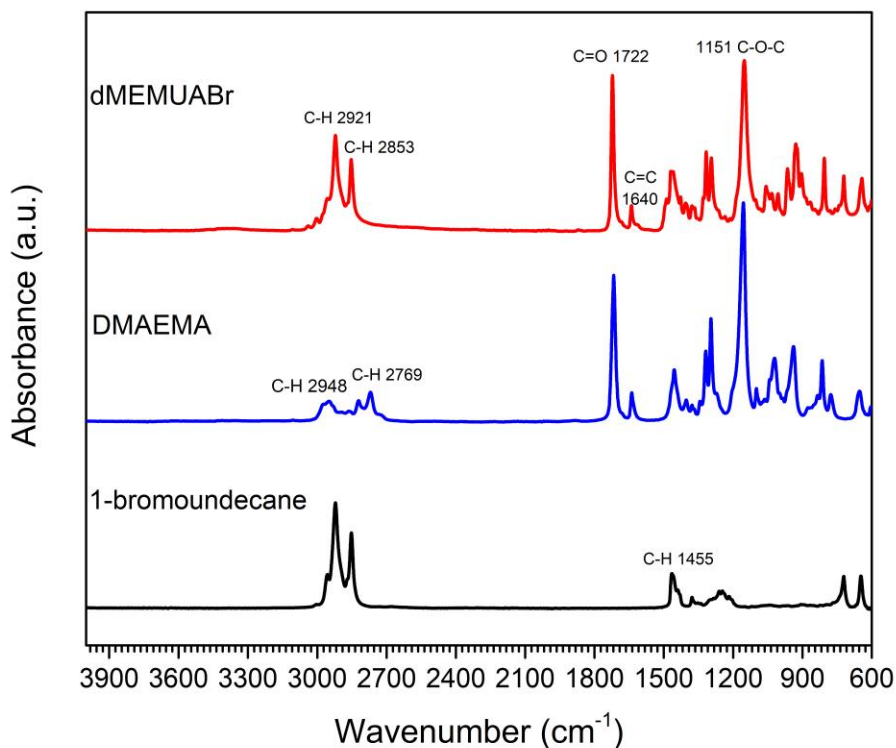
**Figure 3.8: The FTIR spectra of synthesized dMEMUABr**

The synthesized dMEMUABr was also characterized by ($^1$H and $^{13}$C) NMR, which is shown in Figure 3.9. In the $^1$H NMR spectrum, 8 different protons in the long alkane chain overlap with each other and form one peak located at 1.26 -1.35 ppm (peak No. 2). In the $^{13}$C NMR result, 5 different carbon atoms in the long alkane chain overlap at 29.17-29.35 ppm (peak No. 4). C2 and C6 also overlap at 22.56 ppm. No other solvent or reactants' characteristic peak can be observed in the NMR test, which confirms the purity of the synthesized dMEMUABr.
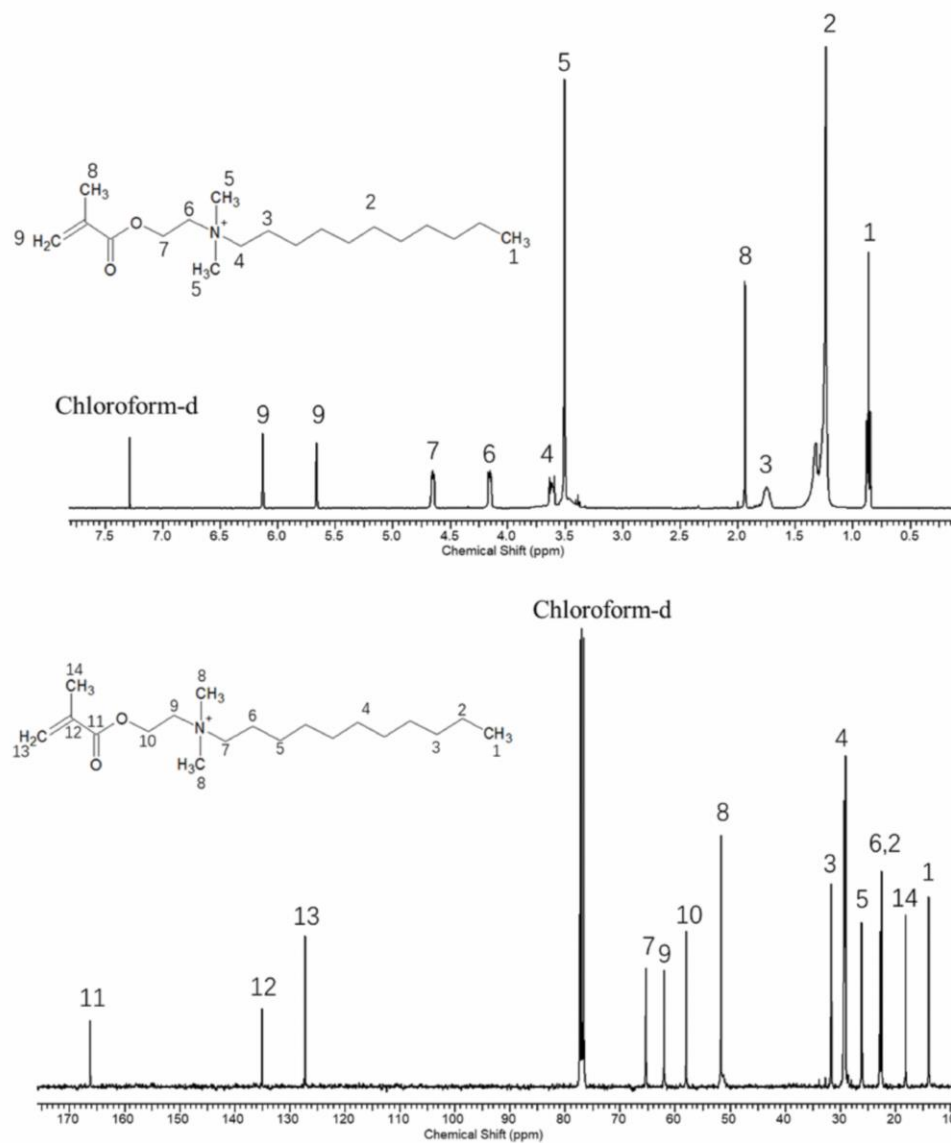
**Figure 3.9: (a) ¹H and (b) ¹³C NMR spectra of synthesized dMEMUABr (in CDCl₃).**

### 3.4.3 UV curing copolymerization process

MMA monomers were used to polymerize with the synthesized dMEMUABr monomers using a UV curing process with the presence of the UV photo initiator HMP. HMP absorbs UV light energy and produces free radicals, which initiates the chain polymerization. [33] Under UV curing, dMEMUABr polymerizes with MMA via C=C double bond consumption. The system of MMA, PMMA and HMP was first investigated to determine the UV curing time for complete polymerization, where PMMA (8 wt%

relative to MMA) was used as thickener. The $^1$H NMR spectra of the coating samples with different UV curing times are shown in Figure 3.10. When the coating was UV cured for 3 min, the characteristic peaks of MMA can be observed at 6.10, 5.56, 3.75 and 1.93 ppm, indicating the MMA monomers were not completely polymerized. The MMA peaks disappeared when the coating was UV cured for 4 min or longer. Therefore, all MMA monomers completely polymerized to be PMMA within 4 min. Longer UV curing time did not have obvious influence on the polymer composition.
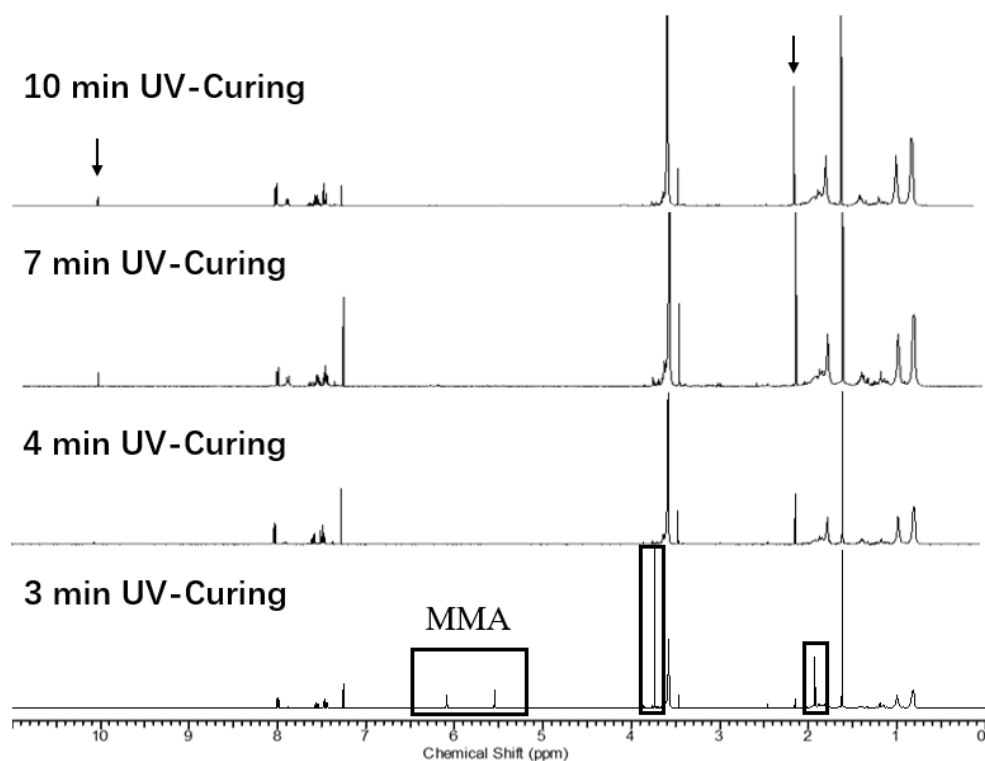


**Figure 3.10: $^1$H NMR spectrums of 3 min, 4 min, 7 min and 10 min UV cured PMMA coatings.**

In addition to the peaks representing PMMA, MMA and HMP, new peaks at 10.03 and 2.18 ppm are observed, assigned to benzaldehyde and acetone. These peaks are attributed to the decomposition of photo initiator HMP during the UV-curing process (Figure 3.11). To minimize the effect of decomposition products on the performance, vacuum heating treatment at 70 °C was applied and $^1$H NMR tests were conducted on coatings before and after the heating treatment. The peak at 3.60 ppm is assigned to protons of -OCH$_3$ in

PMMA. As in each coating sample, same amount of MMA polymerized to be PMMA and this peak represents 3H, integration area of this peak was set to be 3 in $^1$H NMR spectrum. Therefore, the mole ratio of the formed acetone and benzaldehyde relative to PMMA can be achieved respectively. Table 3.1 indicates that the amount of decomposition products acetone and benzaldehyde decreased after vacuum heating at 70 °C. The longer time the coating is UV cured, the easier decomposition products form. Half acetone and benzaldehyde evaporated in 7 min UV cured coating, as it contained a greater amount of decomposition products. The remaining amount of decomposition products were almost the same for 4 min and 7 min UV cured coating after vacuum heating treatment. The remaining residues were difficult to be removed, likely due to being trapped inside the polymer with benzaldehyde having a high boiling point. Therefore, the minimum UV curing time for complete polymerization was determined to be 4 min, which was applied for preparation of all coating samples.
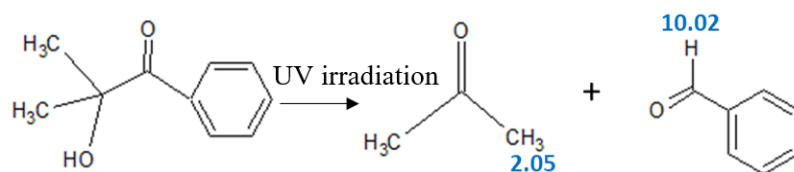


**Figure 3.11: Scheme for decomposition of photo initiator HMP.**

**Table 3.1**：**Integration of decomposition products acetone and benzaldehyde relative to PMMA before and after vacuum heating at 70 °C in $^1$H NMR spectrums。**

|  | PMMA<br>(3H, 3.60 ppm) | Acetone<br>(6H, 2.17 ppm) | Benzaldehyde<br>(1H, 10.03 ppm) |
|---|---|---|---|
| 4 min UV Curing | 3 | 0.08 | 0.01 |
| 4 min UV Curing with vacuum heating at 70 °C | 3 | 0.06 | 0 |
| 7 min UV Curing | 3 | 0.16 | 0.02 |
| 7 min UV Curing with vacuum heating at 70 °C | 3 | 0.07 | 0.01 |

### 3.4.4 Testing of VO$_2$/Poly(MMA-co-dMEMUABr) dual-functional coating

After adding the antimicrobial agent dMEMUABr and VO$_2$ nanoparticles to the above system, a dual-functional coating was quickly achieved via UV curing, which formed a transparent colorless thin film on the glass surface. MMA and dMEMUABr monomers are covalently bonded through acrylic moieties with long hydrocarbon tail oriented out towards to the surface. The positively charged dMEMUABr moieties attracts negatively charged bacteria membrane surfaces through strong ionic interactions, and the long hydrophobic tail performs antimicrobial property. VO$_2$ nanoparticle is integrated inside the polymer matrix, obtaining thermochromic performance to regulate the solar irradiation through its unique first-order MIT at the same time. The schematic pictorial of this system is shown in Figure 3.12.
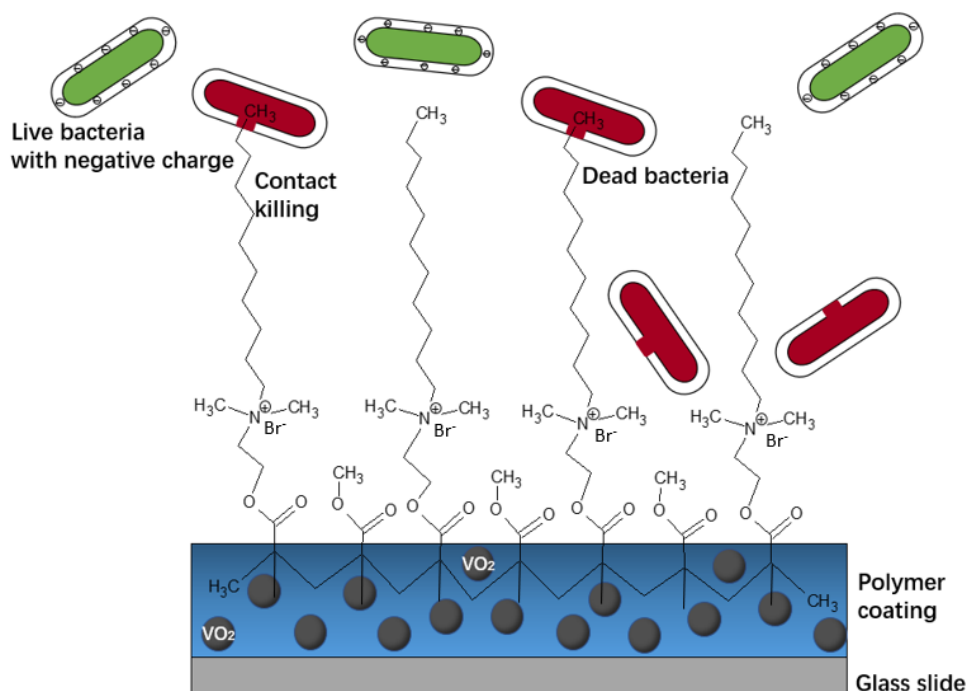
**Figure 3.12: Schematic of synthesized VO₂/poly(MMA-co-dMEMUABr) dual-functional coating.**

Water contact angle measurements were carried out on the UV cured PMMA, dMEMUABr based acrylic and the dual-functional coatings. The contact angle can tell the properties of a surface, Here, a 1.4 ml water drop was generated on top of the coating surface, with at least 6 different drops conducted, and the average used for analysis. As shown in Figure 3.13, the contact angle of UV cured PMMA coating is 71.7 °, which was identical with previous studies on water contact angle of pure PMMA material between 65 ° to 80 °.[34-36] A coating is considered as hydrophilic when its water angle is smaller than 90 °, otherwise it is considered as hydrophobic.[37, 38] After the polymerization of MMA and antimicrobial agent dMEMUABr, the contact angle decreased to 56.3 °, which indicated the surface became more hydrophilic. Although the long hydrophobic hydrocarbon chain should have increased the contact angle, the hydrophilic moiety of dMEMUABr takes a dominant role. After adding VO₂, the particle took place of some hydrophilic dMEMUABr and led to the increase of the contact angle to 63.2 °. The

hydrophilic property helps to attract more bacteria to be adhesive to the coating surface in the solution, so that the antibacterial efficiency can be greatly enhanced.
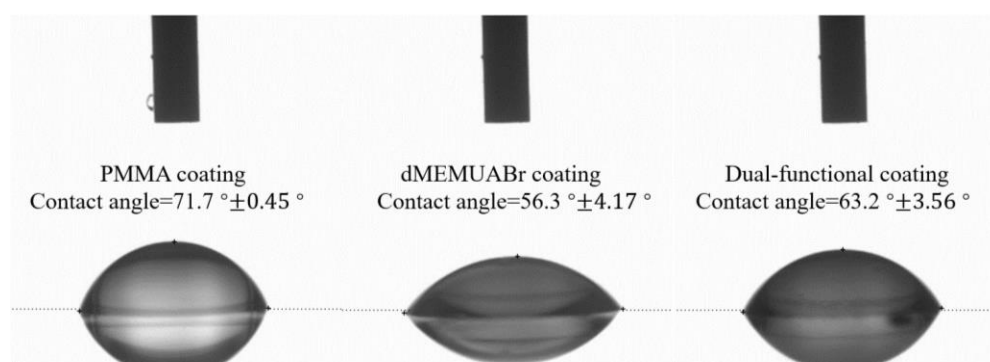


**Figure 3.13: The contact angles of UV cured (a) PMMA coating, (b) Poly(MMA-co-dMEMUABr) coating and (c) as-synthesized dual-functional VO₂/poly(MMA-co-dMEMUABr) coating.**

**The thermochromic property of the VO₂/poly(MMA-co-dMEMUABr) dual-functional coating** was tested by measuring the transmittance in near infrared region using room temperature (25 °C) and high temperature (90 °C), as shown in Figure 3.14. 1 wt% of VO₂ nanoparticles relative to the amount of MMA was integrated into the poly(MMA-co-dMEMUABr) matrix. The transmittance spectra of the dual-functional coating were conducted using glass as the reference. The integrated $VO_2$ (M) experienced complete MIT during the temperature increase. The solar energy modulation ($\Delta T_{sol}$) was calculated to be 5.8 %, using a wavelength range of 950 nm-2500 nm, which started from the cross point of two transmittance curves. High luminous transmittance value $T_{lum}$ (41.1 % at 90 °C and 36.1 % at 25 °C) was achieved. The ability of blocking infrared light through its first-order MIT increases with higher $VO_2$ concentration, but at the expense of lower luminous transmittance.

These thermochromic performance parameters were also compared with the performance of some other hydrothermally synthesized $VO_2$ film, summarized in Table 3.2. Beside acetone, oxalic acid ($H_2C_2O_4.2H_2O$) and hydrazine ($N_2H_4$) can also be used for reducing $V_2O_5$. $VO_2$ nanoparticles synthesized using $N_2H_4$ and ($H_2C_2O_4.2H_2O$) were found to exhibit similar $\Delta T_{sol}$ values (6.93 % and 6.4 %), but lower luminous transmittance values

(7.35 % and 31.2 %). Furthermore, hydrazine is considered as highly toxic material, which may cause health concern issues. Reducing $V_2O_5$ using $N_2H_4.HCl$ and HCl has reported excellent thermochromic performance with high $\Delta T_{sol}$ and $T_{lum}$ values. However. this method needs higher synthesis temperature and the synthesized $VO_2$ has a high transition temperature at 91 °C, which makes it more difficult to be used for window coating. Producing $VO_2$ (M) with acetone offers an easier, safer and more energy-efficient way compared to other synthesis methods.
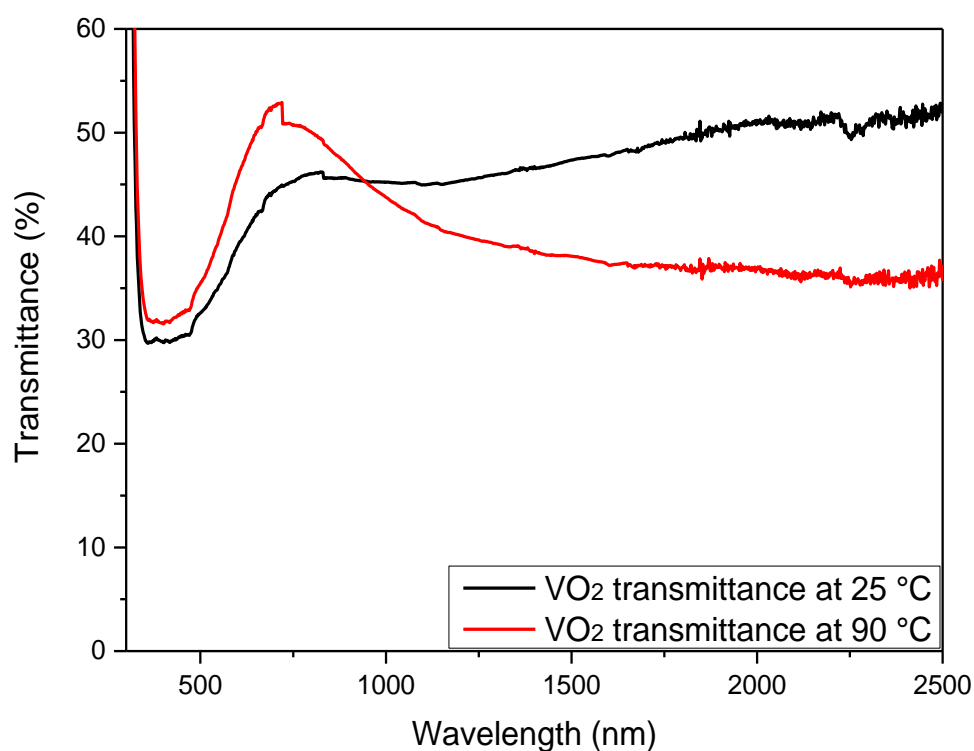


**Figure 3.14: Optical transmittance spectra of synthesized VO₂/poly(MMA-co-dMEMUABr) dual-functional coating.**

**Table 3.2: Comparison of hydrothermal synthesis methods of VO$_2$(M) in some published papers and related experimental parameters.**

| Precursors | T/t | $T_{lum}$ & $T_{sol}$ |
|---|---|---|
| V$_2$O$_5$+(CH$_3$)$_2$CO | 210/18 | $T_{lum}$(90 °C)=41.1%; $T_{lum}$(25 °C)=36.1% $\Delta T_{sol\,(950\text{-}2500)}$ =5.8 % |
| V$_2$O$_5$+H$_2$C$_2$O$_4$.2H$_2$O [39] | 260/48 | $T_{lum}$(90 °C)=8.21%; $T_{lum}$(25 °C)=7.35% $\Delta T_{sol\,(1000\text{-}2500)}$ =6.93 % |
| V$_2$O$_5$+ N$_2$H$_4$.HCl+HCl [40] | 330/15 | $T_{lum}$=45.6%; $\Delta T_{sol}$=22.3 % |
| V$_2$O$_5$+H$_2$O$_2$+H$_2$WO$_4$+N$_2$H$_4$ [41] | 260/24 | $T_{lum}$ =31.2%; $\Delta T_{sol}$=6.4 % |

**Antimicrobial activity of the dual-functional coating** was carried out using E.coli bacteria. As the final bacteria suspension spread on agar plates for incubation experienced series 10 fold dilution, the concentration of E.coli suspension contacting with coatings for 24 h can be calculated by multiplying the counted CFU number with ten to the power of the dilution times. The antimicrobial efficiency was calculated using the reduction of the living E.coli bacteria between each coating and control sample versus the control number of bacteria. The control sample was a glass specimen without any coating. The purchased PMMA coating was prepared by directly dissolving purchased PMMA (Mw 350,000) powder in dichloromethane and spread onto a glass surface. The coating was heated in a vacuum oven at 55 °C to evaporate the solvent.

It was found that no obvious antimicrobial performance was shown for purchased PMMA (Mw 350,000) coating compared to control sample, while the UV cured PMMA coating showed a relatively low antimicrobial efficiency of 25.7 %. It may be due to the free radicals generated by HMP and its decomposition products. Synthesized poly(MMA-co-dMEMUABr) coating showed excellent antibacterial efficiency, which can kill almost all

(99.8 %) E.coli bacteria within 24 h contact at low addition (3.8 wt% relative to MMA). The antimicrobial mechanism of dMEMUABr is that the acrylic end of dMEMUABr is linked to MMA via double bond and the long hydrophobic tail faces outward. Positively charged dMEMUABr attracts bacteria through ionic interaction. It interacts with a target site at the inner membrane of the bacteria and bind to DNA, which was found that it can cause compaction and collapse of DNA.[42] McDonnell proposed the procedures of QACs killing the microorganisms: (1) Adsorption and penetration of QACs to the bacteria cell wall, (2) react with the lipid or protein of the cytoplasmic membrane, (3) lead to membrane disorganization and leakage of low-weight material, (4) degradation of nucleic acid, (5) lysis of cell wall due to autolytic enzymes.[43-45, 42] In addition, the antimicrobial moieties are believed to be enriched at the coating surface due to low surface energy, which greatly increases the antimicrobial efficiency.[27] In comparison, the $VO_2$/PMMA coating exhibited a low antimicrobial effect on E.coli. This result is in accord with previous antimicrobial testing of a nano-$VO_2$ film which did not show any significant antimicrobial effect on gram-negative bacteria, such as E. coli and P. aeruginosa.[46] In our approach, the dual-functional $VO_2$/poly(MMA-co-dMEMUABr) coating has a relatively good antimicrobial activity, which can kill 90.3 % E.coli within 24 h. The antimicrobial efficiency decreased by 9.5 % after $VO_2$ nanoparticle addition. This may be due to $VO_2$ particles occupying an active area of main antimicrobial agent dMEMUABr contacting bacteria.

**Table 3.3: Viable bacterial concentration and antimicrobial efficiency with initial bacterial concentration of $10^5$ CFU/ml treated with different coatings for 24 h.**

|  | Living E.coli Concentration (CFU/ml) | Antimicrobial efficiency |
|---|---|---|
| Control (glass) | $1.14 \times 10^5$ |  |
| Purchased PMMA (Mw 350,000) | $1.07 \times 10^5$ | 6.1 % |
| PMMA (UV cured) | $8.47 \times 10^4$ | 25.7 % |
| VO$_2$/PMMA (UV cured) | $9.63 \times 10^4$ | 15.5 % |
| Poly(MMA-co-dMEMUABr) (UV cured) | $2.67 \times 10^2$ | 99.8 % |
| VO$_2$/Poly(MMA-co-dMEMUABr) (UV cured) | $1.11 \times 10^4$ | 90.3 % |

Zone of inhibition was carried out using E.coli bacteria solution at concentration of $10^5$ CFU/ml spread all over the agar plate. Poly(MMA-co-dMEMUABr) coating and VO$_2$/poly(MMA-co-dMEMUABr) dual-functional coating were attached to the bacteria directly and incubated in the nutrient agar at 37 °C for 24 h. As leaching of antimicrobial agent may eventually pollute the environment and raise bacteria's resistance, contact kill is highly desired. The test in Figure 3.15 shows the inhibition zone does not further expand around the coating. This means that the antimicrobial agent dMEMUABr only kills bacteria contacted to its surface and the toxic moieties does not release to the surroundings, even after addition of VO$_2$ nanoparticle. The result further proves the dual-functional coating kill bacteria based on non-release principle and neither dMEMUABr nor VO$_2$ will release to the environment.
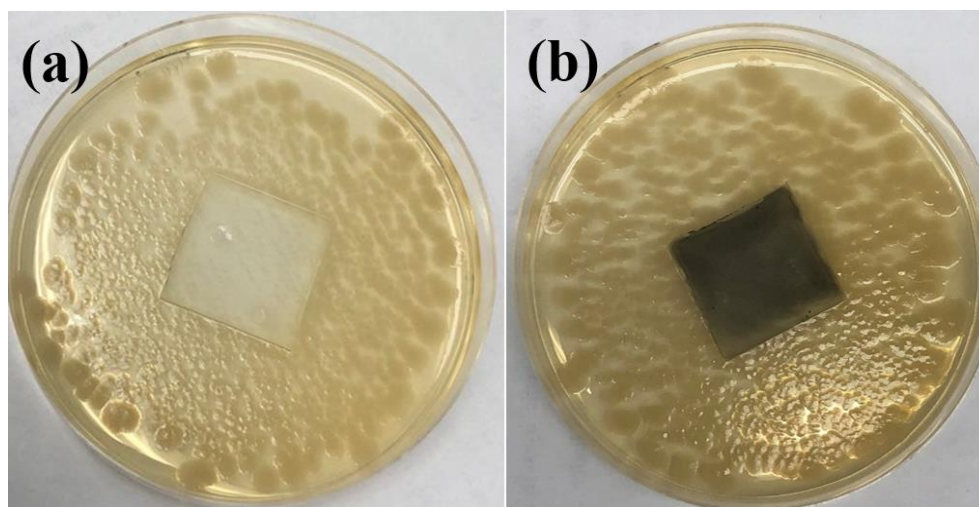
**Figure 3.15: Picture of zone of inhibition test result for (a) Poly(MMA-co-dMEMUABr) coating and (b) VO₂/poly(MMA-co-dMEMUABr) dual-functional coating..**

## 3.5 Conclusions

In this contribution, we successfully synthesized a dual-functional VO$_2$/poly(MMA-co-dMEMUABr) coating via UV curing, performing both thermochromic and antimicrobial property. The antimicrobial agent QAC dMEMUABr and thermochromic VO$_2$ (M) nanoparticles were well characterized. The dual-functional coating utilized the acrylic linked poly(MMA-co-dMEMUABr) and dispersed VO$_2$ inside the polymer. The UV curing time for complete polymerization was determined to be at least 4 min with the presence of HMP. All coating samples were vacuum heated at 70 °C to remove decomposition products of HMP after UV curing. The water angle test indicated the hydrophilic property of the coating surface. After VO$_2$ addition, the hydrophilicity decreased compared to poly(MMA-co-dMEMUABr) coating. The thermochromic test of the dual-functional coating proved the ability of blocking the infrared light when temperature raised to 90 °C. $\Delta T_{sol}$ (5.8 %) and $T_{lum}$ (36.1 %) values were achieved for optical performance of the thermochromic property. On the other hand, the antimicrobial test showed that the dual-functional coating had significant antibacterial activity against E. coli, with low dMEMUABr amount (3.8 wt% relative to MMA). The coating was tested based on contact kill principle, without leaching toxic substance to environment.

This work offers an inspiration of dual-functional coating production for window, screen, medical imaging usage or other further applications.

## 3.6 References

[1] Alie D, Gedvilas L, Wang Z, et al. Direct synthesis of thermochromic VO2 through hydrothermal reaction [J]. Journal of Solid State Chemistry, 2014, 212:237-241.

[2] Li M, Magdassi S, Gao Y, et al. Hydrothermal Synthesis of VO2 Polymorphs: Advantages, Challenges and Prospects for the Application of Energy Efficient Smart Windows [J]. Small, 2017, 13 (36).

[3] Leroux C, Nihoul G, Van Tendeloo G. From VO2(B) to VO2(R) Theoretical structures of VO2 polymorphs and in situ electron microscopy. [J]. Phys. Rev. B: Condens. Matter Mater. Phys., 1998, 57:5111-5121.

[4] Zhang J, Tian H, Hao L, et al. Thermochromic VO2 films from ammonium citrato-oxovanadate(iv) with excellent optical and phase transition properties [J]. Journal of Materials Chemistry C, 2016, 4 (23):5281-5288.

[5] Liang S, Shi Q, Zhu H, et al. One-Step Hydrothermal Synthesis of W-Doped VO2 (M) Nanorods with a Tunable Phase-Transition Temperature for Infrared Smart Windows [J]. ACS Omega, 2016, 1 (6):1139-1148.

[6] Dong B, Shen N, Cao C, et al. Phase and morphology evolution of VO2 nanoparticles using a novel hydrothermal system for thermochromic applications: the growth mechanism and effect of ammonium (NH4+) [J]. RSC Advances, 2016, 6 (85):81559-81568.

[7] Gao Y, Luo H, Zhang Z, et al. Nanoceramic VO2 thermochromic smart glass: A review on progress in solution processing [J]. Nano Energy, 2012, 1 (2):221-246.

[8] Wu C, Dai J, Zhang X, et al. Direct confined-space combustion forming monoclinic vanadium dioxides [J]. Angew Chem Int Ed Engl, 2010, 49 (1):134-137.

[9] Al-Jawad SMH, Taha AA, Salim MM. Synthesis and characterization of pure and Fe doped TiO2 thin films for antimicrobial activity [J]. Optik, 2017, 142:42-53.

[10] Cho M, Chung H, Choi W, et al. Different inactivation behaviors of MS-2 phage and Escherichia coli in TiO2 photocatalytic disinfection [J]. Appl Environ Microbiol, 2005, 71 (1):270-275.

[11] Yuan P, Ding X, Yang YY, et al. Metal Nanoparticles for Diagnosis and Therapy of Bacterial Infection [J]. Adv Healthc Mater, 2018, 7 (13):e1701392.

[12] Liu Y, He L, Mustapha A, et al. Antibacterial activities of zinc oxide nanoparticles against Escherichia coli O157:H7 [J]. J Appl Microbiol, 2009, 107 (4):1193-1201.

[13] Singh VP, Sandeep K, Kushwaha HS, et al. Photocatalytic, hydrophobic and antimicrobial characteristics of ZnO nano needle embedded cement composites [J]. Construction and Building Materials, 2018, 158:285-294.

[14] Duran N, Duran M, de Jesus MB, et al. Silver nanoparticles: A new view on mechanistic aspects on antimicrobial activity [J]. Nanomedicine, 2016, 12 (3):789-799.

[15] Jain A, Duvvuri LS, Farah S, et al. Antimicrobial polymers [J]. Adv Healthc Mater, 2014, 3 (12):1969-1985.

[16] Elena P, Miri K. Formation of contact active antimicrobial surfaces by covalent grafting of quaternary ammonium compounds [J]. Colloids Surf B Biointerfaces, 2018, 169:195-205.

[17] Klibanov AM. Permanently microbicidal materials coatings [J]. Journal of Materials Chemistry, 2007, 17 (24):2479.

[18] Melo LD, Palombo RR, Petri DF, et al. Structure-activity relationship for quaternary ammonium compounds hybridized with poly(methyl methacrylate) [J]. ACS Appl Mater Interfaces, 2011, 3 (6):1933-1939.

[19] Cherdtrakulkiat R, Boonpangrak S, Sinthupoom N, et al. Derivatives (halogen, nitro and amino) of 8-hydroxyquinoline with highly potent antimicrobial and antioxidant activities [J]. Biochem Biophys Rep, 2016, 6:135-141.

[20] Denyera SP, Stewartb GSAB. Mechanisms of action of disinfectants [J]. International Biodeterioration & Biodegradation, 1998, 41:261-268.

[21] Jampala SN, Sarmadi M, Somers EB, et al. Plasma-enhanced synthesis of bactericidal quaternary ammonium thin layers on stainless steel and cellulose surfaces [J]. Langmuir, 2008, 24 (16):8583-8591.

[22] Roy D, Knapp JS, Guthrie JT, et al. Antibacterial cellulose fiber via RAFT surface graft polymerization [J]. Biomacromolecules, 2008, 9 (1):91-99.

[23] Wanag A, Rokicka P, Kusiak-Nejman E, et al. Antibacterial properties of TiO2 modified with reduced graphene oxide [J]. Ecotoxicol Environ Saf, 2018, 147:788-793.

[24] Zhang S, Li R, Huang D, et al. Antibacterial modification of PET with quaternary ammonium salt and silver particles via electron-beam irradiation [J]. Mater Sci Eng C Mater Biol Appl, 2018, 85:123-129.

[25] Feng J, Oyeneye OO, Xu WZ, et al. In-Situ NMR Measurement of Reactivity Ratios for Copolymerization of Methyl Methacrylate and Diallyl Dimethylammonium Chloride [J]. Industrial & Engineering Chemistry Research, 2018, 57 (46):15654-15662.

[26] Alivio TEG, Sellers DG, Asayesh-Ardakani H, et al. Postsynthetic Route for Modifying the Metal—Insulator Transition of VO2 by Interstitial Dopant Incorporation [J]. Chemistry of Materials, 2017, 29 (12):5401-5412.

[27] Zhao J, Millians W, Tang S, et al. Self-Stratified Antimicrobial Acrylic Coatings via One-Step UV Curing [J]. ACS Appl Mater Interfaces, 2015, 7 (33):18467-18472.

[28] Gangan MS, Athale CA. Threshold effect of growth rate on population variability of Escherichia coli cell lengths [J]. R Soc Open Sci, 2017, 4 (2):160417.

[29] Sezonov G, Joseleau-Petit D, D'Ari R. Escherichia coli physiology in Luria-Bertani broth [J]. J Bacteriol, 2007, 189 (23):8746-8749.

[30] Kim Y, Yu S, Park J, et al. High-throughput roll-to-roll fabrication of flexible thermochromic coatings for smart windows with VO2 nanoparticles [J]. Journal of Materials Chemistry C, 2018, 6 (13):3451-3458.

[31] Horrocks GA, Singh S, Likely MF, et al. Scalable hydrothermal synthesis of free-standing VO(2) nanowires in the M1 phase [J]. ACS Appl Mater Interfaces, 2014, 6 (18):15726-15732.

[32] Whittaker L, Zhang H, Banerjee S. VO2 nanosheets exhibiting a well-defined metal–insulator phase transition [J]. Journal of Materials Chemistry, 2009, 19 (19):2968.

[33] Monroe BM, Weed GC. Photoinitiators for Free-Radical-Initiated Photoimaging System [J]. Chem. Rev., 1993, 93 (1):435-448.

[34] Coan T, Barroso GS, Machado RAF, et al. A novel organic-inorganic PMMA/polysilazane hybrid polymer for corrosion protection [J]. Progress in Organic Coatings, 2015, 89:220-230.

[35] Ma Y, Cao X, Feng X, et al. Fabrication of super-hydrophobic film from PMMA with intrinsic water contact angle below 90° [J]. Polymer, 2007, 48 (26):7455-7460.

[36] Tennico YH, Koesdjojo MT, Kondo S, et al. Surface modification-assisted bonding of polymer-based microfluidic devices [J]. Sensors and Actuators B: Chemical, 2010, 143 (2):799-804.

[37] Jung YC, Bhushan B. Contact angle, adhesion and friction properties of micro-and nanopatterned polymers for superhydrophobicity [J]. Nanotechnology, 2006, 17 (19):4970-4980.

[38] Rios PF, Dodiuk H, Kenig S, et al. The effect of polymer surface on the wetting and adhesion of liquid systems [J]. Journal of Adhesion Science and Technology, 2007, 21 (3-4):227-241.

[39] Li Y, Ji S, Gao Y, et al. Core-shell VO2@TiO2 nanorods that combine thermochromic and photocatalytic properties for application as energy-saving smart coatings [J]. Sci Rep, 2013, 3:1370.

[40] Chen Z, Gao Y, Kang L, et al. Fine crystalline VO2 nanoparticles: synthesis, abnormal phase transition temperatures and excellent optical properties of a derived VO2 nanocomposite foil [J]. Journal of Materials Chemistry A, 2014, 2 (8):2718.

[41] Wang N, Duchamp M, Xue C, et al. Single-Crystalline W-Doped VO2Nanobeams with Highly Reversible Electrical and Plasmonic Responses Near Room Temperature [J]. Advanced Materials Interfaces, 2016, 3 (15):1600164.

[42] Zinchenko AA, Sergeyev VG, Yamabe K, et al. DNA compaction by divalent cations: structural specificity revealed by the potentiality of designed quaternary diammonium salts [J]. Chembiochem, 2004, 5 (3):360-368.

[43] GE M. Antisepsis, disinfection, and sterilization [J]. ASM Press, Washington, DC., 2007.

[44] Ioannou CJ, Hanlon GW, Denyer SP. Action of disinfectant quaternary ammonium compounds against Staphylococcus aureus [J]. Antimicrob Agents Chemother, 2007, 51 (1):296-306.

[45] Xu WZ, Yang L, Charpentier PA. Preparation of Antibacterial Softwood via Chemical Attachment of Quaternary Ammonium Compounds Using Supercritical CO2 [J]. ACS Sustainable Chemistry & Engineering, 2016, 4 (3):1551-1561.

[46] Li J, Zhou H, Wang J, et al. Oxidative stress-mediated selective antimicrobial ability of nano-VO2 against Gram-positive bacteria for environmental and biomedical applications [J]. Nanoscale, 2016, 8 (23):11907-11923.

Chapter 4

# 4 Reactivity Ratio of Methyl Methacrylate and N,N-dimethyl-N-{2-[(2-methylprop-2-enoyl)oxy]ethyl}undecane-1-aminium bromide (dMEMUABr) in thermal and UV initiated polymerization

## 4.1 Abstract

Reactivity ratios for methyl methacrylate (MMA) and the quaternary ammonium compound (QAC) N,N-dimethyl-N-{2-[(2-methylprop-2-enoyl)oxy]ethyl}undecane-1-aminium bromide (dMEMUABr) were determined for both thermal initiated and UV initiated copolymerization by using thermal initiatorazobisisobutyronitrile (AIBN) and photo initiator N,N-dimethylformamide (DMF) respectively. An in-situ NMR technique was utilized for analyzing the reactivity ratios in thermal initiated copolymerization at 60 °C with two different solvents, deuterated dimethyl sulfoxide (DMSO-$d_6$) and chloroform-d. The mole fraction of MMA ranged from 0.25 to 0.72 in DMSO-$d_6$ solvent and 0.25 to 0.9 in chloroform-d solvent. On the other hand, the conventional low-conversion technique was used for analyzing the reactivity ratios in UV initiated copolymerization, with MMA feed compositions ranging from 0.46-0.83 prepared. The consumption reduction of monomers and composition of the formed copolymer were monitored and calculated through ^{1}H NMR spectra. The in-situ NMR technique was found to simplify the process, saving experimental time by not requiring isolation of copolymer. For thermal initiated copolymerization, the results show the significant effect of solvent polarity on reactivity ratios. The reactivity ratio of MMA is higher than that of dMEMUABr in polar solvent DMSO-$d_6$, while the results are opposite in non-polar solvent chloroform-d. The reactivity ratios were found comparable for both thermal and UV initiated copolymerization, with the reactivity ratio of MMA lower than that of dMEMUABr in both cases using chloroform-d solvent. This study offers important information for designing and developing poly (MMA-co-dMEMUABr) by choosing a desired feed composition and solvent for specific application

## 4.2 Introduction

radical copolymerization is a widely used technology for preparing copolymers with synergistic properties using various monomers. The monomer sequence of the chain and compositional heterogeneity greatly influence the ultimate chemical and physical properties of the copolymer.[1, 2] Reactivity ratios provide critical information to predict and design the sequence distribution of the copolymer.[3] They also help to understand the kinetics and mechanistic perspective of copolymerization.[4] The calculation methods for reactivity ratios are categorized into non-linear least squares (NLLS) method and linear least squares (LLS) method. Common LLS methods include: Finemann-Ross(F-R), inverted Finemann-Ross (IFR), Yezrielev-Brokhina-Roskin (Y-B-R), Kelen-Tüdös (K-T) and the extended Kelen-Tüdös (EKT) method. In 1987, O'Driscoll and Reilly pointed out the limitations of the LLS method.[5] It was found that the LLS equations distort the error distribution and result in a poor estimate.[6, 7] The Mayo-Lewis equation of NLLS method was shown to be more ac curate and statistically sound, which shows the relationship between the composition of the feed and the copolymer.(eq 1)[8, 9] $F_1$ represents the mole fraction of monomer 1 in the copolymer, and $f_1$ represents the mole fraction of monomer 1 in the feed before copolymerization. $r_1$ and $r_2$ are the reactivity ratios of each monomer. When r is calculated higher than 1, this monomer shows a tendency polymerizing with its own monomer. When r is less than 1, this monomer is easier to polymerize with the other monomer.[10]

$$F_1 = \frac{r_1 f_1{}^2 + f_1(1-f_1)}{r_1 f_1{}^2 + 2f_1(1-f_1) + r_2(1-f_1)^2} \quad (1)$$

Quaternary ammonium compounds (QACs) are of significant interest nowadays for their excellent antimicrobial performance, low toxicity, low cost and environmental stability.[11, 12] A kind of QAC named N,N-dimethyl-N-{2-[(2-methylprop-2-enoyl)oxy]ethyl}undecane-1-aminium bromide (dMEMUABr) was successfully synthesized with an acrylic moiety on one end and a long hydrocarbon tail on the other, fully described in chapter 3.[13] On the other hand, methyl methacrylate (MMA) is a widely used material with excellent optical properties, light weight and resistance to

discoloration.[14] MMA has been reported for copolymerizing with a variety of monomers, including N(-1,1-dimethyl-3—oxobutyl)acrylamide (DOBA), diallyl dimethylammonium chloride (DADMAC) and 2-(diisopropylamino)ethyl methacrylate (DPA). Reactivity ratios of MMA and DOBA were reported to be 1.52 and 0.43 respectively in thermal copolymerization, showing that the MMA monomer is more reactive for polymerization on the copolymer end compared to the DOBA monomer.[15] In the copolymerization system of MMA and DPA, the reactivity ratio was 0.86-1.04 for MMA and 0.91-1.07 for DPA, showing ideal copolymerization behavior.[16] For an ideal copolymerization, the copolymer composition will be equal to the feed ratio. A relatively high reactivity ratio for MMA was reported for copolymerization with DADMAC with $r_{MMA}$=20.49-41.38 and $r_{DADMAC}$=0.09-0.33.[17] These widely varying values show that the reactivity ratios are sensitive to the other monomer MMA is copolymerized with. Investigation of the copolymerization of dMEMUABr and MMA copolymerization is important for developing antimicrobial coatings or processable antimicrobial plastics, with an investigation of the reactivity ratios helping one to better understand its sequence distribution and optimize the copolymer composition.

The reactivity ratios of MMA and dMEMUABr under thermal initiated and UV initiated copolymerization were examined in this work. Although a few investigations on the reactivity ratios in UV initiated copolymerization have been reported, the comparisons of these two types of initiation methods are not widely reported.[18, 19] Additionally, the effect of solvent on the reactivity ratios of MMA/dMEMUABr system was also investigated in this study. DMSO-$d_6$ and chloroform-d solvent were used and compared under thermal initiated copolymerization. An *in-situ* NMR technique and conventional low-conversion approach were applied respectively for determining the reactivity ratios in thermal and UV initiated copolymerization. *In-situ* NMR can simultaneously monitor the real-time concentration of each monomer, so the composition of the formed copolymer can be calculated.[20, 21] Using the conventional low-conversion method, monomers with different feed ratios are prepared, and the composition of the copolymers are then determined by the consumption of each monomers generated in $^1$H NMR spectra, with total mole conversion limited less than 15 %.[22, 23, 10] Both LLS and NLLS methods were compared for the reactivity ratio calculations.

## 4.3  Experimental Section

### 4.3.1  Materials

Methyl methacrylate (MMA, 99%), photo initiator 2-hydroxy-2-methylpropiophenone (HMP, 97 %), deuterated dimethyl sulfoxide (DMSO-$d_6$, 99.9 atom % D) were purchased from Sigma-Aldrich Canada. Thermal imitator azobisisobutyronitrile (AIBN) was purchased from Toronto Research Chemical Inc.  N,N-dimethylformamide (DMF) was obtained from Caledon Laboratory Ltd. Chloroform-d was obtained from Cambridge Isotope Laboratories Inc. The inhibitor (MEHQ, 4-methoxyphenol) of MMA was removed by distillation method.[17] All other chemicals were used as received.

### 4.3.2  Copolymerization process

**Thermal initiated copolymerization**

The method for the *in-situ* NMR measurement of reactivity ratios for thermal initiated copolymerization was based on our group's previous work.[17] The copolymerization of MMA and dMEMUABr was carried out at 60 °C. DMF was used as internal reference for monitoring concentration changes for each component, because of its high boiling point, stability in high temperature and not reacting with other solvent or monomers. Two different solvents (DMSO-$d_6$ and chloroform-d) were used for dissolution of all monomer. In brief, the predetermined amounts of dMEMUABr, MMA, AIBN, DMF and solvent DMSO-$d_6$/chloroform-d were added to the NMR tube (Table 4.1). The weights of monomers were also determined by $^1$H NMR based on the amount of internal reference DMF. After that, the solution was well sonicated to ensure complete dissolution, followed by purged with argon gas for 10 min to remove dissolved oxygen before sealed. The sealed NMR tube was put in NMR spectrometer with temperature set at 60 °C. The NMR instrument was programmed to collect $^1$H NMR spectra every 10 min for specified period. The formed copolymer was also dissolved in solvent, as no sediment was observed in the mixture after thermal copolymerization (Figure 6.1). Two series of experiments with different initial molar ratios were carried out using DMSO-$d_6$ solvent, so that the collected experimental data will cover a wider range of $f_1$-$F_1$ plot, giving more

accurate estimated reactivity ratios. Extending the copolymerization reaction time also enhanced data accuracy.

**Table 4.1: Reaction condition of in-situ thermal initiated copolymerization of MMA and dMEMUABr at 60 °C.**

| solvent | molar ratio MMA/dMEMUABr | MMA (mg) | dMEMUABr (mg) | AIBN (mg) | DMF (mg) | Time (h) |
|---|---|---|---|---|---|---|
| DMSO-$d_6$ | 0.73/0.27 | 22.88 | 33.26 | 1.20 | 12.28 | 10 |
| DMSO-$d_6$ | 0.57/0.43 | 14.62 | 41.49 | 1.14 | 15.70 | 10 |
| Chloroform-d | 0.25/0.75 | 2.80 | 32.65 | 1.46 | 10.85 | 13 |

**UV initiated copolymerization**

For investigation of UV initiated copolymerization, chloroform-d was used as solvent for comparison and the copolymerization process was carried out at room temperature. Different feed compositions of MMA and dMEMUABr (0.46/0.54, 0.51/0.49, 0.58/0.42, 0.77/0.23, 0.83/0.17) were prepared and determined by ^{1}H NMR. The total mass of MMA and dMEMUABr was controlled at 41.7 ± 1.1mg for all parallel experiments. The mixture was well sonicated in NMR tubes, then purged with argon gas for 10 min before sealing. The NMR tube was then illuminated by UV light (UVP95012701, 365 nm, 100W, BLAK-RAY, B-100AP Model, U.S.A.) for copolymerization. The distance between NMR tube and UV light source was 13 cm and the intensity of UV light received by the mixture was 5471 µW/cm$^2$, tested by UVA/B light meter (SPER SCIENTIFIC, 850009). The conversion rate was controlled lower than 15 % by adjusting the UV illumination time.

### 4.3.3  Characterizations

The thermal initiated copolymerization process was detected *in situ* by a Varian INOVA 600 spectrometer at 60 °C. According to the constant mole amount of internal reference DMF, the continuous change of each monomers can be monitored. The $^1$H NMR spectra of monomers mixture before and after UV initiated copolymerization were collected by Varian INOVA 600 spectrometer at room temperature. All chemical shifts were referenced to tetramethylsilane (TMS; 0.0 ppm). ACD Spectrus Processor was used for analyzing the $^1$H NMR spectra.

## 4.4 Results and Discussion

### 4.4.1  Copolymerization and copolymers

When exposed to heat or UV light, free radicals produced by thermal initiator AIBN or photo initiator HMP initiate the copolymerization process of MMA and dMEMUABr. There is one polymerizable C=C double bond for each monomer, which is consumed during polymerization and forms a long hydrocarbon backbone of poly(MMA-co-dMEMUABr), as shown in Figure 4.1 .
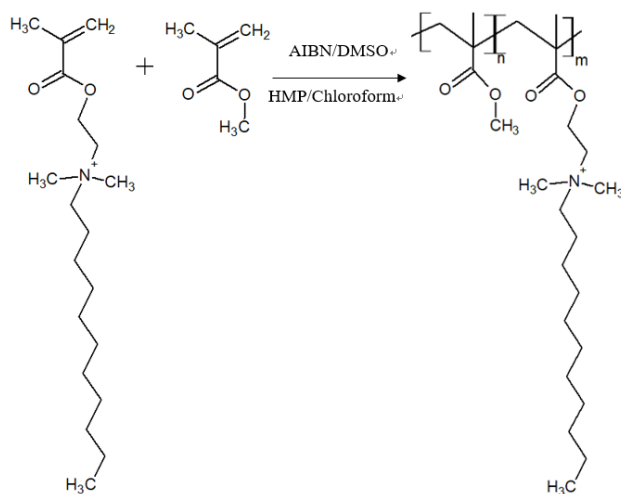


**Figure 4.1: Schematic Diagram of Copolymerization of MMA and dMEMUABr.**

## 4.4.2 In-situ NMR technique for reactivity ratio determination in thermal-initiated copolymerization

*In-situ* ^{1}H NMR analysis for determining reactivity ratios in heterogeneous copolymerization has been proved to be a reliable and more efficient and simpler method compared to traditional techniques, which providing accurate information of residue monomers' composition for a wide range of copolymerization reaction.[24, 17, 25] To monitor the consumption of each monomer and the initiator during the copolymerization process, internal reference DMF was added to the system. The characteristic peaks of DMF in ^{1}H NMR spectra are located at 2.74, 2.89 and 7.96 ppm, which do not overlap with other characteristic peaks. In addition, DMF is inert, which neither reacts with other chemicals nor decomposes during heating. The ^{1}H NMR spectra of the copolymerization mixture before and after 10 h thermal initiated copolymerization in DMSO-$d_6$ solvent were summarized in Figure 4.2. The characteristic peaks of MMA include 1.89, 3.69, 5.65 and 6.01 ppm. The characteristic peaks of dMEMUABr are located at 0.86, 1.26, 1.92, 3.12, 3.74, 4.54, 5.74 and 6.08 ppm. The peak at 1.67 ppm is assigned to AIBN.

To determine the molar number change of monomers over the reaction time, characteristic peaks of MMA at 5.65 and 6.01 ppm and characteristic peaks of dMEMUABr at 5.74 and 6.08 ppm were integrated by referencing to the integration of DMF characteristic peak. These peaks represent protons in =$CH_2$ group in MMA and dMEMUABr respectively, which are easily defined and do not overlap with other peaks. It was found that the integration values of MMA peaks at 5.65 and 6.01 ppm and dMEMUABr peaks at 5.74 and 6.08 ppm decreased with reaction time, while characteristic peaks at 0.81, 1.75, 3.57 ppm increased, due to the formation of copolymer. The peaks at 0.81, 1.75 ppm are assigned to the protons in the formed long hydrocarbon polymer backbone, and the peak at 3.57 ppm is the proton in functional group -$OCH_3$ in polymerized MMA. As the molar ratio of each monomer relative to DMF can be collected from ^{1}H NMR spectra and the mole number of added DMF is known, the mole number of MMA and dMEMUABr at any time during the entire copolymerization process can be calculated.
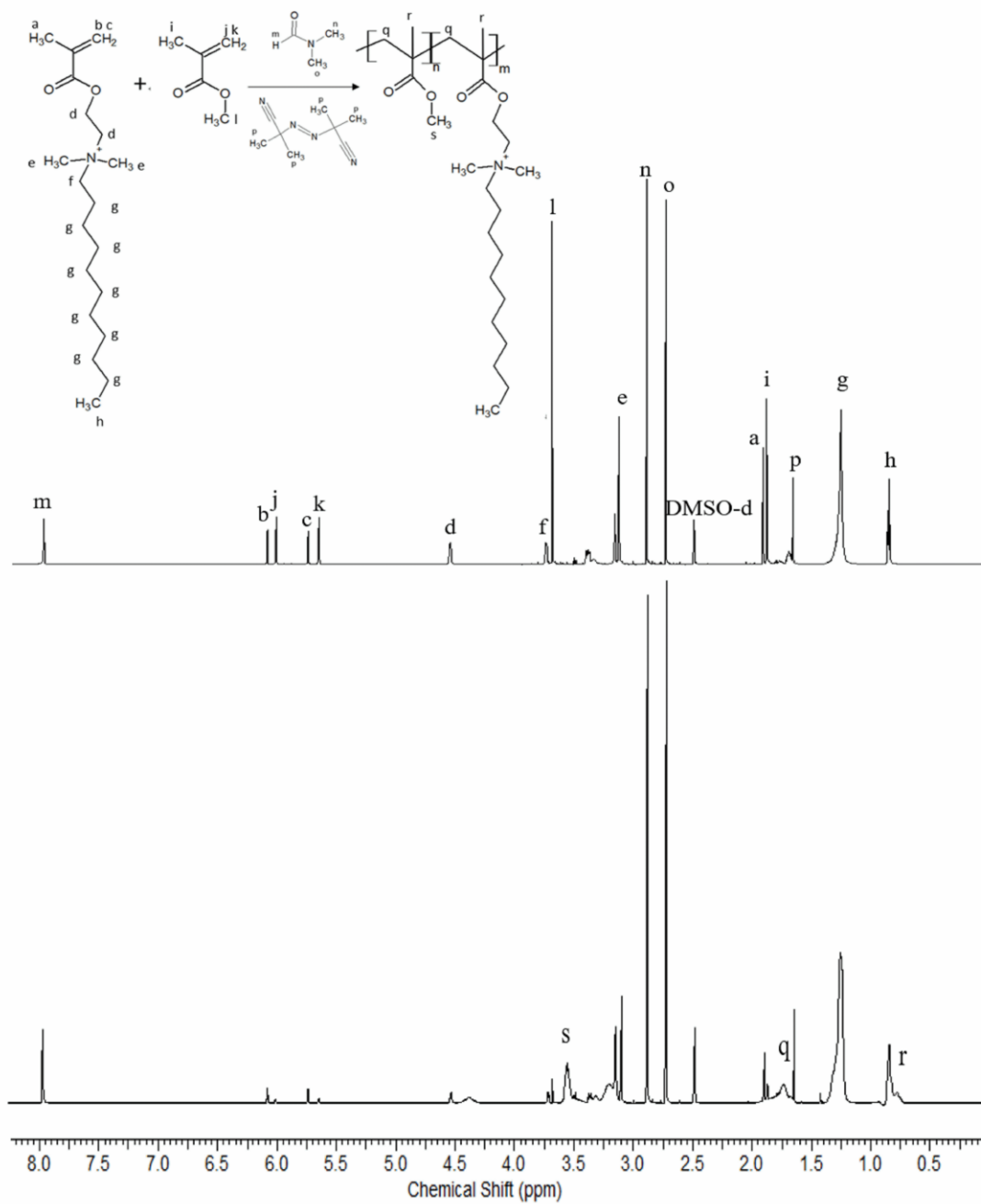
**Figure 4.2:** *In-situ* **1H NMR spectra of the reaction at 60 °C in DMSO-d$_6$ before and after 600 min copolymerization.**

After the mole number of MMA and dMEMUABr were collected over the entire copolymerization process, the consumption of each monomer over the reaction time in DMSO-d$_6$ and chloroform-d solvent was plotted in Figure 4.3 respectively. This shows that the concentration for both MMA and dMEMUABr continuously decrease with time. The concentration of MMA decreases faster than dMEMUABr in DMSO-d$_6$ solvent, while the concentration of dMEMUABr decreased faster in chloroform-d solvent. The consumption of both monomers was rapid for the first few hours, then gradually became slow. The experimental data was well fit with the simulated curve, generated by MATLAB software (MathWorks, Natick, MA, USA). Using the fitted curve, the mole fraction of MMA in the feed (f$_1$) and total monomers conversion (x$_n$) at any time can be generated, which was plotted in Figure 4.4. The calculated data provide a good fit with the simulated curve.
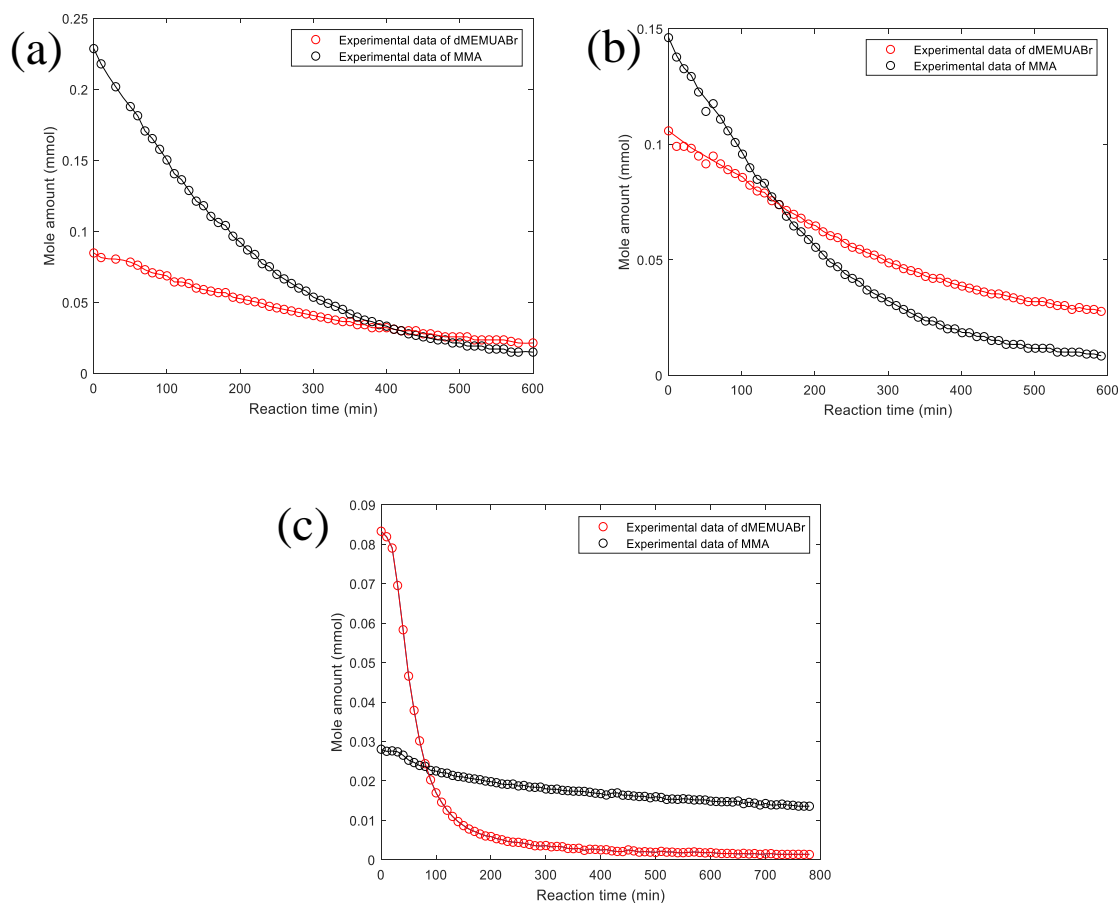
**Figure 4.3: Consumption of MMA (black) and dMEMUABr (red) monomer with reaction time at 60 °C thermal copolymerization in DMSO-d$_6$ solvent with initial molar ratio (a)MMA:dMEMUABr=0.73:0.27, (b) MMA:dMEMUABr=0.57:0.43 and (c) in chloroform-d solvent with initial molar ratio MMA:dMEMUABr=0.25:0.75.**
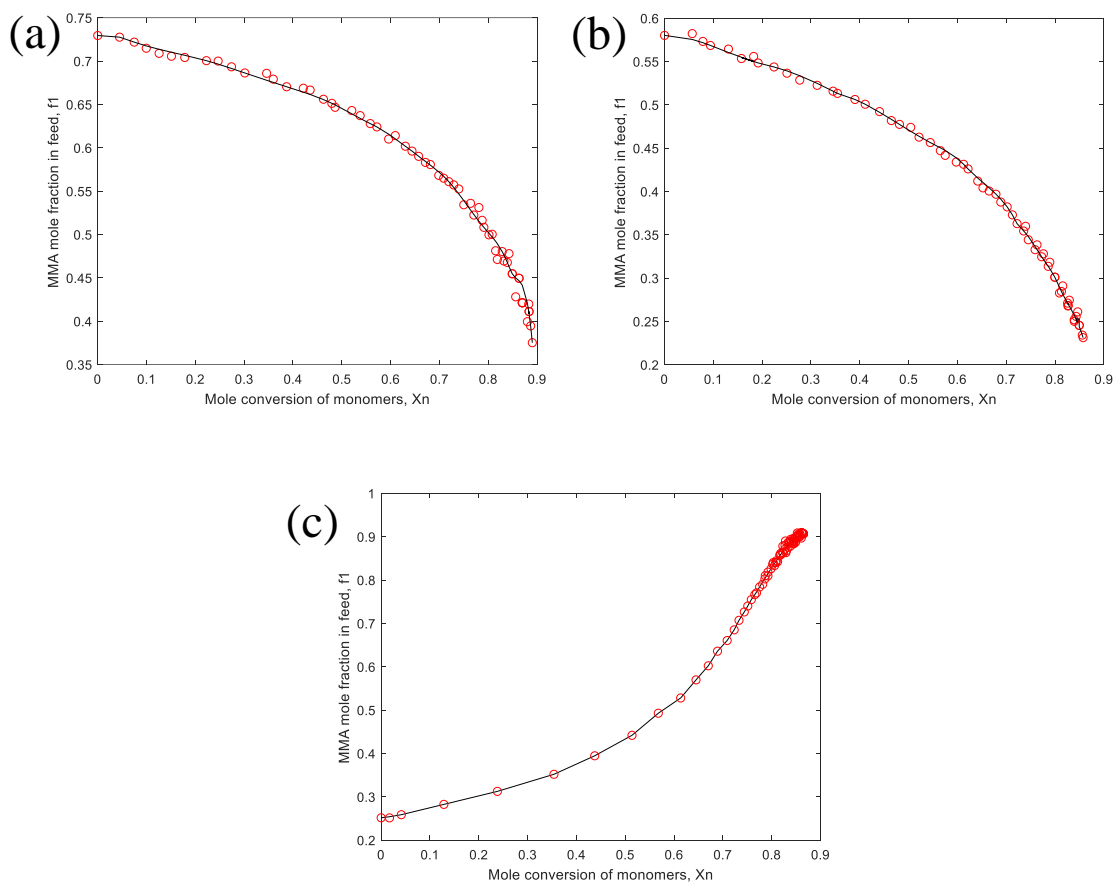
**Figure 4.4: Plot of the change of MMA mole fraction in feed f1 with the mole conversion of monomers Xn at 60 °C thermal copolymerization in DMSO-d$_6$ solvent with initial molar ratio (a) MMA:dMEMUABr=0.73:0.27, (b) MMA:dMEMUABr=0.57:0.43, and (b) in chloroform-d solvent with initial molar ratio MMA:dMEMUABr=0.25:0.75.**

Mole fraction of MMA and dMEMUABr in the formed copolymer $F_1$, $F_2$ can be calculated by either the direct numerical differential method (DND) or numerical solution differential method (NSD). For the DND method, the mole fraction of MMA in copolymer $F_1$ is considered as the mole number of MMA consumed in the feed versus the reduction of total mole number of monomers in a defined short time frame (eq 2). In the NSD method, $F_1$ is calculated using the mole fraction of MMA in feed $f_1$ and the mole conversion of monomers $x_n$ (eq 3 and eq 4). Similarly, the derivative is calculated as the difference of the mole fraction versus the difference of mole conversion within 40 min

reaction. The data of MMA mole fraction in copolymer $F_1$ calculated by these two methods is plotted and compared in Figure 4.5. The two series of $f_1$ and $F_1$ data with initial feed ratio 0.73/0.27 and 0.57/0.43 were combined, as they used the same experimental conditions. After achieving both $F_1$ and $f_1$ experimental data, the reactivity ratios for MMA and dMEMUABr were calculated using both the NLLS and linear KT methods. For the NLLS method, typically, the reactivity ratios $r_1$ and $r_2$ were solved to best fit the $F_1$ and $f_1$ data using equation 1 by MATLAB. Some experimental data points were deleted at high conversions. Therefore, the distribution of these points at both high and low conversion region are even, and each point received equal priority for fitting the Mayo-Lewis equation.

For DND method:

$$F_{1,t} = \frac{d_{m1,t}}{d_{m1,t} + d_{m2,t}} = \frac{m_{1,t+20} - m_{1,t-20}}{(m_{1,t+20} - m_{1,t-20}) + (m_{2,t+20} - m_{2,t-20})} \quad (2)$$

For NSD method：

$$F_{1,t} = f_{1,t} - (1 - X_{n,t}) \frac{df_1}{dX_n} \quad (3)$$

$$F_{1,t} = f_{1,t} - (1 - X_{n,t}) \frac{f_{1,t+20} - f_{1,t-20}}{X_{n,t+20} - X_{n,t-20}} \quad (4)$$
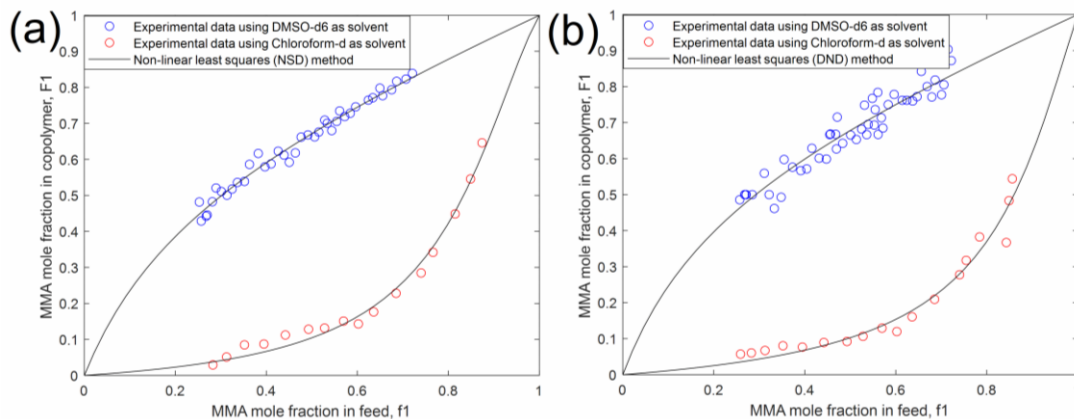
**Figure 4.5: Fitting curve using (a) NSD data and (b) DND data in DMSO-$d_6$ (blue) and chloroform-d (red) solvent.**

The calculated reactivity ratios of MMA and dMEMUABr in DMSO-$d_6$ and chloroform-d solvent estimated by non-linear NSD and DND method and linear KT method are summarized in Table 4.3. It can be seen that both the NLLS and linear KT methods gave generally similar results. The reactivity ratio of MMA is higher than that of dMEMUABr in DMSO-$d_6$ solvent, while the results show the opposite in chloroform-d solvent. For example, $r_{MMA}$=1.69 $r_{dMEMUABr}$=0.32 was achieved for DMSO-$d_6$ solvent, while $r_{MMA}$=0.46, $r_{dMEMUABr}$=11.51 was calculated for chloroform-d solvent, both estimated by the NSD method. The difference is attributed to the solvent polarity as well as the solvent-monomer interactions. The non-polar solvent chloroform-d (dielectric constant $\varepsilon$ = 4.8) and polar solvent DMSO-$d_6$ ($\varepsilon$ = 46.7) have different influence on solvation of monomers and radicals, which eventually affect the reactivity ratios and copolymer composition.[26, 27] For example, Idowu et al. studied the reactivity ratios of HEMA and BMA under different solvents and obtained $r_{HEMA}$=1.18, $r_{BMA}$=1.11 in the polar solvent dimethylformamide and $r_{HEMA}$=57.6, $r_{BMA}$=5.41 in the non-polar solvent xylene.[28] Our results indicate that chloroform-d may be a better choice for antimicrobial coating application, as the antimicrobial agent dMEMUABr is easier to be inserted into the copolymer chain compared to MMA monomer. The generated $F_1$-$f_1$ curve in the plot (Figure 4.5) using calculated reactivity ratio values by NLLS and KT method well fit the experimental data, which confirmed the results.

### 4.4.3 Low-conversion technique for reactivity ratio determination in UV initiated copolymerization

In UV initiated copolymerization, the photo initiator HMP was used to produce free radicals to initiate the copolymerization. To ensure the stability of internal reference DMF under UV light irradiation, a mixture of DMF and ethanol was checked with $^1$H NMR before and after 20 min UV exposure (Figure 6.2). The molar ratio remained constant, which indicated the inert property of DMF under 20 min UV exposure. MMA and dMEMUABr monomers were prepared in different molar ratios and the copolymerization was started by UV light irradiation. The total conversion of monomer was controlled below 15 % by shortening the UV exposure time. The mixture was examined by $^1$H NMR both before and after the copolymerization.

The characteristic peaks of monomer, initiator and chloroform-d solvent in $^1$H NMR spectra are compared in Figure 4.6. The characteristic peaks of HMP were located at 1.58, 7.41, 7.51 and 7.99 ppm. Among them, 7.41, 7.51 and 7.99 ppm are assigned to the protons in the benzene ring. Similarly, the characteristic peaks of MMA at 5.65 and 6.01 ppm and characteristic peaks of dMEMUABr at 5.74 and 6.08 ppm were integrated by referencing to DMF characteristic peak. After UV illumination, the composition of copolymer was calculated by the reduction of MMA and dMEMUABr mole number. Specifically, the mole fraction of MMA in copolymer $F_1$ is the reduction of MMA mole number versus the total monomers consumed. The mole fraction for each monomer in feed $f_1$ and copolymer $F_1$ are summarized in Table 4.2.

After the $F_1$-$f_1$ data was collected, the reactivity ratio $r_{MMA}=0.73$, $r_{dMEMUABr}=4.42$ were calculated by the linear regression using the KT method. The linear regression plot is shown in Figure 6.3, and the calculation parameters for KT plot are provided in Table 6.1in the Appendices. Reactivity ratios determined by the NLLS method was $r_{MMA}=0.76$, $r_{dMEMUABr}=4.48$. The values achieved by the linear KT an d NLLS methods were similar.
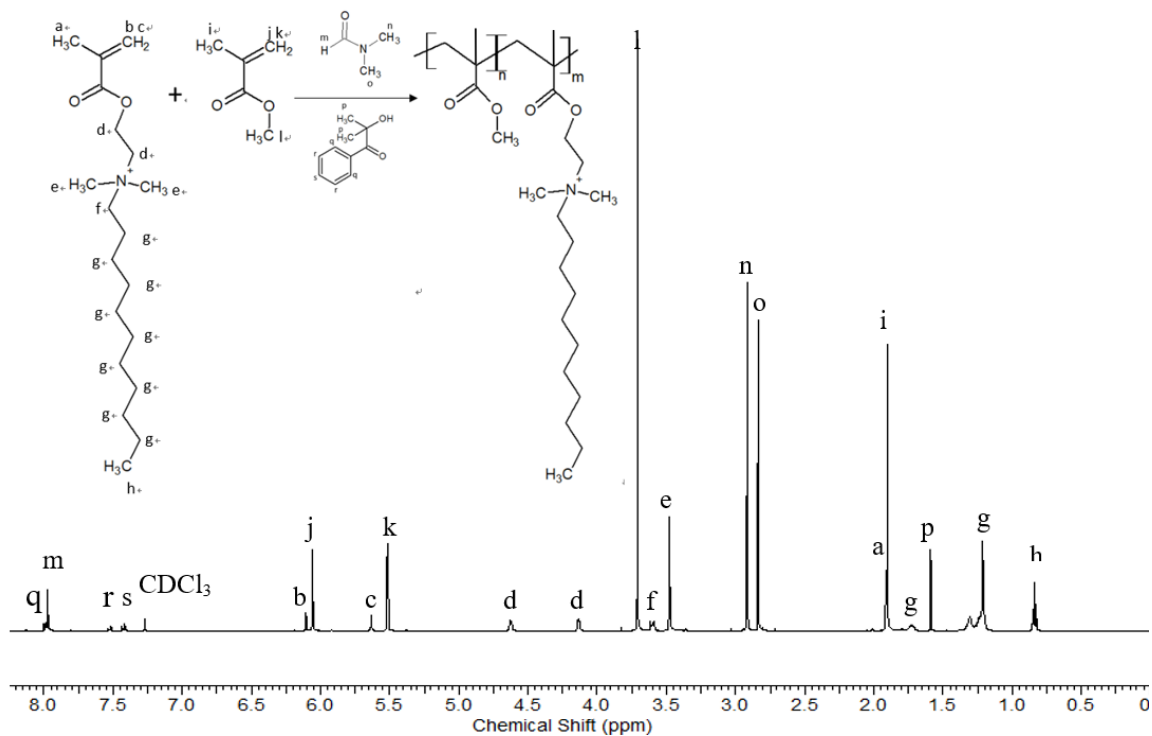
**Figure 4.6：** **$^1$H NMR spectra of UV initiated copolymerization mixture in chloroform-d solvent.**

**Table 4.2： Mole fraction of MMA and dMEMUABr in feed and copolymer in UV initiated copolymerization using chloroform-d solvent, analyzed by $^1$H NMR spectra.**

| Mole fraction of MMA in feed ($f_1$) | Mole fraction of MMA in copolymer ($F_1$) |
|---|---|
| 0.46 | 0.20 |
| 0.51 | 0.25 |
| 0.58 | 0.33 |
| 0.77 | 0.63 |
| 0.83 | 0.69 |

### 4.4.4  Comparison of reactivity ratios of MMA and dMEMUABr in thermal and UV initiated copolymerization

The reactivity ratios achieved for both the thermal initiated and UV initiated free radical copolymerization are summarized in Table 4.3. The reactivity ratio for MMA is lower than that of dMEMUABr for the UV initiated copolymerization, which was consistent with those calculated using the thermal initiated copolymerization when non-polar chloroform-d solvent was employed. dMEMUABr is even more reactive when inserted to the propagating end in thermal initiated than in UV initiated copolymerization. When the solvent changed to polar solvent DMSO-$d_6$, the reactivity ratio of MMA became higher than that of dMEMUABr.  A higher dMEMUABr mole fraction in the feed is required if more dMEMUABr needs to be incorporated into the copolymer chain. Our comparison reveals that both thermal and UV initiation methods do not have significant influence on the sequence structure of the formed copolymer. However, different solvents with various polarities can affect the reactivity ratios of MMA/dMEMUABr copolymerization system. Therefore, the choice of solvent needs to be taken into account when designing and tailoring copolymers.

**Table 4.3: Summary of reactivity ratios of MMA/dMEMUABr system estimated by NLLS and KT methods in DMSO-d$_6$ and chloroform-d solvent under thermal and UV initiated copolymerization.**

|  | Solvent | Method | Data source | $r_{MMA}$ | $r_{dMEMUABr}$ |
|---|---|---|---|---|---|
| Thermal | DMSO-d | NLLS | NSD | 1.69±0.14 | 0.32±0.05 |
|  |  |  | DND | 1.73±0.26 | 0.29±0.09 |
|  |  | K-T | NSD | 1.70 | 0.32 |
|  |  |  | DND | 1.65 | 0.24 |
|  | CDCl$_3$-d | NLLS | NSD | 0.46±0.16 | 11.51±3.11 |
|  |  |  | DND | 0.27±0.14 | 10.08±3.53 |
|  |  | K-T | NSD | 0.28 | 8.55 |
|  |  |  | DND | 0.06 | 6.64 |
| UV initiated | CDCl$_3$-d | NLLS | / | 0.76 | 4.48 |
|  |  | K-T | / | 0.73 | 4.42 |

## 4.5 Conclusions

Free radical copolymerization of MMA and synthesized QAC dMEMUABr was carried out by thermal initiator AIBN and UV initiator HMP respectively. The comparison of reactivity ratios of this system between thermal copolymerization and UV copolymerization was investigated for the first time. For the thermal copolymerization at 60 °C, *in-situ* ^{1}H NMR technique was used for monitoring the change of each monomer during the entire copolymerization time. Reactivity ratios were calculated by both the

NLLS and linear KT methods, which gave similar results. When using the non-polar solvent chloroform-d, the reactivity ratio of MMA ($r_{MMA}$=0.06-0.46) is lower than that of dMEMUABr ($r_{dMEMUABr}$=6.64-11.51), which was found consistent for the reactivity ratios in UV initiated copolymerization ($r_{MMA}$=0.73-0.76, $r_{dMEMUABr}$=4.42-4.48), indicating higher tendency of dMEMUABr units added into the copolymer. However, in the polar solvent DMSO-$d_6$, the reactivity ratio of MMA ($r_{MMA}$=1.65-1.73) is higher than that of dMEMUABr ($r_{dMEMUABr}$=0.24-0.32). The measured reactivity ratios using different solvents and different initiation methods offers valuable information for designing copolymer with specified function.

## 4.6 References

[1] Yao Z, Cui Y, Zheng K, et al. Composition and properties of porous blend membranes containing tertiary amine based amphiphilic copolymers with different sequence structures [J]. J Colloid Interface Sci, 2015, 437:124-131.

[2] Zaremba D, Menzel H, Kowalsky W, et al. Styrene based copolymers for consistent reactivity ratio evaluation [J]. Materials Chemistry and Physics, 2018, 209:227-232.

[3] C.Erbil, S.Özdemir, N.Uyanık. Determination of the monomer reactivity ratios for copolymerization of itaconic acid and acrylamide by conductometric titration method [J]. Polymer, 2000, 41:1391-1394.

[4] Roka N, Kokkorogianni O, Pitsikalis M. Statistical copolymers of N-vinylpyrrolidone and 2-(dimethylamino)ethyl methacrylate via RAFT: Monomer reactivity ratios, thermal properties, and kinetics of thermal decomposition [J]. Journal of Polymer Science Part A: Polymer Chemistry, 2017, 55 (22):3776-3787.

[5] O'Driscoll KF, Reilly PM. Determination of reactivity ratios in copolymerization [J]. 1987, 10-11 (1):355-374.

[6] F. GCLK, O'Driscoll, Reilly PM. Estimating reactivity in free radical copolymerizations [J]. Journal of Polymer Science, 1985, 72 (1).

[7] Habibi A, Vasheghani-Farahani E, Semsarzadeh MA, et al. Monomer reactivity ratios for lauryl methacrylate-isobutyl methacrylate in bulk free radical copolymerization [J]. Polymer International, 2003, 52 (9):1434-1443.

[8] Hofmeyr JH, Gqwaka OP, Rohwer JM. A generic rate equation for catalysed, template-directed polymerisation [J]. FEBS Lett, 2013, 587 (17):2868-2875.

[9] Zhang M, Carnahan EM, Karjala TW, et al. Theoretical Analysis of the Copolymer Composition Equation in Chain Shuttling Copolymerization [J]. Macromolecules, 2009, 42 (21):8013-8016.

[10] Zhang Z, Zheng H, Huang F, et al. Template Polymerization of a Novel Cationic Polyacrylamide: Sequence Distribution, Characterization, and Flocculation Performance [J]. Industrial & Engineering Chemistry Research, 2016, 55 (37):9819-9828.

[11] Jampala SN, Sarmadi M, Somers EB, et al. Plasma-enhanced synthesis of bactericidal quaternary ammonium thin layers on stainless steel and cellulose surfaces [J]. Langmuir, 2008, 24 (16):8583-8591.

[12] Roy D, Knapp JS, Guthrie JT, et al. Antibacterial cellulose fiber via RAFT surface graft polymerization [J]. Biomacromolecules, 2008, 9 (1):91-99.

[13] Zhao J, Millians W, Tang S, et al. Self-Stratified Antimicrobial Acrylic Coatings via One-Step UV Curing [J]. ACS Appl Mater Interfaces, 2015, 7 (33):18467-18472.

[14] Ergün Y, Dirier C, Tanoğlu M. Polymethyl methacrylate based open-cell porous plastics for high-pressure ceramic casting [J]. Materials Science and Engineering: A, 2004, 385 (1-2):279-285.

[15] Jagan Mohan D. Synthesis, characterization and swelling properties of copolymers of N(-1,1-dimethyll-3-oxobutyl)acrylamide with methyl methacrylate [J]. Designed Monomers and Polymers, 2013, 17 (5):438-444.

[16] Faraguna F, Vidović E, Jukić A. Reactivity ratios and copolymer properties of 2-(diisopropylamino)ethyl methacrylate with methyl methacrylate and styrene [J]. Polymer International, 2015, 64 (10):1497-1504.

[17] Feng J, Oyeneye OO, Xu WZ, et al. In-Situ NMR Measurement of Reactivity Ratios for Copolymerization of Methyl Methacrylate and Diallyl Dimethylammonium Chloride [J]. Industrial & Engineering Chemistry Research, 2018, 57 (46):15654-15662.

[18] Patton DL, Page KA, Hoff EA, et al. A robust and high-throughput measurement platform for monomer reactivity ratios from surface-initiated polymerization [J]. Polymer Chemistry, 2012, 3 (5):1174.

[19] Wang Y, Zhang X, Li W, et al. Determination of Reactivity Ratios of Copolymerization of Acrylamide (AM) and Methacryloxyethyltrimethyl Ammonium Chloride (DMC) with Ultraviolet Initiation, and Their Sequence Length Distribution [J]. Polymers & Polymer Composites, 2016, 24.

[20] Preusser C, Hutchinson RA. An In-Situ NMR Study of Radical Copolymerization Kinetics of Acrylamide and Non-Ionized Acrylic Acid in Aqueous Solution [J]. Macromolecular Symposia, 2013, 333 (1):122-137.

[21] Zhang W, Allgaier J, Zorn R, et al. Determination of the Compositional Profile for Tapered Copolymers of Ethylene Oxide and 1,2-Butylene Oxide by In-situ-NMR [J]. Macromolecules, 2013, 46 (10):3931-3938.

[22] CANKAYA N, TEMÜZ MM. Monomer reactivity ratio of cellulose grafted with N-cyclohexylacrylamide and methyl methacrylate by atom transfer radical polymerization [J]. Cellulose Chemistry and Technology, 2012, 48:209-215.

[23] El-Newehy MH, Al-Deyab SS, Al-Hazmi AM. Reactivity ratios for organotin copolymer systems [J]. Molecules, 2010, 15 (4):2749-2758.

[24] Cuccato D, Storti G, Morbidelli M. Experimental and Modeling Study of Acrylamide Copolymerization with Quaternary Ammonium Salt in Aqueous Solution [J]. Macromolecules, 2015, 48 (15):5076-5087.

[25] Wu Z, Liu P, Liu Y, et al. Regulating sequence distribution of polyethers via ab initio kinetics control in anionic copolymerization [J]. Polymer Chemistry, 2017, 8 (37):5673-5678.

[26] 2010. NMR Solvent Data Chart [M]. Cambridge Isotope Laboratories, Inc.

[27] Hao J, An F, Lu C, et al. Solvent effects on radical copolymerization of acrylonitrile and methyl acrylate: solvent polarity and solvent-monomer interaction [J]. Journal of Macromolecular Science, Part A, 2019, 56 (11):1012-1021.

[28] Idowu LA, Hutchinson RA. Solvent Effects on Radical Copolymerization Kinetics of 2-Hydroxyethyl Methacrylate and Butyl Methacrylate [J]. Polymers (Basel), 2019, 11 (3).

# Chapter 5

# 5 Summary and Future Work

## 5.1 Summary

In this thesis, the synthesis method of antimicrobial/thermochromic dual-functional coating using dMEMUABr and $VO_2$ nanoparticles was reported and the performance of the coating was well characterized. The reactivity ratios of MMA and dMEMUABr monomer were determined under thermal and UV initiated copolymerization using *in-situ* NMR and conventional low-conversion technique. Main conclusions are listed as follows:

1. dMEMUABr and MMA completely copolymerized within 4 min UV curing. It was found that photo initiator HMP decomposed itself to acetone and benzaldehyde during the UV exposure, and vacuum heating at 70 °C can remove some of them. The remaining was difficult to be removed, due to high boiling point or being trapped within polymer.

2. The dual-functional coating showed 5.8 % solar energy modulation, and high luminous transmittance (41.1 % and 36.1 % at 90 °C and 25 °C). The antimicrobial test of the dual-functional coating indicated 90.3 % of E.coli bacteria reduction with 24 h contact. The antimicrobial efficiency decreased by 9.5 % compared to pure poly dMEMUABr coating, may due to the occupation of the active area by $VO_2$ particles. The dual-functional coating was proved based on contact kill, without releasing toxic moieties to the surroundings.

3. When using the same chloroform-d solvent, the reactivity ratio of MMA ($r_{MMA}$=0.06-0.46) was found to be lower than that of dMEMUABr ($r_{dMEMUABr}$=6.64-11.51) in thermal initiated copolymerization, which was consistent for the reactivity ratios in UV initiated copolymerization ($r_{MMA}$=0.73-0.76, $r_{dMEMUABr}$=4.42-4.48). That indicated dMEMUABr units are more active to be added into the copolymer. The different initiation method do not have significant influence on reactivity ratios.

4. When using the polar solvent DMSO-d$_6$, the reactivity ratio of MMA ($r_{MMA}$=1.65-1.73) is higher than that of dMEMUABr ($r_{dMEMUABr}$=0.24-0.32), which showed the opposite trend, compared to reactivity ratios obtained using non-polar chloroform-d solvent. That indicated the significant impact of solvent polarities on reactivity ratios.

## 5.2 Future Work

To further improve the system, some suggestions on the future work are listed as follows:

1. The transition temperature of VO$_2$ particle is too high to be realistically used for window coating. Doping with metal ion to decrease the transition temperature near room temperature can be followed up to make the coating more applicable. Tungsten is considered as the most efficient elements, which can make transition temperature drop by 20 K per at. %.

2. Further tests of the dual-functional coating should be considered. Physical and mechanical testing of the coating need to be carried out, such as ductility test and adhesion test. These tests can help to better understand the durability of the coating and its optimization. Antimicrobial test of the coating against other types of organisms, such as fungus, parasites, can be carried out to further explore the property of QACs.

3. The reactivity ratios of MMA and dMEMUABr using DMSO-d$_6$ under UV initiated copolymerization need to be carried out in the future, so that the impact the solvent polarities on reactivity ratios in this system can be reconfirmed.

# 6    Appendices

MATLAB code for collecting Y axis data from the fit curve. *interp1* returns interpolated values of 1-D function at specific query points with linear interpolation.

```
>> Yout=interp1(X,Y,Xin,'spline')
```

MATLAB code for solving reactivity ratio with NLLS method, finding most fit $r_1$ and $r_2$ with Mayo-Lewis equation. *nlinfit* estimates the coefficients for the nonlinear regression using the model of *modelfun*. The returned values are estimated using iterative least squares estimation, with given initial value of [1;1].

```
>> modelfun = @(k,f1) (k(1).*f1.^2+f1.*(1-f1))./(k(1).*f1.^2+2.*f1.*(1-f1)+k(2).*(1-f1).^2);
```

```
>> ratio=nlinfit(f1,F1,modelfun,[1;1])
```

**Figure 6.1：Picture of NMR tube after 10 h thermal copolymerization reaction at 50 °C. No sediment was observed.**
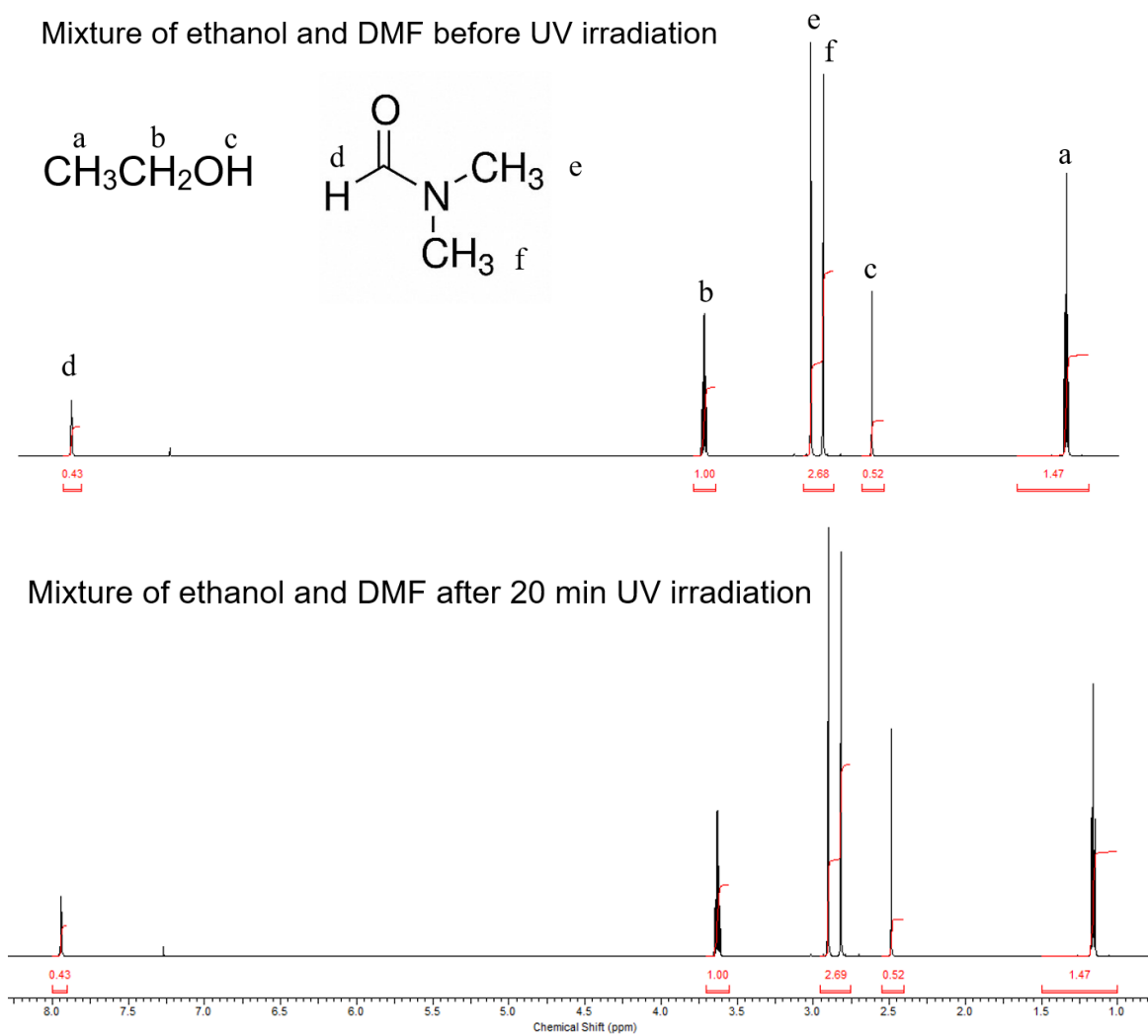
**Figure 6.2:** **$^1$H NMR spectra of mixture of ethanol and DMF before and after 20 min UV exposure.**

**Kelen-Tüdös** method for reactivity ratios calculation:

$$\alpha = (H_{min}H_{max})^{0.5}; \quad \eta = \left(r_1 + \frac{r_2}{\alpha}\right)\mu - \frac{r_2}{\alpha}$$

**Table 6.1: Calculation parameters for KT method under UV initiated copolymerization**

| $f_1$ (MMA) | $F_1$ (MMA) | $G = \dfrac{f_1(2F_1 - 1)}{(1 - f_1)F_1}$ | $H = \dfrac{f_1^{\,2}(1 - F_1)}{(1 - f_1)^2 F_1}$ | $\mu = \dfrac{H}{\alpha + H}$ | $\eta = \dfrac{G}{\alpha + H}$ |
|---|---|---|---|---|---|
| 0.46 | 0.2 | -2.55556 | 2.902606 | 0.342367 | -0.30143 |
| 0.51 | 0.25 | -2.08163 | 3.249896 | 0.368246 | -0.23587 |
| 0.58 | 0.33 | -1.4228 | 3.871848 | 0.409837 | -0.1506 |
| 0.77 | 0.625 | 1.33913 | 6.724764 | 0.54672 | 0.108871 |
| 0.83 | 0.69 | 2.688832 | 10.70954 | 0.657633 | 0.165111 |
| 0.46 | 0.2 | -2.55556 | 2.902606 | 0.342367 | -0.30143 |
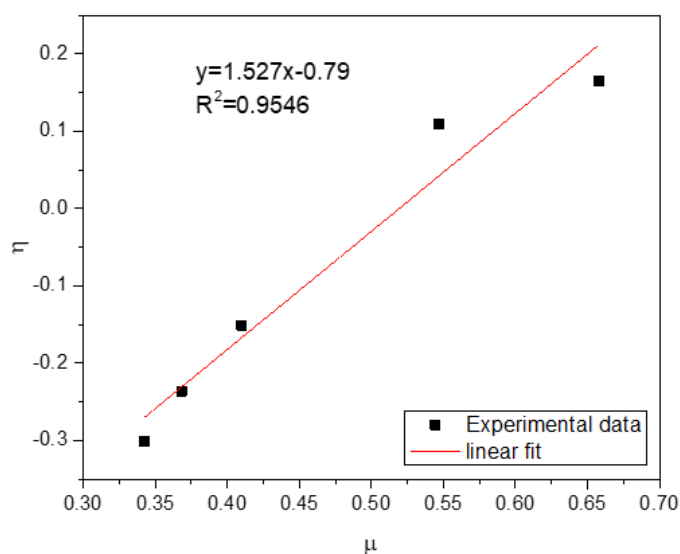


**Figure 6.3: KT plots for MMA/dMEMUABr system under UV initiated copolymerization in chloroform-d solvent.**

# Curriculum Vitae

**Name:**           Yixian Liu

**Post-secondary**    East China University of Science and Technology
**Education and**      Shanghai, China
**Degrees:**          2013-2015 B.E.

                     University of Western Ontario
                     London, Ontario, Canada
                     2015-2017 B.E.

                     University of Western Ontario
                     London, Ontario, Canada
                     2017-2019 M.E.Sc.

**Related Work**     Teaching Assistant
**Experience**       University of Western Ontario
                     2018-2019